STRATEGIES FOR SELECTIVE TARGETING OF THE WARBURG EFFECT IN CANCER

A Dissertation

Presented to the Faculty of the Graduate School

of Cornell University

In Partial Fulfillment of the Requirements for the Degree of

Doctor of Philosophy

by

Maria Volpe Liberti

December 2018

STRATEGIES FOR SELECTIVE TARGETING OF THE WARBURG EFFECT IN CANCER

Maria Volpe Liberti, Ph.D.

Cornell University 2018

Cancer cells undergo numerous adaptive processes to sustain rapid growth and survival. One notable mechanism is by rewiring their metabolism, most prominently through a phenomenon known as the Warburg Effect (WE). The WE is defined as an increase in glucose consumption and lactate secretion in the presence or absence of oxygen. Although the WE has been extensively studied, efforts to therapeutically target it have been largely unsuccessful due to the lack of obvious metabolic biomarkers and difficulties achieving full enzyme inhibition without inducing toxicity in normal tissue. Although targeted cancer therapies that use genetics have been successful, principles for selectively targeting tumor metabolism that also depend on environmental factors remain unknown. This limitation prompted the investigation to determine whether differential control in metabolism can be exploited for therapy.

In this dissertation, I first determined whether therapeutic targeting of glyceraldehyde-3-phosphate dehydrogenase (GAPDH), an enzyme that differentially regulates the Warburg Effect in cancer, can result in anti-tumor efficacy. Using comparative metabolomics, integrated pharmacogenomics, and systems biology, I found that koningic acid (KA), a natural product produced by the *Trichoderma* species, is a highly specific inhibitor of GAPDH. Notably, I determined that the quantitative extent of

the Warburg Effect predicts response to KA in both cancer cells and tumors. Secondly, given the efficacy of KA in cancers specifically undergoing the Warburg Effect, I next used KA as a tool to determine whether there is a biological distinction between the Warburg Effect and glycolysis. I developed an evolved resistance model to KA and confirmed using metabolomics, stable isotope tracing, and a set of pharmacological approaches that glucose metabolism can exist in multiple states in the cell with distinct metabolic outputs. Lastly, I used therapeutic and genetic interventions to target 3-phosphoglycerate dehydrogenase (PHGDH), which diverts glucose flux into serine biosynthesis, and showed that this disrupts cancer cell growth through inhibition of *de novo* serine synthesis and downstream serine metabolism. Together, my findings contribute to a shifting paradigm in the current understanding of metabolic cancer therapy and show the potential use of metabolic factors as predictors and important determinants of therapeutic response.

BIOGRAPHICAL SKETCH

Maria Volpe Liberti was born on October 24, 1990 in Secaucus, New Jersey. She is the daughter of Augusto and Janet Liberti and is the oldest of three children – Giuseppe and Gabriella Liberti. During Maria's junior year of high school at the Montclair Kimberley Academy, she took a Biology II Honors course where she began to learn about the intricacies of signaling pathways in cancer. This course captivated her curiosity for a deeper understanding of the molecular intricacies within a cell where she came to realize the numerous questions still unanswered. She was eager to explore the cancer field further and began volunteering at the Oncology Unit at Mountainside Hospital in Montclair, NJ. There, she learned about the limitations in current cancer therapies and wanted to become part of the research effort to advance the cancer field. During her senior year in high school, she carried out a year-long independent research project where she learned how to use the scientific method and experienced the personal fulfillment that comes with engaging in scientific research.

When Maria entered Lafayette College in Easton, PA, she was determined to pursue her passion for cancer research. In 2011, she began doing research there in the Department of Biology under the mentorship of Dr. Robert Kurt. In Dr. Kurt's laboratory, she explored how myeloid differentiation primary response gene 88 (MYD88) inhibitors affect 4T1 murine mammary carcinoma cell growth. In the summer of 2012, Maria was selected as a summer undergraduate research fellow at Boston University under the mentorship of Dr. Thomas Gilmore where she studied the evolutionary conservation of toll-like receptor 4 (TLR) in the *Nematostella vectensis* sea anemone. During this 10-week experience, Maria was introduced to bioinformatics and molecular cloning techniques. Upon Maria's return to Lafayette in fall 2012, she undertook a senior honors thesis where she conceptualized a project to investigate the effects of auranofin, a gold-based compound, on cancer cells to determine the mechanisms of cell death and its effects on the cell cycle. Together, her college efforts culminated in the receipt of her Bachelor

of Science in biology with honors in spring 2013.

In fall 2013, Maria attended Cornell University in the field of Biochemistry, Molecular, and Cell Biology to pursue her Ph.D. and continue her passion for cancer research. She joined the laboratory of Dr. Jason Locasale in 2014 to investigate cancer metabolism with a focus on the Warburg Effect. After just over a year of joining the Locasale lab, the lab relocated to the Department of Pharmacology and Cancer Biology at Duke University in the fall 2015 where she has continued her dissertation work as a visiting student. During her graduate school career, Maria received the Cornell/Sloan Fellowship, the National Science Foundation Graduate Research Fellowship, and the National Cancer Institute F99/K00 Predoctoral to Postdoctoral Transition award. Upon graduation, Maria is excited to begin her postdoctoral work at the Rockefeller University.

Dedicated to my loving and supportive family.

ACKNOWLEDGMENTS

I would first and foremost like to thank my PhD advisor and phenomenal mentor, Dr. Jason Locasale. He is an exceptional scientist and I truly owe all my scientific and writing skills to him. From Jason, I have learned the talent, dedication, and determination necessary to successfully run a lab. He has always pushed me beyond my limits and never let me settle for less than my potential. The wealth of support that he has provided me over the years on both my projects and in my career has been invaluable. I am incredibly grateful that I relocated to Duke University with the lab and believe that this was the best decision I could have made scientifically. I am thankful for all his guidance and commitment to my success during my PhD.

I would also like to thank my committee members, Dr. Richard Cerione and Dr. Robert Weiss. Even from afar, they both have provided me with valuable advice on my projects and my career. I have always felt supported from them both and knew that they were only a phone call or email away. I also thank Cornell's Molecular Biology and Genetics department for their support during my PhD while I was at Cornell and during my transition to Duke.

I also express my sincere gratitude to Dr. Xiaojing Liu for teaching me metabolomics and mass spectrometry. I would also like to thank all the members of the Locasale lab, especially Dr. Samantha Mentch, Dr. Ahmad Cluntun, and Dr. Mahya Mehrmohamadi for their scientific and personal support both while I was at Cornell and even after when I moved to Duke.

While at Duke, I have been so fortunate to have invaluable support from other lab members in the Locasale lab, especially Sydney Sanderson and Dr. Michael Reid. They

both have been there for me to celebrate my successes, but to also talk me through any challenges I faced during graduate school. I would also like to thank Dr. Madan Kwatra for giving me the opportunity to be a teaching assistant for his course "Pharmacogenomics and Personalized Medicine" while at Duke and the Duke Pharmacology and Cancer Biology department for making me feel like one of their own.

Much of this work could not have been done without the help of my fantastic collaborators. I am especially thankful to Dr. Qian Wang from Dr. Luhua Lai's lab for our collaboration on the PHGDH project. I am also sincerely thankful to my many other collaborators who provided essential materials and assistance on my projects, especially Dr. Joshua Baccile from Dr. Frank Schroeder's lab, Dr. Suzanne Wardell from Dr. Donald McDonnell's lab, and all others. The success of my projects would not have been possible without all their help.

My graduate school experiences would not have been the same without the loving and unconditional encouragement from my friends both at Cornell and at Duke. While I already thanked Sydney Sanderson for her support in the laboratory, I cannot express my gratitude enough for the constant support I received from her as an amazing friend. She has encouraged me since the moment I arrived at Duke and always reminds me to keep seeing the bigger picture. I am also thankful to Andrea Walens who has always been there for me and has also been an amazing friend, as well as Victoria Deneke who has been a great roommate and a wonderful friend. These girls have really helped make my graduate school experience at Duke a truly memorable one.

I would especially like to thank Marcel Naguiat for being there for me since the beginning of my graduate school journey. I am thankful for his patience and

understanding of the commitment involved in doing science and earning a PhD. Marcel has been my constant support system, even with the many miles between us for more than half my time in graduate school. I thank him for always being there for me and pushing me to my fullest potential.

I would also like to especially and most importantly thank the pillars of my success, my loving parents Augusto and Janet, and my siblings Giuseppe and Gabriella Liberti. I thank Giuseppe and Gabby for always supporting me, both near and far. I am so lucky to have them as siblings and I love them for always wanting the best for me. My parents have always instilled in me the importance of finding my passion and pursuing a career that brings me joy and fulfillment. It is with their unwavering love and encouragement that I have been given the capability of accomplishing my goals of becoming a scientist, and I thank them so much for that. The demands of earning a PhD have kept me away from them and from family events that I wish I could have been there for, but I thank them for their understanding of my absence and I cannot wait to be close to them again. They are the greatest strength that God has given me.

Lastly, I thank my funding sources. I was supported by the Cornell/Sloan Fellowship (70481/A001), the National Science Foundation Graduate Research Fellowship (DGE-1144153), and the National Cancer Institute Predoctoral to Postdoctoral Transition Fellowship (F99CA222986). My work was also supported by grants from the National Institute of Health (R01CA193256 and R00CA168997) and the International Life Sciences Institute given to my advisor, Dr. Jason Locasale.

TABLE OF CONTENTS

LIST OF FIGURES

LIST OF ABBREVIATIONS

1,3-BPG: 1,3-Bisphosphoglycerate

3BP: 3-Bromopyruvate

3PG: 3-Phosphoglycerate

αKG: Alpha-Ketoglutarate

ADP: Adenosine Diphosphate

ALDO: Aldolase

ALT: Alanine Transferase

AMP: Adenosine Monophosphate

As_2O_3: Arsenic Trioxide

As_2O_4: Arsenate

ATP: Adenosine Triphosphate

CMP: Cytidine Monophosphate

CTP: Cytidine Triphosphate

DCA: Dichloroacetate

DHAP: Dihydroxyacetone Phosphate

E4P: Erythrose-4-Phosphate

ENO: Enolase

F1,6-BP: Fructose 1,6-Bisphosphate

FAD^+: Flavin Adenine Dinucleotide

FBP: Fructose 1,6-Bisphosphatase

FCC: Flux Control Coefficient

G3P: Glycerol-3-Phosphate

G6P: Glycerate-6-Phosphate

GA3P: Glyceraldehyde-3-Phosphate

GAPDH: Glyceraldehyde-3-Phosphate Dehydrogenase

GDP: Guanosine Diphosphate

GLUT: Glucose Transporter

GMP: Guanosine Monophosphate

GPI: Glucose Phosphate Isomerase

GSH: Reduced Glutathione

GSSG: Oxidized Glutathione

GTP: Guanosine Triphosphate

HK: Hexokinase

IA: Iodoacetate

KA: Koningic Acid

LDH: Lactate Dehydrogenase

MCA: Metabolic Control Analysis

MID: Mass Isotopomer Distribution

NAD^+: Nicotinamide Adenine Dinucleotide

NADH: Reduced Nicotinamide Adenine Dinucleotide

NADPH: Reduced Nicotinamide Adenine Dinucleotide Phosphate

NSCLC: Non-Small Cell Lung Cancer

OIS: Oncogene-Induced Senescence

PAM: Protospacer Adjacent Motif

PEP: Phosphoenolpyruvate

PFK: Phosphofructokinase

PGAM: Phosphoglycerate Mutase

PGK: Phosphoglycerate Kinase

PHGDH: 3-Phosphoglycerate Dehydrogenase

PK: Pyruvate Kinase

PPP: Pentose Phosphate Pathway

R5P: Ribose-5-Phosphate

ROC: Receiver-Operating Characteristic

ROS: Reactive Oxygen Species

S7P: Sedoheptulose-7-Phosphate

sgRNA: Single-Guide RNA

TAM: Tumor Associated Macrophage

TCA: The Citric Acid Cycle

TIL: Tumor-Infiltrating Lymphocyte

TPI: Triose-Phosphate Isomerase

UMP: Uridine Monophosphate

UDP: Uridine Diphosphate

UTP: Uridine Triphosphate

WE: Warburg Effect

X5P: Xylulose-5-Phosphate

LIST OF SYMBOLS

ºC: degrees Celsius

Å: Angstrom

g: times gravity

hr: hour

kg: kilogram

kV: kilovolt

min: minute

mg: milligram

µL: microliter

µm: micrometer

µM: micromolar

mL: milliliter

mm: millimeter

ms: millisecond

m/z: mass over charge ratio

nm: nanometer

ppm: parts per million

v/v: volume/volume percent

CHAPTER 1: INTRODUCTION[1]

1.1 Introduction to the Warburg Effect

It is well-established that cancer cells rewire their metabolism to sustain rapid proliferation, energy, and cellular homeostasis demands. Cancer cells meet their growth and energy requirements by upregulating anabolic metabolic pathways for the production of biomass, as well as upregulating catabolic pathways for the production of energy and reducing equivalents (Boroughs and DeBerardinis, 2015; DeBerardinis and Chandel, 2016; Locasale and Cantley, 2011; Pavlova and Thompson, 2016; Vander Heiden and DeBerardinis, 2017). Many of these alterations occur as a result of oncogene activation and/or loss of tumor suppressor genes that regulate key enzymes in metabolic pathways (Dang, 2012; DeNicola et al., 2011; Levine and Puzio-Kuter, 2010). Together, metabolic reprogramming confers a number of signaling outputs in the cell and interactions between oncogenic signaling pathways, chromatin regulation, and the environment. One of the most well-known and established mechanisms by which cancer cells rewire their metabolism is through a phenomenon known as the Warburg Effect (i.e. aerobic glycolysis). The Warburg Effect is defined as an increase in glucose uptake and lactate secretion in the presence of absence of oxygen (Vander Heiden et al., 2009; Warburg, 1956; Warburg et al., 1927).

Although the Warburg Effect is the oldest and most well-studied metabolic reprogramming process in cancer metabolism, there are still many unanswered questions

[1] This chapter was adapted and modified from published work: Liberti, M.V. and Locasale, J.W., 2016. The Warburg effect: how does it benefit cancer cells? *Trends in biochemical sciences*, *41*(3), pp.211-218.

in the field. While therapeutic targeting of glycolytic enzymes in cancer has been an intense area of research, there are still challenges associated with effective enzyme inhibition. Moreover, despite the clear importance of the Warburg Effect in the clinic, such as its diagnostic relevance in FDG-PET imaging to measure glucose uptake in tumors, there is much debate as to whether the Warburg Effect has clearly defined functions and biological outputs in cancer. Thus, while many research efforts have been made in the past century to understand, define, and target the Warburg Effect, its functions remain unclear. In this chapter, I discuss several proposed explanations for the function of the Warburg Effect, emphasize their rationale, and discuss their controversies. In addition, I review the current progress made in the field on therapeutic targeting efforts of the Warburg Effect.

1.2 Glucose metabolism and the Warburg Effect

The metabolism of glucose, the central macronutrient, allows for energy to be harnessed in the form of ATP through the oxidation of its carbon bonds. This process is essential for sustaining all mammalian life. In mammals, the end product can be lactate or, upon full oxidation of glucose via respiration in the mitochondria, CO_2. In tumors and other proliferating or developing cells, the rate of glucose uptake dramatically increases and lactate is produced, even in the presence of oxygen and fully functioning mitochondria. This process, known as the Warburg Effect, has been studied extensively (Figure 1.1). However, after careful inspection, it becomes apparent that its benefits for cell growth and survival are not yet resolved. This analysis will focus on several proposals

for its function, and in each case, we discuss their appeal as well as their drawbacks. Before our discussion of each proposal, we first introduce the Warburg Effect in a historical context with an emphasis on lesser-appreciated aspects of its conceptual development. It is our hope that this retrospective brings additional context to current ideas in cancer metabolism.

1.3 Historical perspectives of the Warburg Effect

In the 1920s, Otto Warburg and colleagues made the observation that tumors were taking up enormous amounts of glucose compared to what was seen in the surrounding tissue. Additionally, glucose was fermented to produce lactate even in the presence of oxygen, thus the term aerobic glycolysis (Warburg, 1925; Warburg et al., 1924). However, it was also noted that respiration alone could maintain tumor viability. Therefore, it was concluded that in order to kill tumor cells by depriving them of energy, both glucose and oxygen had to be eliminated (Warburg et al., 1927). Subsequently, in 1929, an English biochemist, Herbert Crabtree, extended Warburg's work and studied the heterogeneity of glycolysis in tumor types. He confirmed Warburg's findings, but further discovered that the magnitude of respiration in tumors was variable with many tumors exhibiting a substantial amount of respiration (Crabtree, 1929). Therefore, Crabtree concluded that not only do tumor cells exhibit aerobic glycolysis, but that there is also variability in fermentation presumably due to environmental or genetic influences.

Contrary to the findings of these previous works and for reasons unclear to these authors, Warburg later proposed that dysfunctional mitochondria is the root of aerobic

glycolysis (Warburg, 1956). Warburg further hypothesized that this event is the primary cause of cancer. This phenomenon was then termed the Warburg Effect in the early 1970s by Efraim Racker, who also pointed out that previous data showed respiratory capability of tumors. Racker developed his own theories about the origins of the Warburg Effect ranging from imbalances in intracellular pH to defects in ATPase activity (Racker, 1972). It was later observed by Racker, Jeffrey Flier and Morris Birnbaum that aerobic glycolysis was a controllable process that can be directly regulated by growth factor signaling. By that time, the discovery of oncogenes led to the conclusion that aberrant regulation of growth factor signaling is an initiating event in oncogenesis. Thus, their observations brought newfound significance to Warburg's hypothesis in cancer biology (Birnbaum et al., 1987; Boerner et al., 1985; Flier et al., 1987; Hiraki et al., 1988). Nevertheless, it remained unclear whether the Warburg Effect was a bystander in cancer pathogenesis until more recently, when genetic and pharmacological studies conclusively showed that the Warburg Effect was required for tumor growth (Fantin et al., 2006; Shim et al., 1998). Coming back to the original findings on tumor metabolism, it is now apparent that targeting both aerobic glycolysis and mitochondrial metabolism may be required (Birsoy et al., 2015; Flaveny et al., 2015; Sullivan et al., 2015; Viale et al., 2014). Throughout this history, its functions have remained controversial. Here, we discuss several of the major proposals and argue that the functions of the Warburg Effect for tumor growth even today remain unknown.

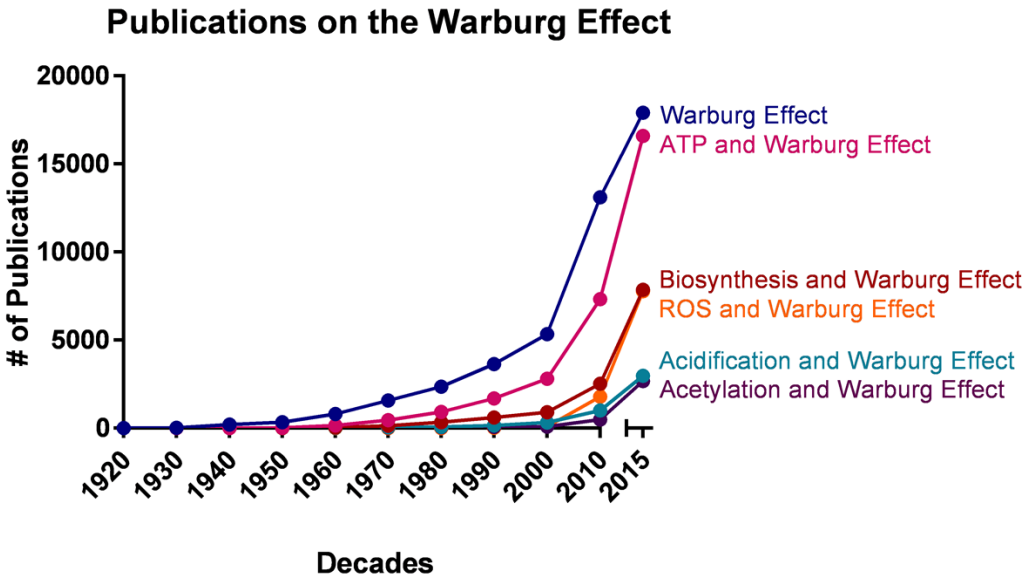

Figure 1.1. The frequency of publications on the Warburg Effect from the 1920s-2010s.
The Warburg Effect has been studied extensively since the 1920s with a surge in the number of publications from the 2000s to today. Many of the proposed functions of the Warburg Effect have also gained vastly renewed interest. Although energy (ATP), biosynthesis, and ROS have been intricately studied in the context of the Warburg Effect, acidification and acetylation have only recently gained attention.

1.4 Warburg Effect and rapid ATP synthesis

Per unit of glucose, aerobic glycolysis is an inefficient means of generating ATP compared to the amount obtained by mitochondrial respiration (Locasale et al., 2011; Vander Heiden et al., 2009). However, the rate of glucose metabolism through aerobic glycolysis is higher such that the production of lactate from glucose occurs 10-100 times faster than the complete oxidation of glucose in the mitochondria. In fact, the amount of ATP synthesized over any given period of time is comparable when either form of glucose metabolism is utilized (Shestov et al., 2014). Thus, a reasonable hypothesis on the reason that cancer employs aerobic glycolysis should account for this inherent difference in

kinetics.

Theoretical calculations using evolutionary game theory support that cells with a higher rate, but lower yield, of ATP production may gain a selective advantage when competing for shared and limited energy resources (Figure 1.2) (Pfeiffer et al., 2001; Slavov et al., 2014). In fact, tumor microenvironments have limited availability of glucose and undergo competition for nutrients with stromal cells and the immune compartment (Chang et al., 2015; Ho et al., 2015). Additional support is found in a recent study that showed when changes to the cellular environment were induced to greatly increase ATP demand by altering the demand of ATP-dependent membrane pumps, aerobic glycolysis increased rapidly and oxidative phosphorylation remained constant (Epstein et al., 2014). This finding provides additional rationale for the function of the Warburg Effect to be supporting the rapid production of ATP that can be rapidly tuned to support the demand for ATP synthesis.

Despite this attractive proposal, there are difficulties. Simple empirical calculations indicate that the amount of ATP required for cell growth and division may be much less than that required for normal cellular maintenance (Locasale et al., 2011; Lunt and Vander Heiden, 2011). Thus, ATP demand may never reach limiting values during tumor cell growth. Furthermore, the mechanisms that are available to other cell types in cases of rapid ATP demand are present in tumor cells as well. For example, rapid ATP synthesis from creatine kinases in exercised muscle or adenylate kinase under hormonal changes are present in most tumor cells and should be able to meet ATP demand. Thus, further studies are needed to show whether this mechanism can account

for the role of aerobic glycolysis.

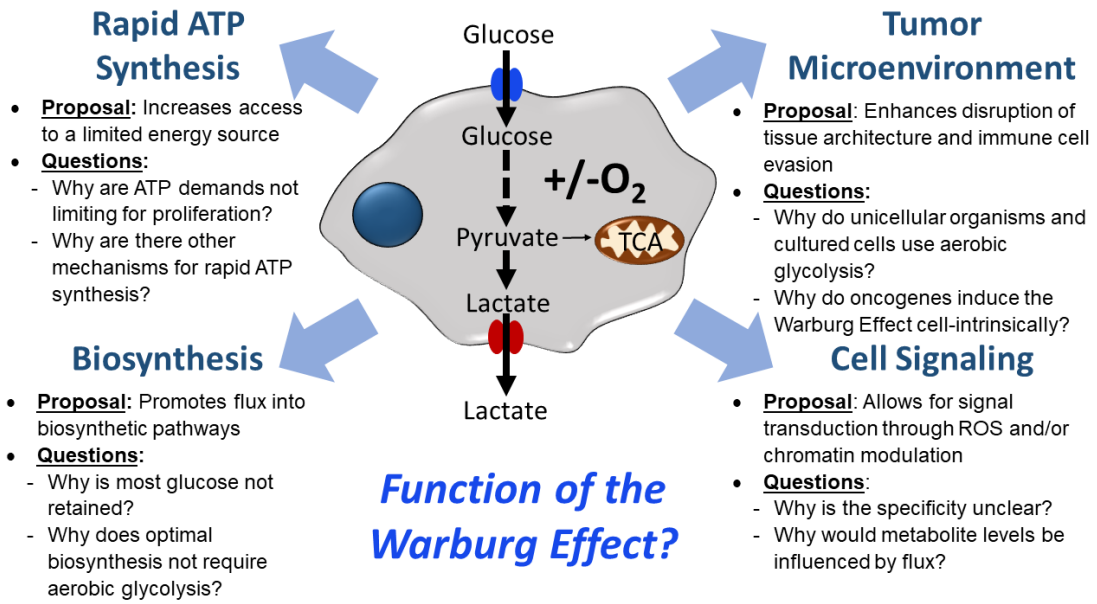

Figure 1.2 Summary of the proposed functions of the Warburg Effect.
The Warburg Effect is defined as an increase in the rate of glucose uptake and preferential production of lactate, even in the presence of oxygen. Each of these functions have been hypothesized to be the function of the Warburg Effect.

1.5 Warburg Effect and biosynthesis

The Warburg Effect has been proposed to be an adaptation mechanism to support the biosynthetic requirements of uncontrolled proliferation (Figure 1.2). In this scenario, the increased glucose consumption is used as a carbon source for anabolic processes needed to support cell proliferation (Boroughs and DeBerardinis, 2015; Cairns et al., 2011; Dang, 2012; DeBerardinis et al., 2008; Koppenol et al., 2011; Levine and Puzio-Kuter, 2010; Patra et al., 2013; Vander Heiden et al., 2009). This excess carbon is used for the de novo generation of nucleotides, lipids, and proteins and can be diverted into multiple branching pathways that emanate from glycolysis. One example is the diversion

of glycolytic flux into de novo serine biosynthesis through the enzyme phosphoglycerate dehydrogenase (PHGDH) (Locasale et al., 2011). In addition to the usage of additional carbon from enhanced glucose metabolism for cellular building blocks, a now famous argument is that rather than having a rate-limiting demand for ATP, proliferating cells are in greater need of reducing equivalents in the form of NADPH. Increased glucose uptake allows for greater synthesis of these reducing equivalents in the oxidative branch of the pentose phosphate pathway, which are then used in reductive biosynthesis, most notably in de novo lipid synthesis (Vander Heiden et al., 2009; Ward and Thompson, 2012).

Another proposed mechanism to account for the biosynthetic function of the Warburg Effect is the regeneration of NAD^+ from NADH in the pyruvate to lactate step that completes aerobic glycolysis. In this scenario, NADH that is produced by glyceraldehyde phosphate dehydrogenase (GAPDH) must be consumed to regenerate NAD^+ to keep glycolysis active. This high rate of glycolysis allows for supply lines to remain open that can, for example, siphon 3-phosphoglycerate (3PG) to serine for one-carbon metabolism-mediated production of NADPH and nucleotides (Lunt and Vander Heiden, 2011; Vander Heiden et al., 2009). These proposals together conclude that the Warburg Effect supports a metabolic environment that allows for the rapid biosynthesis to support growth and proliferation.

Furthermore, others have proposed that aerobic glycolysis is a tradeoff to support biosynthesis (Hermsen et al., 2015; Hui et al., 2015). In these scenarios, the inefficient way of making ATP occurs as a cost of maintaining high fluxes through anabolic

pathways. These pathways require increased expression of biosynthesis genes such as those involved in nucleotide and lipid metabolism and the tradeoff occurs by limiting the use of mitochondria in order to preserve high expression of biosynthetic enzymes in the face of limited protein number that can be made. Another scenario of such a tradeoff comes from the idea that the physical volume available per cell may limit mitochondria number and thus any energy and biomass that exceed the limited mitochondrial capacity needs to be produced from aerobic glycolysis (Molenaar et al., 2009; Shlomi et al., 2011; Vazquez et al., 2010). This concept has been termed the solvent capacity constraint. In both of these cases, the Warburg Effect is an adaptation to support biomass production in the face of limited options for ATP generation.

The attractiveness of this proposal in part comes from its ability to provide a simple explanation for the apparent correlation between aerobic glycolysis and cell growth and proliferation. Furthermore, it appears intuitive to some that the branching pathways from glycolysis would be used to a greater extent during the Warburg Effect since the rate of glycolysis is larger and lactate production in this case would serve to regenerate NAD^+ to allow for glycolysis to continue. Also, the requirements of NADPH for lipid generation can be summarized in a very simple chemical equation showing that the demand for NADPH is higher than that of ATP for biosynthesis (Vander Heiden et al., 2009).

However, there are major limitations for this proposed function of the Warburg Effect. First, during aerobic glycolysis, most of the carbon is not retained and is instead excreted as lactate (Lunt and Vander Heiden, 2011). In fact, the overall equation of 1

glucose molecule being converted into 2 lactate molecules with no overall gain or loss of NAD^+ and NADH leaves no room for biomass. That is, due to the stoichiometry of glycolysis, biomass production is mutually exclusive with lactate generation and it is not possible for the regeneration of NAD^+ by lactate alone to account for biosynthesis. Thus, the avenues that lead to the biosynthesis from glucose occur in the complete absence of making lactate which is the hallmark of the Warburg Effect. Also, it is now widely accepted that mitochondria are key components of the biosynthetic program whose substrates in the TCA cycle are used for nucleotide, amino acid, and lipid biosynthesis (Carracedo et al., 2013; Wellen and Thompson, 2012). In light of this evidence, it remains difficult to fathom how the Warburg Effect can directly promote biosynthesis.

Regarding proposals that define the Warburg Effect as a tradeoff to promote biosynthesis, recent estimates from quantitative proteomics show that the cost of protein production for conducting aerobic glycolysis is enormous. In fact, cells devote as much as 10% of their entire proteome and half of all of their metabolic genes to produce proteins involved in glycolysis (Madhukar et al., 2015). In contrast, biosynthetic programs in cells require much lower amounts of protein. Thus, the cost of producing proteins for aerobic glycolysis is as large, if not larger, than the cost of producing proteins for biosynthesis. These proposals are further challenged by the evidence showing that mitochondrial functions occur concomitantly with the Warburg Effect and thus limiting mitochondrial activity appears not to occur during the Warburg Effect. Ultimately, further research is needed to elucidate whether the Warburg Effect functions to support biosynthetic programs.

1.6 Warburg Effect and the tumor microenvironment

In contrast to the cell-intrinsic functions described in the previous sections, the Warburg Effect may present an advantage for cell growth in a multicellular environment. Acidification of the microenvironment and other metabolic crosstalk are intriguing possibilities. Elevated glucose metabolism decreases the pH in the microenvironment due to lactate secretion (Figure 1.2) (Estrella et al., 2013). The potential benefits of acidosis to cancer cells are multifold. An acid-mediated invasion hypothesis suggests that H^+ ions secreted from cancer cells diffuse into the surrounding environment and alter the tumor-stroma interface allowing for enhanced invasiveness (Estrella et al., 2013; Gatenby and Gawlinski, 1996). A recent study showed that tumor-derived lactate is a contributor to M2 tissue-associated macrophage (TAM) polarization (Colegio et al., 2014). Also as briefly mentioned previously, the availability of glucose appears to be a result of direct competition between tumor and tumor infiltrating lymphocytes (TIL) (Chang et al., 2015; Ho et al., 2015). The high rates of glycolysis limit the availability of glucose for TILs that require sufficient glucose for their effector functions. Supporting this proposal is direct evidence indicating that targeting aerobic glycolysis in the tumor has the added benefit of increasing the supply of glucose to TILs and thus boosting their main function which is to eradicate the tumor cells. Together, this body of evidence indicates that tumor cells can communicate with cells in the immune system to support pro-tumor immunity.

It is likely that the Warburg Effect provides an overall benefit that supports a tumor microenvironment conducive to cancer cell proliferation. However, the Warburg

Effect is thought to be an early event in oncogenesis that is an immediate consequence of an initial oncogenic mutation, such as that of *KRAS* in pancreatic cancer or *BRAF* in melanoma thus occurring before cell invasion and in benign and early stage lesions as well (Shain et al., 2015; Ying et al., 2012). Another issue is that in conditions completely isolated from the environment such as in the growth phase of unicellular yeast, the Warburg Effect remains the choice of energy metabolism from glucose (Molenaar et al., 2009). Altogether, these data suggest that non-cell-intrinsic functions of the Warburg Effect are insufficient to entirely explain its functions.

1.7 Warburg Effect and cell signaling

We and others have proposed that the Warburg Effect confers direct signaling functions to tumor cells (Hamanaka and Chandel, 2011; Locasale et al., 2011; Wellen et al., 2009; Wellen and Thompson, 2010, 2012). This proposal is particularly attractive since it identifies a direct causal role of altered glucose metabolism in promoting tumorigenesis through this signal transduction affecting other cellular processes. Two areas of signaling function are the generation and modulation of reactive oxygen species (ROS) and the modulation of chromatin state. Other studies have identified additional possible signaling mechanisms (Chang et al., 2013; Ho et al., 2015).

Maintaining the appropriate balance of ROS is essential (Sena and Chandel, 2012). Excessive ROS damages cell membranes, nucleic acids, and has other deleterious effects. Insufficient ROS disturbs signaling processes that are beneficial for cell proliferation, such as by inactivating phosphatase and tensin homolog (PTEN) and

tyrosine phosphatases. The Warburg Effect causes alterations in mitochondrial redox potential, ultimately changing ROS generation (Locasale et al., 2011).

An important determinant of redox potential in cells is the NADH that is available in the mitochondria for electron transport. Cellular mechanisms to maintain redox homeostasis are in place when glycolysis rates fluctuate. Up to a certain extent of glycolysis, the malate-aspartate shuttle through the mitochondria is able to restore the NADH imbalance (Locasale et al., 2011). However, when glycolysis rates are faster than what can be accommodated by the malate-aspartate shuttle, the conversion of pyruvate into lactate via lactate dehydrogenase (LDH) is able to regenerate NAD^+. This process may also affect the homeostasis of ROS generation by affecting the concentration of reducing equivalents in the mitochondria (Figure 1.2) (Locasale, 2012; Locasale et al., 2011). This consequence of the Warburg Effect may be directly involved in oncogene-induced senescence (OIS) (Kaplon et al., 2013). OIS has a tumor-suppressive cellular function and a recent study has reported that increased glucose oxidation through pyruvate dehydrogenase (PDH) can regulate OIS. This finding shows that the redox balance of NADH may contribute to direct signaling roles for the Warburg Effect.

In addition, metabolic pathways that stimulate redox homeostasis are upregulated alongside the Warburg Effect. For example, the pentose phosphate pathway coming from glycolysis generates NADPH. De novo serine metabolism, which feeds into the one-carbon metabolism, produces NADPH and glutathione, which modulate ROS levels (Fan et al., 2015; Mehrmohamadi et al., 2014). Together these findings provide direct biochemical links between aerobic glycolysis and ROS availability that could in turn

affect myriad signaling processes.

In addition to cell signaling through ROS, a signaling link between glucose metabolism and histone acetylation has been well documented (Cluntun et al., 2015; Evertts et al., 2013; Liu et al., 2015; Lu and Thompson, 2012). The status of chromatin structure is responsible for regulating different cellular functions including DNA repair and gene transcription. It has been established that acetyl-CoA, the substrate for histone acetylation, can be regulated by glucose flux (Evertts et al., 2013). Studies have shown that there is a direct link between cellular metabolism and regulation of growth genes and that intracellular acetyl-CoA levels may represent a widely conserved mechanism that promotes this important link (Cai et al., 2011). The activity of ATP-citrate lyase, the enzyme responsible for converting citrate into acetyl-CoA can influence histone acetylation levels (Wellen et al., 2009). Elevated levels of acetyl-CoA may be enough to drive cells into growth phase via histone acetylation (Lu and Thompson, 2012). Removal of glucose or reduction of ATP-citrate lyase results in loss of acetylation on several histones and causes decreased transcription of genes involved in glucose metabolism. This indicates that there is some interplay between glucose metabolism and histone acetylation. Supporting this idea, glycolytic metabolism has been found to impact chromatin structure (Liu et al., 2015).

In addition to histone acetylation responding to glucose availability in cells, deacetylation can be influenced by nutrient availability as well (Wellen and Thompson, 2012). Deacetylation plays an important role in nutrient sensing and signaling since the activity of multiple deacetylases are modulated by NAD^+ levels. More specifically, the

ratio of NAD^+/NADH increases in nutrient-deprived conditions (Cluntun et al., 2015; Lu and Thompson, 2012; Wellen and Thompson, 2012). Therefore, both acetylation and deacetylation can be influenced by nutrient availability, indicating that their statuses may be consequences of the Warburg Effect. These multiple lines of evidence point to glycolysis having cell signaling functions.

However, difficulties also limit this proposal from being the general mechanism that benefits cancer cells by undergoing aerobic glycolysis. One such limitation is that it is hard to imagine how molecular specificity arises through such a gross global signaling mechanism. In contrast to, for example, growth factor signaling in which ligand-binding to a substrate induces conformational and enzymatic activity changes that affect specific cellular processes, a mechanism whereby the state of glycolysis signals to other cellular processes lacks obvious sources of specificity. Another limitation is that such proposals typically lack falsifiability. This means it is extremely difficult to design experiments to conclusively show that a specific signaling mechanism, such as chromatin structure modulation, directly comes from the status of glucose metabolism as the key benefit for aerobic glycolysis. One reason for this is that the biochemical interaction occurs rapidly but the cellular phenotypic alterations evolve over much longer times resulting in many confounding factors that occur along the way. Genetic models that could test these hypotheses are difficult to conceive, and other experiments lack the ability to test whether specific cellular outcomes occur through such signaling mechanisms and not through indirect means. The extent to which these general features, such as ROS signaling homeostasis and chromatin structure organization, are key events in tumorigenesis also

remains unclear (DeNicola et al., 2011). In the future, such specificity and ability to experimentally test these hypotheses may come from observing quantitative aspects of the mechanism as has been shown in other studies of signal transduction. Experiments that can precisely control the levels of acetyl-CoA and ROS could allow for one to decouple many of the downstream effects of the Warburg Effect.

1.8 Warburg Effect and therapeutic targeting

Because the Warburg Effect has been very well-documented for nearly a century with clear evidence that it is the most prevalent metabolic rewiring process found in cancer, there have been tremendous efforts put forth to therapeutically target it (Galluzzi et al., 2013; Luengo et al., 2017). 2-deoxyglucose (2DG) has been thoroughly explored in the past years as an inhibitor of glycolysis. 2DG is an analog of glucose which is phosphorylated by HK2 to produce 2-deoxyglucose-6-phosphate, which cannot be further metabolized by the cell (Zhang et al., 2006). While 2DG has been shown to be effective at inhibition of glycolysis in cell culture with important functional outputs to affect signaling such as chromatin regulation (Cluntun et al., 2015; Zhang et al., 2014), there have been numerous challenges associated with translation of 2DG clinically. Preclinically, 2DG has been shown to exert differential effects on cells depending on its concentration. At low concentrations, 2DG affects glycolytic rate through various mechanisms (Chen and Gueron, 1992; Cluntun et al., 2015; Vander Heiden, 2011), but at higher concentrations, it acts as an inhibitor of HK (Kurtoglu et al., 2007; Nirenberg and Hogg, 1958). Thus, the pharmacological effects that 2DG exerts on cells are not well-

defined. Moreover, in early clinical trials 2DG was used at concentrations that effectively inhibit HK to achieve tumor growth inhibition, but major side effects were found including hypoglycemia (Landau et al., 1958). In more recent clinical trials, 2DG was tested again as an anti-cancer therapy, but this time at lower doses, which was insufficient to limit tumor progression (Raez et al., 2013).

Various inhibitors of GAPDH, the sixth enzymatic step in glycolysis, have been developed. 3-bromopyruvate (3BP) has been explored as a GAPDH inhibitor. It has been shown to inhibit GAPDH through a pyruvylation reaction via an irreversible covalent bond with its pyruvyl moiety (Ganapathy-Kanniappan et al., 2009). However, due to its high reactivity with sulfhydryl and hydroxyl groups, it has also been previously reported to inhibit various other enzymes and pathways (Baker and Rabin, 1969; Bendrat et al., 1997; Chen et al., 2009; Dell'Antone, 2006; Ming-Hua et al., 1996), thus limiting its efficacy as an anti-cancer therapy. Iodoacetate (IA) has also been shown to inhibit glycolysis via alkylation of the cysteine residue in GAPDH (Sabri and Ochs, 1971; Williamson, 1967). However, similar to 3BP, IA is promiscuous for cysteine residues (Gundlach et al., 1959a; Gundlach et al., 1959b; Schmidt and Dringen, 2009), severely limiting its efficacy clinically. A potentially promising GAPDH inhibitor is koningic acid (KA), or heptelidic acid, which is a natural product and has been shown in the literature to alkylate the cysteine residue of the catalytic site of GAPDH (Endo et al., 1985; Sakai et al., 1988, 1991). While KA is also an alkylating agent, it has been shown to have high binding affinity for GAPDH *in vitro* and is also secreted from fungal species that express two GAPDH isozymes: a KA-sensitive and KA-resistant GAPDH isozyme (Sakai et al.,

1990; Watanabe et al., 1993), suggesting further its likely specificity for GAPDH. Its potential as an anti-cancer therapy and GAPDH inhibitor is further explored in the subsequent chapter. Lastly, vitamin C has recently been explored as a GAPDH inhibitor in which at high concentrations, it acts as an oxidant rather than an anti-oxidant and can inhibit GAPDH and limits tumor progression (Yun et al., 2015). However, it does so by generating reactive oxygen species (ROS) in the cells, which then inactivates GAPDH, thus inducing numerous other changes in cells due to accumulating oxidative stress.

In addition, pyruvate kinase M2 (PKM2) is another enzyme in glycolysis, which catalyzes the conversion of phosphoenolpyruvate (PEP) to pyruvate, that has been thought to be linked to the Warburg Effect (Christofk et al., 2008; Israelsen et al., 2013; Lunt et al., 2015). It is an isoform that differs from PKM1 by 56 amino acids, which allows PKM2 to be allosterically regulated by fructose 1,6-bisphosphate (F 1,6-BP), but not PKM1 (Dombrauckas et al., 2005). Thus, there have been numerous efforts to therapeutically exploit the unique site of PKM2 (Dayton et al., 2016). Studies have shown that compound 3 from a compound library screen inhibited the allosteric site of PKM2 (Vander Heiden et al., 2010). However, it also showed non-specific binding also to PKL and PKR, the PK liver and red blood cell isoforms respectively. Other studies found shikonin and alkannin to specifically bind PKM2 at low concentrations, but PKM1 and PKL at higher concentrations (Chen et al., 2011). Therefore, despite the therapeutic efforts made to target PKM2, there has not been significant progress made clinically. Moreover, there have been questions around the role of pyruvate kinase in cancer and in the Warburg Effect. A recent study has implicated PKM1, rather than PKM2, as a

significant contributor to tumor progression (Morita et al., 2018). Thus, more work is necessary to elucidate the role of pyruvate kinase in the Warburg Effect.

Dichloroacetate (DCA) is clinically used for the treatment of lactic acidosis and has been widely studied as a glycolytic inhibitor in cancer (Michelakis et al., 2008). DCA has been shown to inhibit the pyruvate dehydrogenase kinase, thus activating pyruvate dehydrogenase to allow pyruvate catabolism in the mitochondria via pyruvate decarboxylation (Hitosugi et al., 2011). While DCA has shown efficacy in early clinical trials for the treatment of various cancers including glioblastoma and non-Hodgkin's lymphoma (Michelakis et al., 2010; Strum et al., 2013), it is unclear whether the shift to oxidative glucose metabolism is the mechanism by which DCA exerts anti-tumor effects (Bonnet et al., 2007; Shen et al., 2013).

Thus, there is a surge of interest in targeting glycolytic enzymes because many types of cancer undergo the Warburg Effect. However, there remain overall challenges attributed to toxicity, off-target effects, and limited efficacy. Therefore, there is still much work needed to be done to elucidate effective therapeutic strategies to target the Warburg Effect and achieve efficacy in cancers, while also limiting toxicity to surrounding healthy tissues.

1.9 Perspective

Extensive research on the Warburg Effect and its functions in cancer cells have advanced our understanding of its causes and requirements for tumor cell proliferation (Koppenol et al., 2011; Locasale, 2012). However, it has left us with a surprising lack of

clarity regarding its ontology. These uncertainties should challenge us to better understand its function in promoting tumor growth. It is likely we will require a better understanding of the biology of Warburg Effect if therapeutic advances are to be made in treating and preventing cancer using dietary and pharmacological intervention in metabolism, which are currently subjects of intense interest.

1.10 Scope of this dissertation

In this dissertation, I focus on identifying strategies for selectively targeting the Warburg Effect. To this end, I use a metabolomic, pharmacological, genetic, and systematic approach to identify targetable enzymes in cancers in both glucose metabolism and serine synthesis, which branches from glycolysis. I also elucidate distinguishable factors between the Warburg Effect, glycolysis, and fully oxidative glucose metabolism.

In chapter 2, I investigate GAPDH as a potential therapeutic target in cancer with KA. Using global metabolite profiling, I determine that of several putative GAPDH inhibitors, KA is the only one that affects glycolysis and related central carbon metabolism pathways. Using genetic approaches, I confirm that KA is a highly specific GAPDH inhibitor. Most notably, I show that the response to KA is predicted only by the quantitative extent of the Warburg Effect, which was validated both in cell culture and in mice.

In chapter 3, I use KA as a tool to investigate the biology of the Warburg Effect, which is important for advancing therapeutic efforts of targeting the Warburg Effect in cancer. I develop an evolved resistance to KA model that allows acquired resistant cells

to transition into a state away from the Warburg Effect. Using this model, I find that KA-acquired resistant cells evolve a loss of the Warburg Effect, but remain dependent on glycolysis with distinct functional metabolic outputs compared to KA-sensitive cells.

Lastly in chapter 4, I explore therapeutic targeting of PHGDH which diverts glucose metabolism into serine biosynthesis. My collaborators in Dr. Luhua Lai's lab at Peking University developed two allosteric inhibitors of PHGDH. Using CRISPR-*Cas9* technology, I genetically knocked out *PHGDH* from cells as a tool to demonstrate specificity of the inhibitors to PHGDH. Further, I find that allosteric inhibition of PHGDH with both inhibitors results in decreased *de novo* serine and glycine production, as well as decreases in downstream metabolism from serine biosynthesis.

Overall, this dissertation aims to use systems biology, metabolomics, genetics, and pharmacological approaches to elucidate strategies for targeting the Warburg Effect in cancer. The described work accomplishes this by identifying KA as a specific GAPDH inhibitor under conditions of the Warburg Effect, resolving the Warburg Effect as a distinct entity from glycolysis, and exploiting PHGDH as a therapeutic target in cancer. Together, these findings significantly contribute to advancing multiple fields in cancer including metabolism, systems biology, and precision medicine with rationale for utilizing metabolic factors as a paradigm for cancer therapy.

1.11 References

Baker, J., and Rabin, B. (1969). Effects of bromopyruvate on the control and catalytic properties of glutamate dehydrogenase. European journal of biochemistry *11*, 154-159.

Bendrat, K., Al-Abed, Y., Callaway, D.J., Peng, T., Calandra, T., Metz, C.N., and Bucala, R. (1997). Biochemical and mutational investigations of the enzymatic activity of macrophage migration inhibitory factor. Biochemistry *36*, 15356-15362.

Birnbaum, M.J., Haspel, H.C., and Rosen, O.M. (1987). Transformation of rat fibroblasts by FSV rapidly increases glucose transporter gene transcription. Science *235*, 1495-1498.

Birsoy, K., Wang, T., Chen, W.W., Freinkman, E., Abu-Remaileh, M., and Sabatini, D.M. (2015). An Essential Role of the Mitochondrial Electron Transport Chain in Cell Proliferation Is to Enable Aspartate Synthesis. Cell *162*, 540-551.

Boerner, P., Resnick, R.J., and Racker, E. (1985). Stimulation of glycolysis and amino acid uptake in NRK-49F cells by transforming growth factor beta and epidermal growth factor. Proceedings of the National Academy of Sciences of the United States of America *82*, 1350-1353.

Bonnet, S., Archer, S.L., Allalunis-Turner, J., Haromy, A., Beaulieu, C., Thompson, R., Lee, C.T., Lopaschuk, G.D., Puttagunta, L., and Bonnet, S. (2007). A mitochondria-K+ channel axis is suppressed in cancer and its normalization promotes apoptosis and inhibits cancer growth. Cancer cell *11*, 37-51.

Boroughs, L.K., and DeBerardinis, R.J. (2015). Metabolic pathways promoting cancer cell survival and growth. Nat Cell Biol *17*, 351-359.

Cai, L., Sutter, B.M., Li, B., and Tu, B.P. (2011). Acetyl-CoA induces cell growth and proliferation by promoting the acetylation of histones at growth genes. Molecular cell *42*, 426-437.

Cairns, R.A., Harris, I.S., and Mak, T.W. (2011). Regulation of cancer cell metabolism. Nat Rev Cancer *11*, 85-95.

Carracedo, A., Cantley, L.C., and Pandolfi, P.P. (2013). Cancer metabolism: fatty acid oxidation in the limelight. Nature reviews Cancer *13*, 227-232.

Chang, C.-H., Curtis, J.D., Maggi, L.B., Faubert, B., Villarino, A.V., O'Sullivan, D., Huang, S.C.-C., van der Windt, G.J., Blagih, J., and Qiu, J. (2013). Posttranscriptional control of T cell effector function by aerobic glycolysis. Cell *153*, 1239-1251.

Chang, C.-H., Qiu, J., O'Sullivan, D., Buck, M.D., Noguchi, T., Curtis, J.D., Chen, Q., Gindin, M., Gubin, M.M., and van der Windt, G.J. (2015). Metabolic Competition in the Tumor Microenvironment Is a Driver of Cancer Progression. Cell.

Chen, J., Xie, J., Jiang, Z., Wang, B., Wang, Y., and Hu, X. (2011). Shikonin and its analogs inhibit cancer cell glycolysis by targeting tumor pyruvate kinase-M2. Oncogene *30*, 4297.

Chen, W., and Gueron, M. (1992). The inhibition of bovine heart hexokinase by 2-deoxy-D-glucose-6-phosphate: characterization by 31P NMR and metabolic implications. Biochimie *74*, 867-873.

Chen, Z., Zhang, H., Lu, W., and Huang, P. (2009). Role of mitochondria-associated hexokinase II in cancer cell death induced by 3-bromopyruvate. Biochimica et biophysica acta *1787*, 553-560.

Christofk, H.R., Vander Heiden, M.G., Harris, M.H., Ramanathan, A., Gerszten, R.E., Wei, R., Fleming, M.D., Schreiber, S.L., and Cantley, L.C. (2008). The M2 splice isoform of pyruvate kinase is important for cancer metabolism and tumour growth. Nature *452*, 230-U274.
Cluntun, A.A., Huang, H., Dai, L., Liu, X., Zhao, Y., and Locasale, J.W. (2015). The rate of glycolysis quantitatively mediates specific histone acetylation sites. Cancer Metab *3*, 10.
Colegio, O.R., Chu, N.Q., Szabo, A.L., Chu, T., Rhebergen, A.M., Jairam, V., Cyrus, N., Brokowski, C.E., Eisenbarth, S.C., Phillips, G.M.*, et al.* (2014). Functional polarization of tumour-associated macrophages by tumour-derived lactic acid. Nature *513*, 559-563.
Crabtree, H.G. (1929). Observations on the carbohydrate metabolism of tumours. Biochemical journal *23*, 536.
Dang, C.V. (2012). Links between metabolism and cancer. Gene Dev *26*, 877-890.
Dayton, T.L., Jacks, T., and Vander Heiden, M.G. (2016). PKM2, cancer metabolism, and the road ahead. EMBO reports, e201643300.
DeBerardinis, R.J., and Chandel, N.S. (2016). Fundamentals of cancer metabolism. Sci Adv *2*, e1600200.
DeBerardinis, R.J., Lum, J.J., Hatzivassiliou, G., and Thompson, C.B. (2008). The biology of cancer: metabolic reprogramming fuels cell growth and proliferation. Cell Metab *7*, 11-20.
Dell'Antone, P. (2006). Inactivation of H+-vacuolar ATPase by the energy blocker 3-bromopyruvate, a new antitumour agent. Life sciences *79*, 2049-2055.
DeNicola, G.M., Karreth, F.A., Humpton, T.J., Gopinathan, A., Wei, C., Frese, K., Mangal, D., Kenneth, H.Y., Yeo, C.J., and Calhoun, E.S. (2011). Oncogene-induced Nrf2 transcription promotes ROS detoxification and tumorigenesis. Nature *475*, 106-109.
Dombrauckas, J.D., Santarsiero, B.D., and Mesecar, A.D. (2005). Structural basis for tumor pyruvate kinase M2 allosteric regulation and catalysis. Biochemistry *44*, 9417-9429.
Endo, A., Hasumi, K., Sakai, K., and Kanbe, T. (1985). Specific inhibition of glyceraldehyde-3-phosphate dehydrogenase by koningic acid (heptelidic acid). The Journal of antibiotics *38*, 920-925.
Epstein, T., Xu, L., Gillies, R.J., and Gatenby, R.A. (2014). Separation of metabolic supply and demand: aerobic glycolysis as a normal physiological response to fluctuating energetic demands in the membrane. Cancer Metab *2*.
Estrella, V., Chen, T., Lloyd, M., Wojtkowiak, J., Cornnell, H.H., Ibrahim-Hashim, A., Bailey, K., Balagurunathan, Y., Rothberg, J.M., Sloane, B.F.*, et al.* (2013). Acidity generated by the tumor microenvironment drives local invasion. Cancer Res *73*, 1524-1535.
Evertts, A.G., Zee, B.M., DiMaggio, P.A., Gonzales-Cope, M., Coller, H.A., and Garcia, B.A. (2013). Quantitative Dynamics of the Link between Cellular Metabolism and Histone Acetylation. Journal of Biological Chemistry *288*, 12142-12151.
Fan, J., Teng, X., Liu, L., Mattaini, K.R., Looper, R.E., Vander Heiden, M.G., and Rabinowitz, J.D. (2015). Human phosphoglycerate dehydrogenase produces the oncometabolite D-2-hydroxyglutarate. ACS Chem Biol *10*, 510-516.

Fantin, V.R., St-Pierre, J., and Leder, P. (2006). Attenuation of LDH-A expression uncovers a link between glycolysis, mitochondrial physiology, and tumor maintenance. Cancer cell *9*, 425-434.
Flaveny, C.A., Griffett, K., El-Gendy Bel, D., Kazantzis, M., Sengupta, M., Amelio, A.L., Chatterjee, A., Walker, J., Solt, L.A., Kamenecka, T.M.*, et al.* (2015). Broad Anti-tumor Activity of a Small Molecule that Selectively Targets the Warburg Effect and Lipogenesis. Cancer cell *28*, 42-56.
Flier, J.S., Mueckler, M.M., Usher, P., and Lodish, H.F. (1987). Elevated levels of glucose transport and transporter messenger RNA are induced by ras or src oncogenes. Science *235*, 1492-1495.
Galluzzi, L., Kepp, O., Vander Heiden, M.G., and Kroemer, G. (2013). Metabolic targets for cancer therapy. Nat Rev Drug Discov *12*, 829-846.
Ganapathy-Kanniappan, S., Geschwind, J.F.H., Kunjithapatham, R., Buijs, M., Vossen, J.A., Tchernyshyov, I., Cole, R.N., Syed, L.H., Rao, P.P., Ota, S.*, et al.* (2009). Glyceraldehyde-3-phosphate Dehydrogenase (GAPDH) Is Pyruvylated during 3-Bromopyruvate Mediated Cancer Cell Death. Anticancer Research *29*, 4909-4918.
Gatenby, R.A., and Gawlinski, E.T. (1996). A reaction-diffusion model of cancer invasion. Cancer research *56*, 5745-5753.
Gundlach, H.G., Moore, S., and Stein, W.H. (1959a). The reaction of iodoacetate with methionine. Journal of Biological Chemistry *234*, 1761-1764.
Gundlach, H.G., Stein, W.H., and Moore, S. (1959b). The nature of the amino acid residues involved in the inactivation of ribonuclease by iodoacetate. Journal of Biological Chemistry *234*, 1754-1760.
Hamanaka, R.B., and Chandel, N.S. (2011). Warburg effect and redox balance. Science *334*, 1219-1220.
Hermsen, R., Okano, H., You, C., Werner, N., and Hwa, T. (2015). A growth-rate composition formula for the growth of E.coli on co-utilized carbon substrates. Molecular systems biology *11*, 801.
Hiraki, Y., Rosen, O.M., and Birnbaum, M.J. (1988). Growth factors rapidly induce expression of the glucose transporter gene. The Journal of biological chemistry *263*, 13655-13662.
Hitosugi, T., Fan, J., Chung, T.-W., Lythgoe, K., Wang, X., Xie, J., Ge, Q., Gu, T.-L., Polakiewicz, R.D., and Roesel, J.L. (2011). Tyrosine phosphorylation of mitochondrial pyruvate dehydrogenase kinase 1 is important for cancer metabolism. Molecular cell *44*, 864-877.
Ho, P.-C., Bihuniak, J.D., Macintyre, A.N., Staron, M., Liu, X., Amezquita, R., Tsui, Y.-C., Cui, G., Micevic, G., and Perales, J.C. (2015). Phosphoenolpyruvate Is a Metabolic Checkpoint of Anti-tumor T Cell Responses. Cell.
Hui, S., Silverman, J.M., Chen, S.S., Erickson, D.W., Basan, M., Wang, J., Hwa, T., and Williamson, J.R. (2015). Quantitative proteomic analysis reveals a simple strategy of global resource allocation in bacteria. Molecular systems biology *11*, 784.
Israelsen, W.J., Dayton, T.L., Davidson, S.M., Fiske, B.P., Hosios, A.M., Bellinger, G., Li, J., Yu, Y., Sasaki, M., and Horner, J.W. (2013). PKM2 isoform-specific deletion reveals a differential requirement for pyruvate kinase in tumor cells. Cell *155*, 397-409.

Kaplon, J., Zheng, L., Meissl, K., Chaneton, B., Selivanov, V.A., Mackay, G., van der Burg, S.H., Verdegaal, E.M., Cascante, M., Shlomi, T., *et al.* (2013). A key role for mitochondrial gatekeeper pyruvate dehydrogenase in oncogene-induced senescence. Nature *498*, 109-112.
Koppenol, W.H., Bounds, P.L., and Dang, C.V. (2011). Otto Warburg's contributions to current concepts of cancer metabolism. Nature Reviews Cancer *11*, 325-337.
Kurtoglu, M., Maher, J.C., and Lampidis, T.J. (2007). Differential toxic mechanisms of 2-deoxy-D-glucose versus 2-fluorodeoxy-D-glucose in hypoxic and normoxic tumor cells. Antioxidants & redox signaling *9*, 1383-1390.
Landau, B.R., Laszlo, J., Stengle, J., and Burk, D. (1958). Certain metabolic and pharmacologic effects in cancer patients given infusions of 2-deoxy-D-glucose. Journal of the National Cancer Institute *21*, 485-494.
Levine, A.J., and Puzio-Kuter, A.M. (2010). The control of the metabolic switch in cancers by oncogenes and tumor suppressor genes. Science *330*, 1340-1344.
Liu, X.-S., Little, J.B., and Yuan, Z.-M. (2015). Glycolytic metabolism influences global chromatin structure. Oncotarget *6*, 4214.
Locasale, J.W. (2012). The consequences of enhanced cell-autonomous glucose metabolism. Trends Endocrinol Metab *23*, 545-551.
Locasale, J.W., and Cantley, L.C. (2011). Metabolic flux and the regulation of mammalian cell growth. Cell Metab *14*, 443-451.
Locasale, J.W., Grassian, A.R., Melman, T., Lyssiotis, C.A., Mattaini, K.R., Bass, A.J., Heffron, G., Metallo, C.M., Muranen, T., Sharfi, H., *et al.* (2011). Phosphoglycerate dehydrogenase diverts glycolytic flux and contributes to oncogenesis. Nat Genet *43*, 869-874.
Lu, C., and Thompson, C.B. (2012). Metabolic regulation of epigenetics. Cell metabolism *16*, 9-17.
Luengo, A., Gui, D.Y., and Vander Heiden, M.G. (2017). Targeting Metabolism for Cancer Therapy. Cell Chem Biol *24*, 1161-1180.
Lunt, S.Y., Muralidhar, V., Hosios, A.M., Israelsen, W.J., Gui, D.Y., Newhouse, L., Ogrodzinski, M., Hecht, V., Xu, K., and Acevedo, P.N.M. (2015). Pyruvate kinase isoform expression alters nucleotide synthesis to impact cell proliferation. Molecular cell *57*, 95-107.
Lunt, S.Y., and Vander Heiden, M.G. (2011). Aerobic glycolysis: meeting the metabolic requirements of cell proliferation. Annu Rev Cell Dev Biol *27*, 441-464.
Madhukar, N.S., Warmoes, M.O., and Locasale, J.W. (2015). Organization of enzyme concentration across the metabolic network in cancer cells. PLoS One *10*, e0117131.
Mehrmohamadi, M., Liu, X., Shestov, A.A., and Locasale, J.W. (2014). Characterization of the usage of the serine metabolic network in human cancer. Cell reports *9*, 1507-1519.
Michelakis, E., Webster, L., and Mackey, J. (2008). Dichloroacetate (DCA) as a potential metabolic-targeting therapy for cancer. British journal of cancer *99*, 989.
Michelakis, E.D., Sutendra, G., Dromparis, P., Webster, L., Haromy, A., Niven, E., Maguire, C., Gammer, T.L., Mackey, J.R., Fulton, D., *et al.* (2010). Metabolic modulation of glioblastoma with dichloroacetate. Sci Transl Med *2*, 31ra34.
Ming-Hua, W., Zhi-Xin, W., and Kang-Yuan, Z. (1996). Kinetics of inactivation of

bovine pancreatic ribonuclease A by bromopyruvic acid. Biochemical Journal *320*, 187-192.
Molenaar, D., van Berlo, R., de Ridder, D., and Teusink, B. (2009). Shifts in growth strategies reflect tradeoffs in cellular economics. Molecular systems biology *5*, 323.
Morita, M., Sato, T., Nomura, M., Sakamoto, Y., Inoue, Y., Tanaka, R., Ito, S., Kurosawa, K., Yamaguchi, K., and Sugiura, Y. (2018). PKM1 confers metabolic advantages and promotes cell-autonomous tumor cell growth. Cancer cell *33*, 355-367. e357.
Nirenberg, M.W., and Hogg, J.F. (1958). Inhibition of anaerobic glycolysis in Ehrlich ascites tumor cells by 2-deoxy-D-glucose. Cancer research *18*, 518-521.
Patra, K.C., Wang, Q., Bhaskar, P.T., Miller, L., Wang, Z., Wheaton, W., Chandel, N., Laakso, M., Muller, W.J., Allen, E.L.*, et al.* (2013). Hexokinase 2 is required for tumor initiation and maintenance and its systemic deletion is therapeutic in mouse models of cancer. Cancer cell *24*, 213-228.
Pavlova, N.N., and Thompson, C.B. (2016). The Emerging Hallmarks of Cancer Metabolism. Cell Metab *23*, 27-47.
Pfeiffer, T., Schuster, S., and Bonhoeffer, S. (2001). Cooperation and competition in the evolution of ATP-producing pathways. Science *292*, 504-507.
Racker, E. (1972). Bioenergetics and the Problem of Tumor Growth: An understanding of the mechanism of the generation and control of biological energy may shed light on the problem of tumor growth. American scientist, 56-63.
Raez, L.E., Papadopoulos, K., Ricart, A.D., Chiorean, E.G., Dipaola, R.S., Stein, M.N., Rocha Lima, C.M., Schlesselman, J.J., Tolba, K., Langmuir, V.K.*, et al.* (2013). A phase I dose-escalation trial of 2-deoxy-D-glucose alone or combined with docetaxel in patients with advanced solid tumors. Cancer Chemother Pharmacol *71*, 523-530.
Sabri, M., and Ochs, S. (1971). Inhibition of glyceraldehyde-3-phosphate dehydrogenase in mammalian nerve by iodoacetic acid. Journal of neurochemistry *18*, 1509-1514.
Sakai, K., Hasumi, K., and Endo, A. (1988). Inactivation of rabbit muscle glyceraldehyde-3-phosphate dehydrogenase by koningic acid. Biochim Biophys Acta *952*, 297-303.
Sakai, K., Hasumi, K., and Endo, A. (1990). Two glyceraldehyde-3-phosphate dehydrogenase isozymes from the koningic acid (heptelidic acid) producer Trichoderma koningii. European journal of biochemistry / FEBS *193*, 195-202.
Sakai, K., Hasumi, K., and Endo, A. (1991). Identification of koningic acid (heptelidic acid)-modified site in rabbit muscle glyceraldehyde-3-phosphate dehydrogenase. Biochim Biophys Acta *1077*, 192-196.
Schmidt, M., and Dringen, R. (2009). Differential effects of iodoacetamide and iodoacetate on glycolysis and glutathione metabolism of cultured astrocytes. Frontiers in neuroenergetics *1*, 1.
Sena, L.A., and Chandel, N.S. (2012). Physiological roles of mitochondrial reactive oxygen species. Mol Cell *48*, 158-167.
Shain, A.H., Yeh, I., Kovalyshyn, I., Sriharan, A., Talevich, E., Gagnon, A., Dummer, R., North, J., Pincus, L., Ruben, B.*, et al.* (2015). The Genetic Evolution of Melanoma from Precursor Lesions. N Engl J Med *373*, 1926-1936.
Shen, Y., Ou, D., Hsu, C., Lin, K., Chang, C., Lin, C., Liu, S., and Cheng, A. (2013).

Activating oxidative phosphorylation by a pyruvate dehydrogenase kinase inhibitor overcomes sorafenib resistance of hepatocellular carcinoma. British journal of cancer *108*, 72.
Shestov, A.A., Liu, X., Ser, Z., Cluntun, A.A., Hung, Y.P., Huang, L., Kim, D., Le, A., Yellen, G., Albeck, J.G.*, et al.* (2014). Quantitative determinants of aerobic glycolysis identify flux through the enzyme GAPDH as a limiting step. Elife *3*, e03342.
Shim, H., Chun, Y.S., Lewis, B.C., and Dang, C.V. (1998). A unique glucose-dependent apoptotic pathway induced by c-Myc. Proceedings of the National Academy of Sciences *95*, 1511-1516.
Shlomi, T., Benyamini, T., Gottlieb, E., Sharan, R., and Ruppin, E. (2011). Genome-scale metabolic modeling elucidates the role of proliferative adaptation in causing the Warburg effect. PLoS computational biology *7*, e1002018.
Slavov, N., Budnik, B.A., Schwab, D., Airoldi, E.M., and van Oudenaarden, A. (2014). Constant growth rate can be supported by decreasing energy flux and increasing aerobic glycolysis. Cell reports *7*, 705-714.
Strum, S.B., Adalsteinsson, Ö., Black, R.R., Segal, D., Peress, N.L., and Waldenfels, J. (2013). Case report: sodium dichloroacetate (DCA) inhibition of the "Warburg Effect" in a human cancer patient: complete response in non-Hodgkin's lymphoma after disease progression with rituximab-CHOP. Journal of bioenergetics and biomembranes *45*, 307-315.
Sullivan, L.B., Gui, D.Y., Hosios, A.M., Bush, L.N., Freinkman, E., and Vander Heiden, M.G. (2015). Supporting Aspartate Biosynthesis Is an Essential Function of Respiration in Proliferating Cells. Cell *162*, 552-563.
Vander Heiden, M.G. (2011). Targeting cancer metabolism: a therapeutic window opens. Nat Rev Drug Discov *10*, 671-684.
Vander Heiden, M.G., Cantley, L.C., and Thompson, C.B. (2009). Understanding the Warburg effect: the metabolic requirements of cell proliferation. Science *324*, 1029-1033.
Vander Heiden, M.G., Christofk, H.R., Schuman, E., Subtelny, A.O., Sharfi, H., Harlow, E.E., Xian, J., and Cantley, L.C. (2010). Identification of small molecule inhibitors of pyruvate kinase M2. Biochemical pharmacology *79*, 1118-1124.
Vander Heiden, M.G., and DeBerardinis, R.J. (2017). Understanding the Intersections between Metabolism and Cancer Biology. Cell *168*, 657-669.
Vazquez, A., Liu, J., Zhou, Y., and Oltvai, Z.N. (2010). Catabolic efficiency of aerobic glycolysis: the Warburg effect revisited. BMC systems biology *4*, 58.
Viale, A., Pettazzoni, P., Lyssiotis, C.A., Ying, H., Sanchez, N., Marchesini, M., Carugo, A., Green, T., Seth, S., Giuliani, V.*, et al.* (2014). Oncogene ablation-resistant pancreatic cancer cells depend on mitochondrial function. Nature *514*, 628-632.
Warburg, O. (1925). The metabolism of carcinoma cells. The Journal of Cancer Research *9*, 148-163.
Warburg, O. (1956). On the origin of cancer cells. Science *123*, 309-314.
Warburg, O., Posener, K., and Negelein, E. (1924). Ueber den stoffwechsel der tumoren. Biochemische Zeitschrift *152*, 319-344.
Warburg, O., Wind, F., and Negelein, E. (1927). The Metabolism of Tumors in the Body. J Gen Physiol *8*, 519-530.

Ward, P.S., and Thompson, C.B. (2012). Metabolic reprogramming: a cancer hallmark even warburg did not anticipate. Cancer cell *21*, 297-308.
Watanabe, H., Hasumi, K., Fukushima, Y., Sakai, K., and Endo, A. (1993). Cloning of two isozymes of Trichoderma koningii glyceraldehyde-3-phosphate dehydrogenase with different sensitivity to koningic acid. Biochim Biophys Acta *1172*, 43-48.
Wellen, K.E., Hatzivassiliou, G., Sachdeva, U.M., Bui, T.V., Cross, J.R., and Thompson, C.B. (2009). ATP-citrate lyase links cellular metabolism to histone acetylation. Science *324*, 1076-1080.
Wellen, K.E., and Thompson, C.B. (2010). Cellular metabolic stress: considering how cells respond to nutrient excess. Molecular cell *40*, 323-332.
Wellen, K.E., and Thompson, C.B. (2012). A two-way street: reciprocal regulation of metabolism and signalling. Nature reviews Molecular cell biology *13*, 270-276.
Williamson, J.R. (1967). Glycolytic control mechanisms III. Effects of iodoacetamide and fluoroacetate on glucose metabolism in the perfused rat heart. Journal of Biological Chemistry *242*, 4476-4485.
Ying, H.Q., Kimmelman, A.C., Lyssiotis, C.A., Hua, S.J., Chu, G.C., Fletcher-Sananikone, E., Locasale, J.W., Son, J., Zhang, H.L., Coloff, J.L.*, et al.* (2012). Oncogenic Kras Maintains Pancreatic Tumors through Regulation of Anabolic Glucose Metabolism. Cell *149*, 656-670.
Yun, J., Mullarky, E., Lu, C., Bosch, K.N., Kavalier, A., Rivera, K., Roper, J., Chio, II, Giannopoulou, E.G., Rago, C.*, et al.* (2015). Vitamin C selectively kills KRAS and BRAF mutant colorectal cancer cells by targeting GAPDH. Science *350*, 1391-1396.
Zhang, D., Li, J., Wang, F., Hu, J., Wang, S., and Sun, Y. (2014). 2-Deoxy-D-glucose targeting of glucose metabolism in cancer cells as a potential therapy. Cancer letters *355*, 176-183.
Zhang, X.D., Deslandes, E., Villedieu, M., Poulain, L., Duval, M., Gauduchon, P., Schwartz, L., and Icard, P. (2006). Effect of 2-Deoxy-D-glucose on various malignant cell lines in vitro. Anticancer Research *26*, 3561-3566.

CHAPTER 2: A PREDICTIVE MODEL FOR SELECTIVE TARGETING OF THE WARBURG EFFECT THROUGH GAPDH INHIBITION WITH A NATURAL PRODUCT[2]

2.1 Background and context

Since glucose is an essential carbon source, cancer cells adapt their metabolic network to increase glucose uptake and lactate secretion through the Warburg Effect (WE). Because the WE is prevalent among many cancer types, targeting glucose metabolism in cancer has shown promise, but its therapeutic window is poorly defined. In contrast to therapies that use genetics to predict outcome, predictors of metabolic therapies are more complex due to metabolic diversity. In this chapter, I use a systems-level approach to identify glyceraldehyde-3-phosphate dehydrogenase (GAPDH), which has rate-limiting properties during the Warburg Effect (WE), as a therapeutic target in cancer and tumor cells. I further show that a natural product, koningic acid (KA), is a highly specific and selective GAPDH inhibitor and that KA response in cancer is predicted only by the quantitative extent of the WE. This study is one of the first examples of a targeted agent whose biomarker cannot be defined by genetics, but rather by specific metabolic values.

---

[2] This chapter was adapted and modified from published work: Liberti, M.V., Dai, Z., Wardell, S.E., Baccile, J.A., Liu, X., Gao, X., Baldi, R., Mehrmohamadi, M., Johnson, M.O., Madhukar, N.S. Shestov, A.A., Chio I.I.C, Elemento, O., Rathmell, J.C., Schroeder F.C., McDonnell, D.P., and Locasale, J.W., 2017. A predictive model for selective targeting of the Warburg effect through GAPDH inhibition with a natural product. *Cell Metabolism*, *26*(4), pp.648-659. Author Contributions: Conceptualization, M.V.L. and J.W.L.; Animal experiments, S.E.W., D.P.M., M.V.L., X.G., and R.B.; Koningic acid isolation and purification, M.V.L., J.A.B. and F.C.S.; Metabolomics, M.V.L. and X.L.; Data analysis, M.V.L, M.M., M.O.J., J.C.R., Z.D., N.S.M., O.E., I.I.C.; Mathematical modeling, Z.D., A.A.S.; All other experiments, M.V.L.; Writing, M.V.L. and J.W.L.; Supervision, M.V.L. and J.W.L.

2.2 Abstract

Targeted cancer therapies that use genetics are successful, but principles for selectively targeting tumor metabolism that is also dependent on the environment remain unknown. I now show that differences in rate-controlling enzymes during the Warburg Effect (WE), the most prominent hallmark of cancer cell metabolism, can be used to predict a response to targeting glucose metabolism. I establish a natural product, koningic acid (KA), to be a selective inhibitor of GAPDH, an enzyme we characterize to have differential control properties over metabolism during the WE. With machine learning and integrated pharmacogenomics and metabolomics, my collaborators and I demonstrate that KA efficacy is not determined by the status of individual genes, but by the quantitative extent of the WE leading to a therapeutic window *in vivo*. Thus, the basis of targeting of the WE can be encoded by molecular principles that extend beyond the status of individual genes.

2.3 Introduction

The general approach in cancer research is to define and then exploit the molecular requirements that distinguish tumor from normal. Targeted cancer therapies have used genomic alterations and differences in gene expression as biomarkers to predict therapeutic efficacy with great success. This strategy is currently the major paradigm within the current concept of precision medicine with each one's disease having a specific molecular profile that determines the appropriate course of action (Collins and Varmus, 2015). In contrast, the determinants of therapies that target metabolism for the treatment of complex diseases, such as diabetes, do not depend on the status of a single gene because the principles that determine a specific response to alterations in metabolism are multifaceted convolutions of both genetic and environmental factors (Vander Heiden and DeBerardinis, 2017). Furthermore, predictive models for targeting cancer metabolism have not yet been successfully developed from the mutational or expression status of individual genes (Vander Heiden and DeBerardinis, 2017). Therefore, substantial challenges, especially regarding the appropriate populations that should be investigated, have limited advances in therapies that target cancer metabolism (Garber, 2016).

The most prominent hallmark of cancer metabolism is the Warburg Effect (WE) or aerobic glycolysis, which is defined by the increased uptake of glucose and incomplete oxidation or fermentation to lactate in the presence of oxygen. The WE has been extensively studied over the years and is routinely exploited clinically as a diagnostic of tumor burden with predictive features of cancer outcome (Liberti and Locasale, 2016; Vander Heiden, 2013). There are a number of strategies that have been proposed to target

the WE including targeting oncogenes and tumor suppressor genes that interact with glucose metabolism and the specific isoforms of glycolytic enzymes that are expressed in cancer (Hay, 2016). However, full target inhibition, and thus complete ablation of an enzyme involved in metabolizing glucose, encounters limiting toxicity as glucose metabolism is required in nearly every mammalian tissue. Therefore, partial inhibition of glycolytic enzyme activity with selectivity against tumors is needed. Whether this specificity is possible and the strategy needed to define it is unknown.

An alternative approach to developing a predictive model for targeting cancer metabolism is to exploit differential properties of network activity (e.g. metabolic flux). In this scenario, the glycolytic pathway would be affected by a perturbation to one of its enzymes during conditions that promote the WE and the same perturbation would leave glucose metabolism lesser affected in conditions of normal physiology. This concept of synthetic lethality has been developed in cancer biology by identifying genetic events that create liabilities but a lesser-studied, if not novel approach to identify these vulnerabilities, is to use the quantitative properties encoded in the kinetics and thermodynamics of the metabolic network that are different during the WE. It is known that the level of control that a metabolic enzyme exerts on a metabolic flux depends on properties other than the expression or activity of the given enzyme. Thus, a change in enzyme activity could result in a different effect on metabolic output depending on other properties of the metabolic network. To our knowledge, this concept has not been explored in cancer therapy.

There are generally thought to be three rate-controlling enzymes in glycolysis:

hexokinase, phosphofructokinase, and pyruvate kinase (Lehninger et al., 2013). However metabolic control analysis (MCA) (Fell, 1992), a quantitative approach to evaluate the amount of enzyme activity that is required to alter the overall output of a pathway, has suggested that the rate-control may be different during the WE (Shestov et al., 2014). Furthermore, MCA has proven invaluable in designing and controlling metabolic pathways for biotechnology applications (Bowden, 1999), but has not to our knowledge been explored in biomedical settings. We therefore reasoned that MCA, by identifying differences in biochemical regulation occurring at the systems or network level of the glycolytic pathway (i.e. flux control), could allow for selective targeting of the WE, thus identifying predictors for therapeutic response that are encoded within metabolism. In the present study, we sought to test this hypothesis.

2.4 Results

2.4.1 Thermodynamic and kinetic analysis of rate control in glycolysis

Based on a previously published mathematical model of glycolysis from the lab (Shestov et al., 2014), my collaborator, Ziwei Dai, performed metabolic control analysis (Heinrich and Schuster, 1996) on lactate production flux and evaluated thermodynamics for each step in glycolysis by calculating flux control coefficients (FCCs) and reaction free energies (ΔGs) (Figure 2.1A). While these models have limitations due to our incomplete knowledge of glycolysis, they can allow for discovery with further appropriate validation. Steps with higher FCCs and lower ΔGs are known to exert stronger control over flux through the pathway (Noor et al., 2014). Ziwei also compared

the FCCs of each enzymatic step in glycolysis to their ΔGs (Figure 2.1B). Two of the canonical rate-limiting enzymes of glycolysis, hexokinase (HK) and phosphofructokinase (PFK) exhibited high FCCs and low ΔGs as expected. However, a third glycolytic enzyme, glyceraldehyde-3-phosphate dehydrogenase (GAPDH), also displayed a high FCC and low ΔG, indicating that GAPDH also may be a rate-controlling enzyme of glycolysis in some settings.

To study the relationship between the WE and control of glycolysis, Ziwei also tuned the model to exhibit varying extents of the WE by altering activities of glycolytic enzymes with the highest variation in protein abundance (Figure 2.1C). Although HK, PFK, and GAPDH all exhibit considerable control over flux in glycolysis, only the value of GAPDH FCC increases during the WE (Figure 2.1D). Therefore, inhibiting GAPDH activity exerts a larger reduction in glycolytic flux in cells undergoing a higher degree of the WE than in cells with lower glycolytic activity (Figure 2.1E), thus providing a rationale for exploring the control of glycolytic rate by GAPDH as a target against the WE.

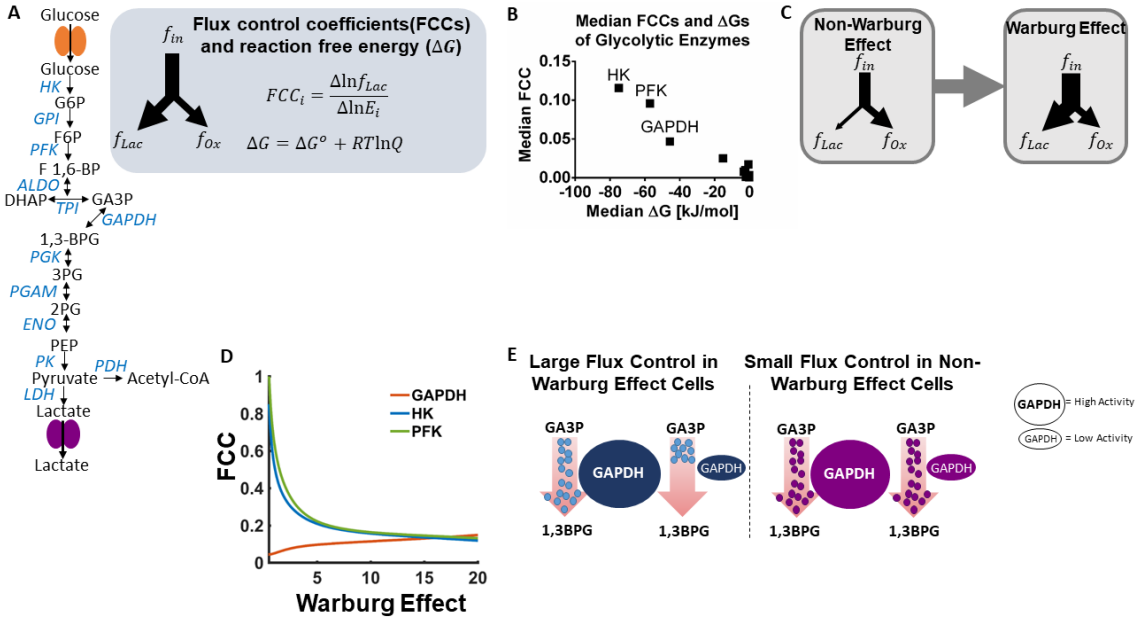

Figure 2.1. Thermodynamic and kinetic analysis of rate-control in glycolysis.
(A) Glycolysis pathway with metabolites (black) and enzymes (blue). Model for flux control coefficients (FCCs) and reaction free energy (ΔG) values. *f*= flux. **(B)** Median FCCs vs. median ΔGs of glycolytic enzymes. HK, hexokinase; PFK, phosphofructokinase; GAPDH, glyceraldehyde-3-phosphate dehydrogenase. **(C)** Schematic showing flux inputs and outputs during Non-Warburg Effect and Warburg Effect conditions. **(D)** Relationship between FCC values of GAPDH, HK, and PFK and extent of the Warburg Effect defined as ratio of lactate production flux to oxidative phosphorylation flux. **(E)** Schematic demonstrating the high rate-limiting effect of GAPDH over cells carrying out the Warburg Effect compared to those undergoing oxidative phosphorylation.
GA3P, glyceraldehyde-3-phosphate; 1,3-BPG, 1,3-bisphosphoglycerate.

2.4.2 Comparative metabolomics nominates a specific GAPDH inhibitor

I next evaluated the cytotoxic activities of several putative GAPDH inhibitors including arsenate, arsenic trioxide, 3-bromopyruvate, iodoacetate, and koningic acid (KA) (Campbell-Burk et al., 1987; Dai et al., 1999; Endo et al., 1985; Ganapathy-Kanniappan et al., 2009; Németi and Gregus, 2005), and found substantial variability (Figures A1.S1A) indicating that they have different pharmacological activities and possibly act by different mechanisms. To further investigate this likely possibility, I generated dose-dependent metabolite profiles in HCT116 cells comprising over 350 metabolites and found that each profile exhibited differences in the levels of glycolytic

metabolites and related pathways (Figures 2.2A-2.2E). However, with the exception of KA, all other profiles exhibited many other perturbations to metabolism as well. I quantified these effects using a network-based pathway analysis (Experimental Procedures) that revealed glycolysis as the highest scoring pathway only in KA-treated cells (Figure 2.2F, 2.2G). Consistent with this finding, I performed a docking analysis which indicates that KA can directly bind to the active site of human GAPDH (Figure 2.2H). Consistently, previous studies have shown that the epoxide moiety of KA alkylates the cysteine residue of the GAPDH catalytic site (Sakai et al., 1988, 1991).

At the concentration corresponding to the IC_{50} value of KA (Figure A1.S1A), GAPDH activity decreased compared to vehicle (Figure A1.S1B). To examine how KA-induced decreases in GAPDH activity exert cytotoxic effects, I evaluated the response at the IC_{50} using a volcano plot (Figure A1.S1C) and confirmed that glycolytic metabolites were predominantly affected with an accumulation of glycolytic intermediates upstream of GAPDH occurring in a dose-dependent manner (Figure A1.S1D). To analyze the consequences of glucose metabolism imbalance, I considered a kinetic flux profiling experiment (Experimental Procedures) using uniformly labeled (U-^{13}C)-glucose in HCT116 cells treated at the IC_{50} over 4 hours. As expected, a reduction of ^{13}C-lactate in KA treated cells was observed, indicating decreased flux through the glycolytic pathway (Figure A1.S1E). Relative levels of pentose phosphate pathway metabolites increased in the presence of KA and flux was disrupted (Figures A1.S1F, A1.S1G), as was flux into glycerol metabolism (Figure A1.S1H). In addition, KA also reduces fluxes in pathways branching from glycolysis downstream of the GAPDH step, including de novo serine

(Figure A1.S1I), entry into the tricarboxylic acid cycle (Figures A1.S1J), and palmitate, the product of *de novo* lipogenesis (Figure A1.S1K). Dose-dependent changes in energy status (Figures A1.S1L-A1.S1N) and redox status (Figure A1.S1O-A1.S1T), both essential functions of glucose metabolism, were also affected. Together these findings indicate that KA induces global alterations in the metabolic network most consistent with direct targeting of GAPDH with a reduction in glycolytic rate and cytotoxicity likely due to the simultaneous effects on numerous metabolic pathways and functions.

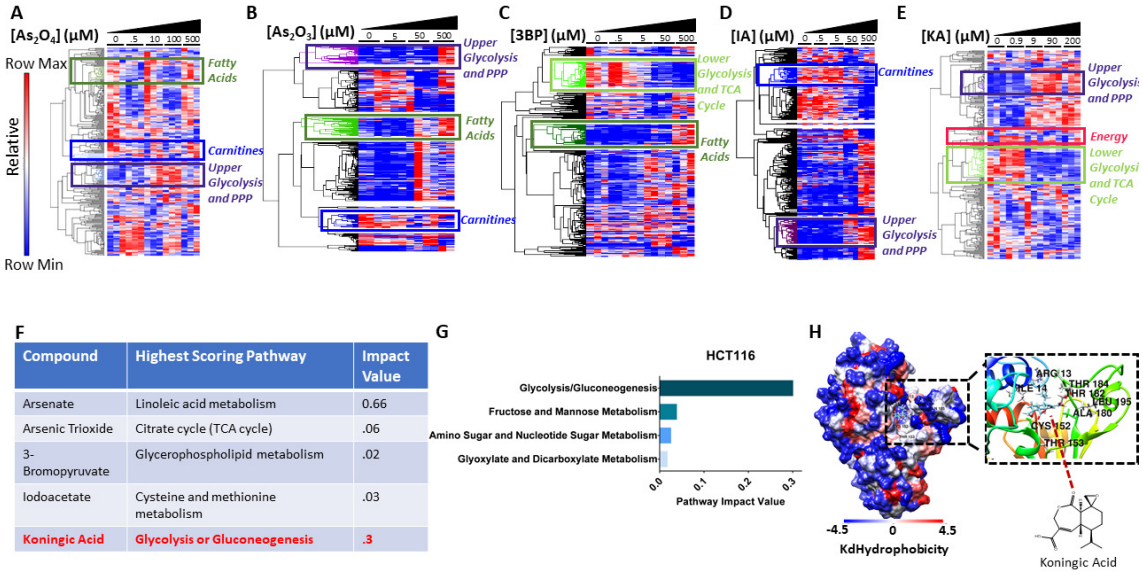

Compound	Highest Scoring Pathway	Impact Value
Arsenate	Linoleic acid metabolism	0.66
Arsenic Trioxide	Citrate cycle (TCA cycle)	.06
3-Bromopyruvate	Glycerophospholipid metabolism	.02
Iodoacetate	Cysteine and methionine metabolism	.03
Koningic Acid	**Glycolysis or Gluconeogenesis**	**.3**

Figure 2.2. Comparative metabolomics nominates a specific GAPDH inhibitor.
(A-E) Clustered heatmaps with pathway and dose annotations of dose-dependent global metabolic responses to putative GAPDH inhibitors. **(A)** Arsenate (As_2O_4). **(B)** Arsenic trioxide (As_2O_3). **(C)** 3-bromopyruvate (3BP). **(D)** Iodoacetate (IA). **(E)** Koningic acid (KA). **(F)** Network-based pathway analysis for each compound. **(G)** Pathway analysis showing top 4 highest scoring pathways in response to KA. **(H)** KA docking analysis to GAPDH active site Cys152.

2.4.3 Expression of a fungal-derived KA-resistant *GAPDH* allele renders human cells completely resistant to KA and reverses their metabolic profile

Notably, the cytotoxic effects of targeting metabolism can often be rescued by supplementation of nutrients that restore the defective metabolic functions, as is the case

of metformin and mitochondrial metabolism (Liu et al., 2016). I thus attempted to restore cell viability by modulating nutrient availability but was unable to rescue cytotoxicity induced by KA (Figures A1.S2A-S2E). To determine whether other mechanisms and thus possible off-target effects may account for KA cytotoxicity, I considered alternative approaches to determine whether GAPDH is the mechanistic target of KA. Notably, KA is a natural product obtained from the *Trichoderma* fungus, which thrives in anaerobic environments rich in sugar. When encountering microbes that compete for its carbon source, it secretes KA as an antibiotic to eliminate these organisms (Sakai et al., 1990; Watanabe et al., 1993), while expressing a resistant allele of GAPDH (*T. koningii* KAr-GAPDH) (Figure 2.3A). Thus, I cloned the *T. koningii* KAr-GAPDH and expressed it in human HEK293T and HCT116 cells. After verifying that human cells can express *T. koningii* KAr-GAPDH (Figure 2.3B, A1.S2F), I observed that HEK293T cells expressing *T. koningii* KAr-GAPDH exhibited complete cell viability (Figure 2.3C) and HCT116 cells expressing *T. koningii* KAr-GAPDH exhibited almost complete viability (Figure A1.S2G) after treatment with 0-200μM KA. These results further demonstrated the specificity of KA towards GAPDH. In addition, while *T. koningii* KAr-GAPDH displays similarity to the active site of GAPDH with conservation of the reactive cysteine, it exhibits evolutionary divergence (Figures A1.S2H-A1.S2J) from mammalian GAPDH suggesting that acquiring resistance by mutating individual GAPDH residues is difficult.

Since expression of *T. koningii* KAr-GAPDH successfully rescued cell viability in human cells treated with KA, I considered whether changes in metabolism observed in human cells treated with KA can be reversed upon KAr-GAPDH expression. After KA

treatment, marked differences in metabolism in empty vector (EV) expressing cells were observed that were completely absent in *T. koningii* KAr-GAPDH-expressing cells (Figures 2.3D, A1.S2K-A1.S2L) and manifested in differential changes in the levels of glycolytic intermediates (Figure 2.3E, A1.S2M), PPP (Figure 2.3F), and the TCA cycle (Figure 2.3G, A1.S2N). Together, these data confirm that the mechanistic target of KA is indeed GAPDH in part by establishing that all disruptions to metabolism are ablated when cells are engineered to be resistant to KA by expressing a resistant allele of GAPDH.

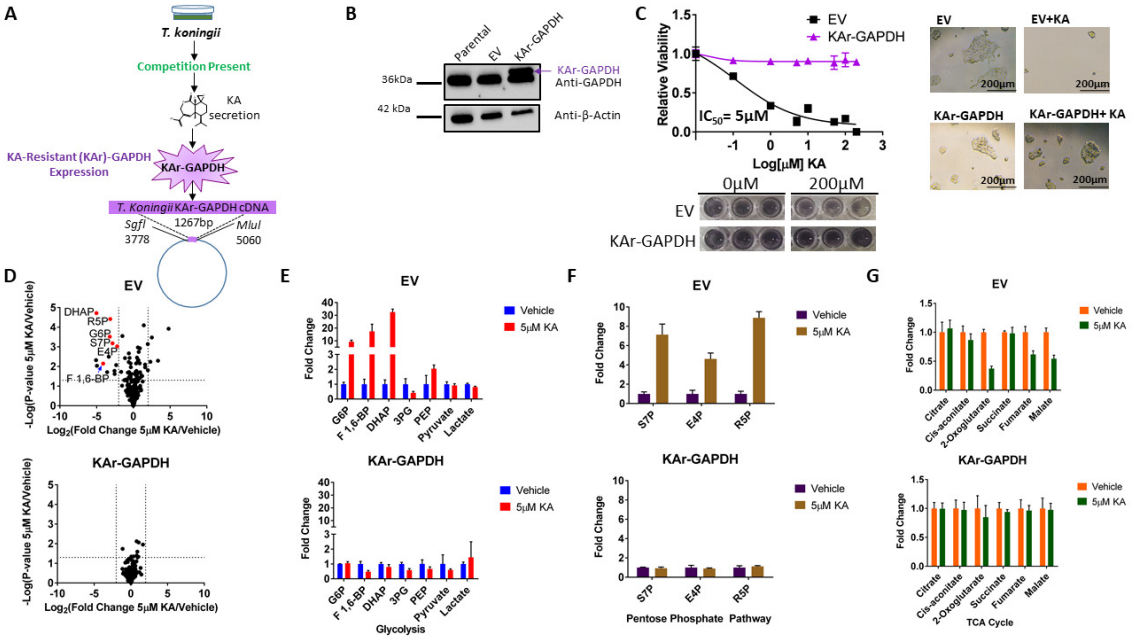

Figure 2.3. Expression of a fungal-derived KA-resistant GAPDH allele renders human cells completely resistant to KA and reverses their metabolic profile.
(A) Schematic showing expression of a resistant allele of GAPDH by *Trichoderma virens.* **(B)** Immunoblotting of parental, EV or KAr-GAPDH expressing HEK293T cells. **(C)** Cell viability of HEK293T cells expressing KAr-GAPDH or EV (top left). Representative images of well (bottom left, top right) KAr-GAPDH or EV expressing cells treated with vehicle (0μM) or KA (200μM). **(D)** Volcano plots showing metabolite profiles of HEK293T cells expressing EV compared to those expressing KAr-GAPDH after treatment with DMSO or 5μM KA. Log_2 fold change versus $–log_{10}$ (p-value). Dotted lines along x-axis represent $±log_2(2)$ fold change and dotted line along y-axis represents $–log_{10}(0.05)$. Glycolysis metabolites shown as red points. All other metabolites are black points. **(E)** Glycolytic metabolite levels. **(F)** Pentose Phosphate Pathway levels. **(G)** TCA cycle metabolite levels.
G6P, Glucose-6-Phoshate; F 1,6-BP, Fructose 1,6-Bisphosphate; DHAP, Dihydroxyacetone Phosphate; 3PG, 3-Phosphoglycerate; PEP, Phosphoenolpyruvate; S7P, Sedoheptulose-7-Phosphate; E4P, Erythrose-4-Phosphate; R5P, Ribose-5-Phosphate.
All data are represented as mean ±SEM from n = 3 biological replicates unless otherwise noted.

2.4.4 The cytotoxic response to KA treatment is heterogeneous

In collaboration with the National Cancer Institute (NCI), we next measured the response to KA across a collection of 60 cancer cell lines from diverse tissue and genetic origins. At 10μM, there was a broad, but heterogeneous response to KA (Figure 2.4A) consistent with measured values of the IC_{50} for each line (Figure A1.S3A). Consistent with earlier findings, HCT116 cells were only moderately sensitive to KA, therefore requiring a higher concentration of KA to trigger a disruption in the metabolic network. I identified three of the most resistant cell lines to KA as MCF-7, UACC-257, and NCI-H226 and their corresponding sensitive cell lines to KA as BT-549, SK-MEL-28, and NCI-H522 based on matching tissue type and subjected them to further analysis. Analysis of the cell lines considered showed that no single tissue type was more sensitive or resistant to KA (Figures A1.S3B-A1.S3D). I assessed whether inhibition of GAPDH activity accounts for the variability in cell line responses and found that GAPDH activity in response to KA treatment revealed little differences in the change in enzyme activity across both sensitive and resistant cells given KA at the same dose (Figures 2.4B, 2.4C). Thus, resistance to KA does not occur due to the inability to effectively inhibit GAPDH, rather it appears to occur by another mode of action.

To determine whether nutrient supplementation could rescue cell viability in sensitive cells, I added serine and lactate, pyruvate, lactate, or 3PG to cells upon KA treatment (Figure A1.S3E). Consistent with the findings in HCT116 cells (Figure A1.S2E), nutrient supplementation was unable to rescue cell cytotoxicity. To determine whether differences in how KA affects metabolism contributes to the response, I

generated metabolite profiles and found that sensitive cell lines revealed signatures nearly identical to those observed in previously characterized cell lines (Figures 2.2-2.3) whereas resistant cell lines did not show any significant metabolite alterations (Figures 2.4D-2.4F) as was also observed with kinetic flux profiling completed by Ziwei Dai and me (Figures 2.4G-2.4H, A1.S3F-A1.S3H). Consistently, an accumulation of upper glycolytic intermediates and altered flux was observed only in sensitive cells (Figure 2.4I, A1.S3I). Branching pathways were also affected whereby glucose flux decreased through TCA cycle intermediates and serine in a representative sensitive cell line (Figures A1.S3J-A1.S3M). Not surprisingly, overall TCA cycle metabolite levels remained unchanged, likely attributed to non-glucose carbon sources fueling the TCA cycle (Figure A1.S3N). The metabolic changes observed in sensitive cells was confirmed using a pathway analysis and hierarchal clustering (Figures A1.S4A-A1.S4D). All together, these data strongly suggest that the heterogeneous response to KA observed across 60 cell lines can be attributed to the specific control that GAPDH exerts over the glycolytic pathway in certain cells, independent of the extent of enzyme inhibition and tissue type.

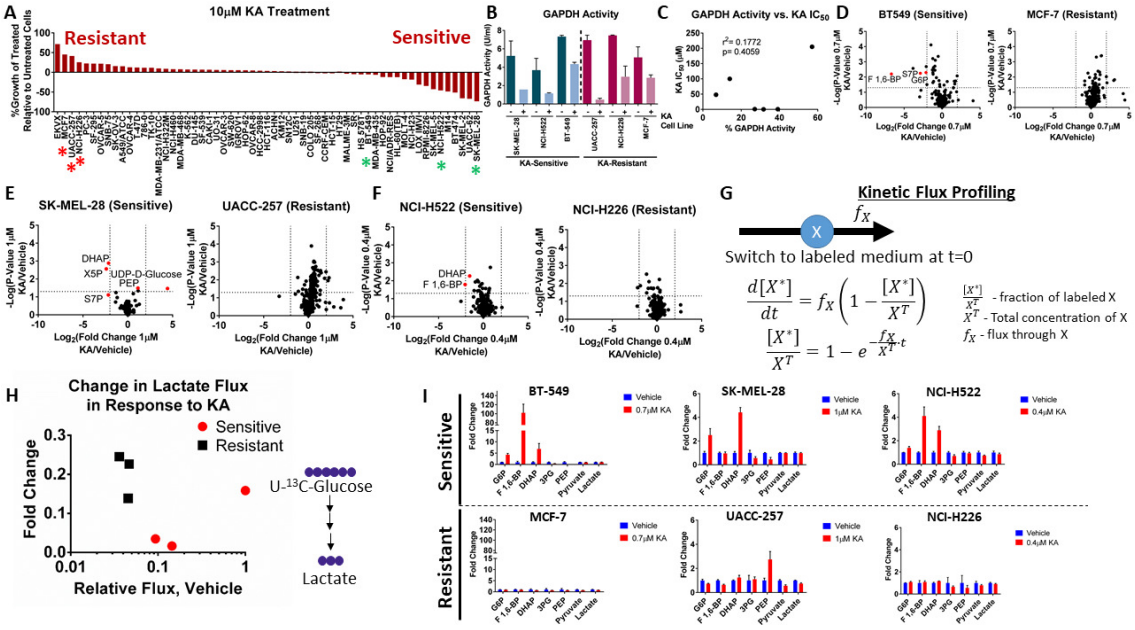

Figure 2.4. The cytotoxic response to KA treatment is heterogeneous.
(A) Waterfall plot showing the difference in response of KA to 60 independent cell lines treated with vehicle (0.01% DMSO) or 10μM KA. Representative KA-resistant cell lines (Red, *) and KA-sensitive cell lines (Green, *). **(B)** Relative GAPDH activity in representative KA-sensitive and resistant cell lines in response to vehicle (DMSO) or KA. SK-MEL-28 and UACC-257 were treated with vehicle or 1μM KA; NCI-H522 and NCI-H226 were treated with vehicle or 0.4μM KA; BT-549 and MCF-7 were treated with 0.7μM KA (n=2). **(C)** Pearson correlation of KA IC_{50} values for KA-sensitive and resistant cell lines versus percent of GAPDH activity. **(D)** Volcano plots showing metabolite profiles of breast cancer cell lines after treatment with DMSO or 90μM KA. Log_2 fold change versus $-log_{10}$ (p-value). Dotted lines along x-axis represent $\pm log_2(2)$ fold change and dotted line along y-axis represents $-log_{10}(0.05)$. Glycolysis metabolites shown as red points. All other metabolites are black points. **(E)** Melanoma cell lines as in (D). **(F)** Non-small cell lung cancer cell lines as in (D). **(G)** Kinetic flux profiling for lactate labeling from ^{13}C-glucose. **(H)** Change in lactate flux in response to KA based on fold changes vs. relative fluxes of the vehicle group from ^{13}C-lactate enrichment from U-^{13}C-glucose. **(I)** Glycolysis profiles for KA-sensitive and resistant breast, melanoma, and NSCLC cell lines treated with vehicle or their respective KA IC_{50} concentrations.
S7P, sedoheptulose-7-phosphate; F 1,6-BP, fructose 1,6-bisphosphate; G6P, glucose-6-phosphate; DHAP, dihydroxyacetone phosphate; X5P, xylulose-5-phosphate; PEP, phosphoenolpyruvate; UDP-D-glucose, uridine diphosphate-D-glucose.
All data are represented as mean ±SEM from n = 3 biological replicates unless otherwise noted.

2.4.5 A multi-omics analysis reveals that only the extent of the WE predicts KA response

We next sought to determine if any molecular features predict KA sensitivity or response. My collaborators Mahya Mehrmohamadi, Neel Madhukar, and I correlated KA IC_{50} values with multiple layers of physical and molecular information including cell size, doubling time, genetic status, mRNA expression, protein expression, and metabolic

uptake and excretion rates that are available in 59 of the 60 cell lines (Dolfi et al., 2013; Jain et al., 2012) (Figure 2.5A). I determined that neither cell size nor doubling time correlated with response to KA (Figures 2.5B-2.5C) nor did mutational status of several commonly mutated oncogenes and tumor suppressor genes including *KRAS, PIK3CA, MYC, and TP53* (Figure A1.S5A). Mahya determined that neither gene set enrichment analysis (GSEA) nor glycolytic enzyme expression reveal any significant association of any known gene sets to KA response (Figures 2.5D-2.5E, A1.S5B) as was also observed when Neel analyzed relationships with protein expression (Figures 2.5F, 2.5G). Strikingly, I determined that a comparison of metabolic uptake and excretion rates (Figure 2.5H) showed that glucose uptake (Spearman correlation, $r = 0.60$, $p = 9.4 \times 10^{-7}$) (Figure 2.5I) and lactate excretion (Spearman correlation, $r = 0.60$, $p = 5.6 \times 10^{-7}$) (Figure 2.5J), two parameters that quantitatively define the WE, had the highest Spearman correlation coefficients and were predictive of KA response. Moreover, my collaborator Ziwei Dai found that metabolic fluxes are significantly more correlated to KA IC_{50} values than to the random distribution (Figure 2.5K), which is not the case for mRNA and protein which appear random (Figures 2.5D, 2.5F). Therefore, of the roughly 50,000 molecular and physical variables surveyed, only glucose uptake and lactate excretion (i.e. the WE) were predictive of KA response allowing us to conclude that KA, and thus partial inhibition of GAPDH, specifically targets the WE.

To address the diagnostic performance of glucose uptake and lactate secretion flux as predictive measurements of KA sensitivity, we generated receiver-operating characteristic (ROC) curves and calculated the area under the curve (AUC) (Figure 2.5L).

Notably, we found that both glucose and lactate flux are strong predictors of KA response with an AUC=0.81, with prediction accuracy comparable to six representative targeted cancer therapies with known biomarkers. These data strongly support the clinical applicability and feasibility of using glycolytic flux, which is readily measured clinically with imaging, as predictors of KA efficacy.

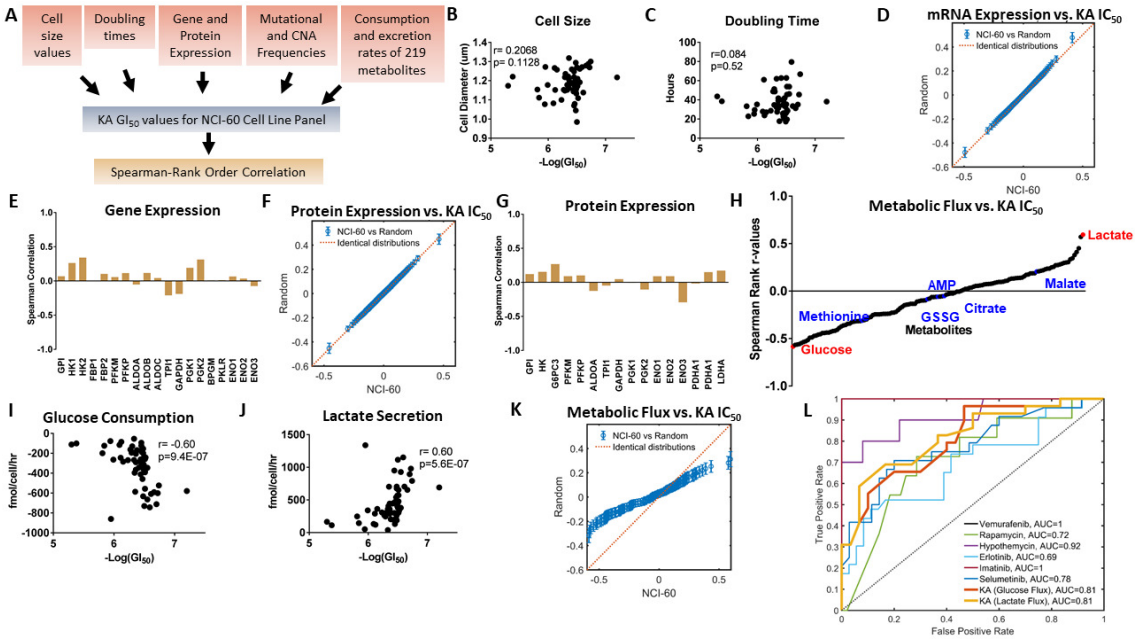

Figure 2.5. A multi-omics analysis reveals that only the extent of the WE predicts KA response.
(A) Schematic workflow of spearman rank correlation calculations from metabolite consumption and excretion rates, cell size, doubling time, mutation and copy number alteration (CNA) frequencies, and gene and protein expression patterns with KA IC_{50} response across NCI-60 cell line collection. **(B)** Cell size correlation with KA IC_{50} response across NCI-60 cell line panel. **(C)** Doubling time correlation as in (B). **(D)** Quantile-Quantile (Q-Q) plot comparing the quantiles from the correlation between mRNA expression levels and KA IC_{50} values in NCI-60 cell line screen with random values. **(E)** Glycolysis gene expression correlation as in (B). **(F)** Q-Q plot for protein expression levels as in (D). **(G)** Glycolysis protein expression correlation as in (B). **(H)** Correlations of uptake and secretion rates of metabolites. **(I)** Glucose uptake correlation as in (B). **(J)** Lactate secretion correlation as in (B). **(K)** Q-Q plot for metabolic flux as in (D). **(L)** Receiver-operating characteristic (ROC) curves of standard cancer therapies with specific targets and/or biomarkers. Area under the curve (AUC) assesses biomarker accuracy.

2.4.6 KA is bioavailable and induces dynamic changes to glycolysis *in vivo*

Thus far, we have established that in culture, the WE can be selectively targeted by exploiting metabolic control analysis and flux control through GAPDH. However, the

effects on normal cells and whether a therapeutic window can be achieved *in vivo* are unclear. To begin to address these remaining questions, my collaborator Marc Johnson first evaluated the effects of GAPDH inhibition in CD8+ cells since these cells are important in immune therapy settings. He found that KA does not have significant effects on proliferation, viability, or activation markers in activated CD8+ cells at lower concentrations (Figures A1.S6A-A1.S6I). I next evaluated the sensitivity of the highly glycolytic (Timmerman et al., 2013) estrogen-responsive breast cancer cell line, BT-474 to KA (IC_{50} =1μM) (Figure A1.S6J). At KA concentrations corresponding to the IC_{50}, GAPDH activity was reduced and glycolysis was altered (Figures A1.S6K-A1.S6M). Next, my collaborators Suzanne Wardell, Xia Gao, and I ovariectomized *nu/nu* mice which were then implanted subcutaneously with a slow-releasing 17β-estradiol pellet and BT-474 cells were injected orthotopically into the mammary fat pad (Experimental Procedures). Tumors were established prior to toxicology studies (Figure 2.6A). 1 mg/kg KA was determined to be the maximum tolerated dose (MTD) based upon behavioral monitoring and adverse events that I observed at higher doses (hemolysis, hematuria, and anemia) (Figure 2.6B). To determine whether KA induces changes in glycolysis, I sacrificed mice over a time course of up to 24 hours and used metabolite profiling to examine the levels of glycolytic intermediates in upper glycolysis at different endpoints. Strikingly, fructose 1,6-bisphosphate (F1,6-BP) accumulated in tumors between 8-16 hours of treatment with 1 mg/kg KA, as did dihydroxyacetone phosphate (DHAP), albeit to a lesser extent (Figure 2.6C). Relative levels of 3-phosphoglycerate (3PG) and phosphoenolpyruvate (PEP), showed a decrease after 5-10 minutes of KA treatment, and

recovered thereafter (Figure 2.6D). After 16 hours, upper glycolytic and PPP metabolites had the largest fold change increase (Figure 2.6E). At 10 minutes, PEP was significantly lower compared to all other detected metabolites, while 3PG had a similar trend (Figure 2.6F). These results indicate a dynamic effect on glycolysis whereby upper glycolytic metabolites accumulate within hours of KA treatment and lower glycolytic intermediates deplete within minutes, but then recover, likely due to a contribution of non-glucose carbon sources (Figure 2.6G). These data confirm that KA is bioavailable, tolerable at certain doses, and induces acute and dynamic changes in the glycolytic network in tumors.

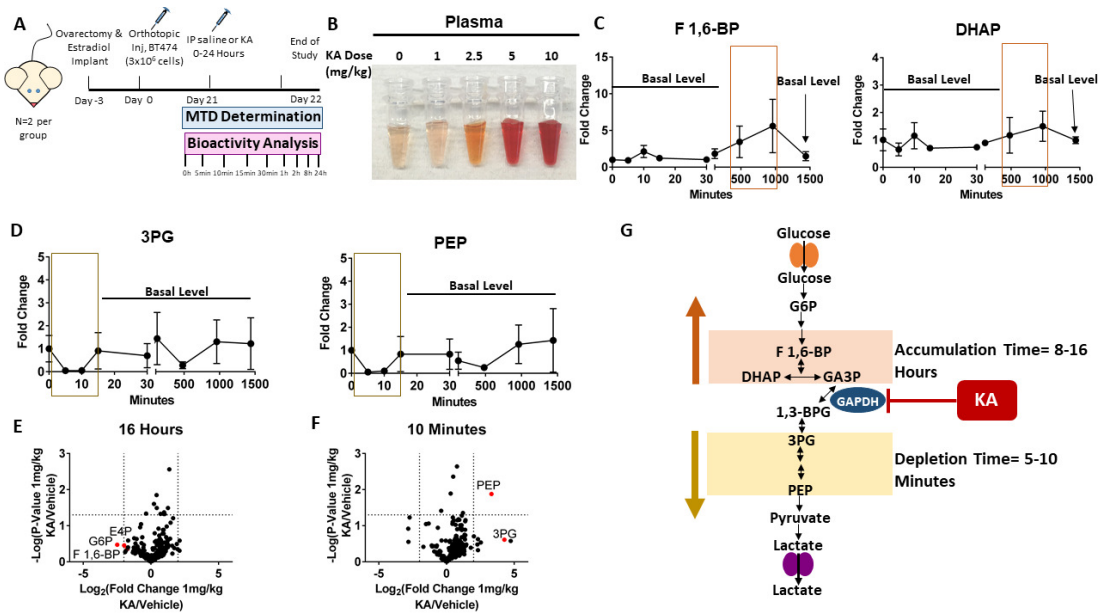

Figure 2.6. KA is bioavailable and induces dynamic changes in glycolysis *in vivo*.
(A) Schematic of timeline and treatment regimen of E2 treated female *nu/nu* mice injected with BT-474 cells orthotopically. These mice were treated with either saline or 1mg/kg, 2.5mg/kg, 5mg/kg, or 10mg/kg to identify the maximum tolerated dose (MTD) for 24 hours. **(B)** Plasma from MTD analysis for doses of 0-10mg/kg KA. **(C)** Levels of upper glycolytic intermediates from 0-24 hours (n=2 per group). **(D)** Levels of lower glycolytic intermediates as in (C). **(E)** Volcano plot showing metabolic profile at 16-hour time-point. Log_2 fold change versus $-log_{10}$ (p-value). Dotted lines along x-axis represent $\pm log_2(2)$ fold change and dotted line along y-axis represents $-log_{10}(0.05)$. Glycolysis and related metabolites shown as red points. All other metabolites are black points (n=2). **(F)** 10-minute time-point as in (E). **(G)** Schematic showing the dynamic response KA treatment.
G6P, glucose-6-phosphate; F 1,6-BP, fructose 1,6-bisphosphate; DHAP, dihydroxyacetone phosphate; GA3P, glyceraldehyde-3-phosphate; 1,3-BPG, 1,3-bisphosphoglycerate; 3PG, 3-phosphoglycerate; PEP, phosphoenolpyruvate.
All data are represented as mean ±SEM from biological replicates.

2.4.7 A therapeutic window for precise targeting of the WE with KA can be achieved *in vivo*

Given the bioavailability and tolerability of KA, I identified a resistant cell line to KA, MDA-MB-231 (Figures A1.S6N-A1.S6O) and carried out metabolite profiling in the presence of KA, in which no metabolic changes were observed in response to KA treatment (Figures A1.S6P-A1.S6Q). My collaborator Suzanne Wardell and I next established two orthotopic breast cancer models in which mice were injected with either sensitive BT-474 cells or resistant MDA-MB-231 cells into the mammary fat pad and were treated daily with 1mg/kg KA, monitoring body weight and tumor growth for 14 days (Figure 2.7A). We determined that the circulating plasma concentration was 0.7μM KA (Figure A1.S7A-S7C). No significant changes in body weight were observed in BT-474 tumor bearing mice ($p=0.37$, two-tailed student's t-test) or MDA-MB-231 tumor bearing mice ($p=0.86$, two-tailed student's t-test) indicative of drug tolerability (Figure A1.S7D). Importantly, tumor growth in KA treated BT-474 tumor bearing mice was substantially suppressed ($p<0.0001$, two-way ANOVA) whereas tumor growth in KA treated MDA-MB-231 cells was only marginally suppressed ($p=0.02$, two-way ANOVA) over the course of 2 weeks (Figures 2.7B-2.7D). In addition, tumor morphology was markedly different in KA treated mice and cell proliferation was significantly decreased ($p=4.0 \times 10^{-5}$, unpaired multiple-t-test) (Figures 2.7E, A1.S7E). GAPDH is suspected to have nuclear functions in cells (Barber et al., 2005; Jung et al., 2014), but remained localized to the cytoplasm, indicative of its role in glycolysis as its primary mode of action for tumor suppression upon KA treatment (Figure 2.7E).

Given the efficacy of KA and issues of toxicity that typically limit further clinical evaluation of glycolysis inhibitors (Raez et al., 2013), I examined the effects on metabolism in healthy tissue. Metabolomics in skeletal muscle showed no differences upon KA treatment (Figures 2.7F, A1.S7F). Metabolomics on whole blood showed as expected, altered glycolysis (Figure A1.S7G), but no substantial differences in complete blood count (CBC) in BT-474 tumor bearing mice ($p=0.08$, two-tailed student's t-test) or in MDA-MB-231 tumor bearing mice ($p=0.41$, two-tailed student's t-test) (Figure 2.7G and A1.S7H). Creatinine ($p=0.35$, two-tailed student's t-test) (Figure 2.7H), bilirubin ($p=0.34$, two-tailed student's t-test) (Figure 2.7I), and alanine aminotransferase (ALT) activity ($p=0.95$, two-way ANOVA) (Figure 2.7J), markers of renal and hepatic toxicity, showed no differences. Energy charges (ATP/ADP) in BT-474 tumor, skeletal muscle, blood, and liver, also showed no significant changes (Figures A1.S7I-A1.S7L). Similarly, oxidized to reduced glutathione ratios were not altered (Figure A1.S7M). While no changes were observed in energy metabolites in tumors, it is possible that non-glucose courses are compensating for glycolysis inhibition at longer times given changes in energy metabolites in cell culture (Figure A1.S1L-A1.S1T). Lastly, I determined the levels of pyruvate and lactate from multiple tissues as a readout of gluconeogenesis. I found that in KA-treated BT-474 tumor bearing mice, pyruvate and lactate were elevated in tumors (Figure A1.S7N), but remained mostly unchanged in liver, plasma, and muscle (Figures A1.S7O-A1.S7Q). These data show that KA exerts bioactivity mainly in the tumors as shown by acute changes in glycolysis, while sparing normal tissues as indicated

by its tolerability without exerting toxic effects in mice.

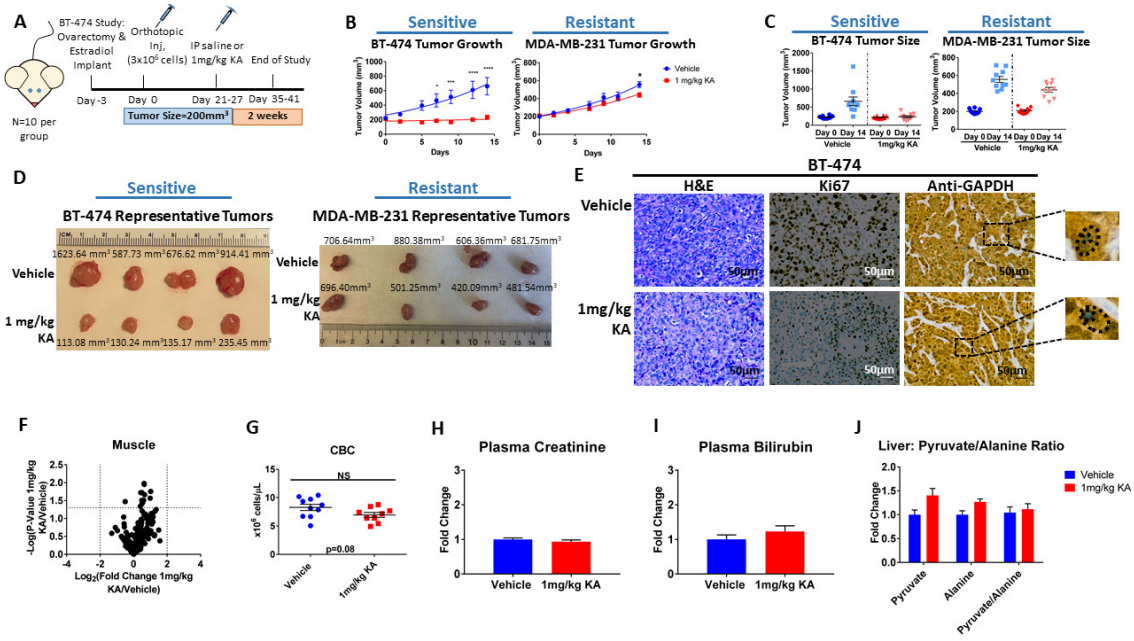

Figure 2.7. A therapeutic window for precise targeting of the WE with KA can be achieved *in vivo*.
(A) Schematic of timeline and treatment of E2 treated female *nu/nu* mice injected with KA-sensitive BT-474 cells and female *nu/nu* mice injected with KA-resistant MDA-MB-231 cells orthotopically and treated with either saline or 1mg/kg KA. **(B)** Average tumor volume (mm^3) over 14 days in mice injected with BT-474 or MDA-MB-231 cells treated with vehicle or 1mg/kg KA (n=10 per group). **(C)** Tumor volume of each individual mouse from day 0 and day 14 in the BT-474 and MDA-MB-231 tumor models (n=10). **(D)** Representative BT-474 and MDA-MB-231 tumors from vehicle treated and 1mg/kg KA treated E2 treated female *nu/nu* mice on day 14. **(E)** Representative hematoxylin and eosin (H&E) and immunohistochemical (IHC) staining of serial sections from *nu/nu* mice injected with BT-474 cells treated with vehicle or 1mg/kg KA. **(F)** Volcano plot showing metabolic profile from skeletal muscle treated with vehicle or 1mg/kg KA from BT-474 tumor model. Log_2 fold change versus $-log_{10}$ (p-value). Dotted lines along x-axis represent $\pm log_2(2)$ fold change and dotted line along y-axis represents $-log_{10}(0.05)$. Significantly different metabolites shown as red points. All other metabolites are black points (n=3). **(G)** Complete blood count (CBC) for BT-474 mice treated with vehicle or 1mg/kg KA after 14 days (n=9 for vehicle group; n=10 for treatment group). **(H)** Relative levels of creatinine from plasma (n=10 per group). **(I)** Relative levels of bilirubin from plasma (n=10 per group). **(J)** Pyruvate, alanine, and pyruvate to alanine ratio in liver (n=10 per group).
Data are represented as mean ±SEM, biological replicates.
*p<0.05, **p<0.01, ***p<0.001, ****p<0.0001 as determined by two-way ANOVA.

2.5 Discussion

There have been numerous efforts to target what have been considered to be rate-limiting steps in glycolysis (Galluzzi et al., 2013; Hay, 2016; Vander Heiden, 2013). Most notably PKM2, an isoform of pyruvate kinase, has been proposed to be limiting for the WE and has been the focus of many drug development efforts. However, targeting it

successfully has been challenging with numerous conflicting findings (Israelsen et al., 2013). My results suggest that GAPDH appears to be the step in glycolysis whose regulatory properties are most different during the WE. I was able to demonstrate a remarkable selectivity towards the WE by targeting GAPDH with KA as was concluded by evaluating the determinants of its efficacy in over sixty cell lines and *in vivo*. Notably, this selectivity to KA treatment was manifested across the diverse cell and tissue types of an entire mammal. Importantly, despite glycolysis being required for nearly every cell in the animal, little to no whole-body metabolic changes were observed at efficacious doses. Thus, partial inhibition of GAPDH while exhibiting selective toxicity in tumors could be tolerated in most healthy cells.

I also determined that this compound, KA, is a candidate for further pre-clinical analysis since its cytotoxicity appears to occur specifically by acting on GAPDH. I found that, when KA is effective, it exerts numerous simultaneous metabolic disturbances across many pathways that are each individually considered to be targets in cancer (Locasale, 2013; Svensson et al., 2016; Weinberg and Chandel, 2015), which may be attractive for therapy.

Other successful cancer therapeutics such as rapamycin have been isolated originally as natural products for their antibiotic activity (Vezina et al., 1975). Rapamycin was later shown to have rich underlying biology after identifying its mechanistic target, TOR. My study provides another example of a natural product with antibiotic activity and rich underlying mammalian biology (Liberti and Locasale, 2016) as its mechanistic target (i.e. the WE). It is likely that in addition to KA being an agent with possible therapeutic

value, KA will serve as a probe to more specifically explore the WE and delineate its physiological and pathophysiological functions.

Metabolic control analysis and principles for targeting cancer metabolism

These findings illustrate how specific control of metabolic flux by an enzyme in a defined metabolic state can be exploited for selective targeting of that metabolic status. While metabolic control analysis (MCA) is widely used in broad applications such as the metabolic engineering of biofuels or antibiotic production in microbes (Bowden, 1999), our studies show that these concepts can be more broadly applicable to address biomedical questions. It should be noted that there are caveats to using MCA in that it depends on the selection and analysis of parameters and the boundary of the specific metabolic network model, and other assumptions. In addition, the assumption that the metabolic system is in steady-state only partially resembles a real system. Nonetheless, we were able to show that MCA could reveal network properties of glucose metabolism specific to the WE. Importantly, we were able to use MCA to define pharmacological interventions that specifically disrupt metabolic pathways important in neoplastic settings but render healthy tissue largely unaffected. This concept was developed by first demonstrating that during the WE, a hallmark of cancer metabolism, the rate-controlling steps in glycolysis are different than in fully oxidative energy metabolism. In this case, the effect of a change in GAPDH activity is amplified under WE conditions as reflected by the drastic changes in glycolytic flux in KA-sensitive cells, but not KA-resistant cells (despite similar degrees of GAPDH inhibition). This differential notably is a systems level property of how the metabolic network is configured and is independent of the

specific behavior of any particular enzyme outside of the context of how the flux through the metabolic network is configured.

Altogether my study consists of a wealth of metabolomics data with over 500 metabolite profiles generated throughout the course of this study. Although many of these compounds are commonly used as GAPDH inhibitors in the literature, I found that their metabolome-wide responses were markedly different. Using a global metabolite profile as a handle on cellular physiology, these differences in responses could be assessed and used for subsequent molecular characterization as when we expressed a resistant allele of GAPDH from *Trichoderma virens* in human cells. Given the advent of this technology, I am hopeful that this resource and framework will allow for similar in-depth characterization when evaluating other pharmacological or genetic perturbations to metabolism. Such resources comparable in scope have been documented for yeast as in a recent study that evaluated the amino acid profiles of a yeast deletion library (Mulleder et al., 2016). This current analysis enables characterization of a phenotypic response in mammalian systems.

Therapeutic applications to cancer metabolism have often been limited by defining the appropriate contexts in which a given agent may be effective. Unlike cases where genetic status determines the success or failure of a given therapy, therapies that affect metabolism may have more complicated biomarkers, if any. In fact, recent studies have suggested that environmental factors such as tissue type or nutritional status have a larger influence on cancer cell metabolism (Davidson et al., 2016; Hensley et al., 2016; Mayers et al., 2016; Yuneva et al., 2012) than the genetic lesions that have been thought

to determine the extent of the WE (Vander Heiden et al., 2009). Therefore, the metabolic state of the tumor is a complex function of genetic, protein and environmental status. Consistent with these findings, I remarkably found that of over 50,000 variables surveyed including the mutational status of oncogenes that are known to influence the WE, only a specific configuration of metabolism involving the extent of glucose uptake and lactate secretion was predictive of the outcome of a treatment with an agent that targets a glycolytic enzyme. Thus, my study provides one of the first examples of a targeted agent whose biomarker cannot be defined by genetic status, but by the value of a specific metabolic flux. Since metabolite measurements are routinely used clinically as diagnostics and FDG-PET uptake, which is a surrogate for glycolytic rate, as a standard approach to monitor tumor progression, my findings could be straightforwardly employed in the clinic. Importantly, my study demonstrates that a complete understanding of pharmacogenomics (Iorio et al., 2016) that uses multi-omics data to predict drug responses also likely requires information encoded at the level of metabolites and metabolic fluxes.

2.6 Experimental Procedures

2.6.1 Cell culture

All cells were cultured in full media containing RPMI-1640 (Gibco), 10% heat-inactivated fetal bovine serum (FBS), 100U/mL penicillin, and 100mg/ml streptomycin. All cell lines were obtained from the American Tissue Culture Collection (ATCC), except UACC-57, which was obtained from the National Cancer Institute (NCI) at the National

Institutes of Health (Bethesda, MD, USA). Cells were cultured in a 37˚C, 5% CO_2 atmosphere. For koningic acid (KA) dose response curves, either KA (Adipogen, #AG-N2-0118-M001; Isolated In-House) solubilized in water was added to the media at the respective concentrations or 0.01% water for the vehicle. At the start of each experiment, cells were seeded at a density of $1x10^6$ cells for 10cm plates for protein collection, $3x10^5$ cells/well in a 6-well plate for metabolite collection, and $5x10^3$ cells/well in a 96-well plate for cell viability and activity assays. Cells were allowed to adhere for 24 hours.

2.6.2 CD8 activation

CD8+ cells were isolated from the spleens of 8-12-week-old C57BL/6J mice (The Jackson Laboratory, 000664) fed standard chow maintained under IACUC approved protocols. CD8+ cells isolated to greater than 95% purity by CD8+ negative isolation kit (Miltenyi, #130-095-236). CD8+ cells were stained using the proliferative dye Cell Trace Violet (LifeTech, #C34557) before stimulation as per manufacturer's protocol. Cells were stimulated on 5 μg/mL anti-CD3/CD28-coated plates (ebioscience, aCD3 #16-0031-85; aCD28 #16-0281-85) in RPMI 1640 media containing IL-2 ('activated', ebioscience, #14-8021-64, 10 ng/mL), or in tissue-culture treated plates in media containing IL-7 ('naive', Peprotech, #217-17), 1 ng/mL) for up to 7 days. Drug was added at the beginning of activation. Cells were removed at each day described for viability (Propidium Iodide, Sigma-Aldrich, #P4864), cell counts, proliferation, and/or surface markers of activation. Cell surface markers used were CD8-APC (ebioscience, #17-0081-82), CD62L-APC (ebioscience, #17-0621-82), CD44-PE (ebioscience, #12-0441-82), and CD62L-FITC (ebioscience, #11-0621-81). At day 4 and 7, cells were removed for intracellular

granzyme B PE stain (ebioscience, #12-8898-80). All data were acquired in triplicate on a MacsQuant Analyzer (Miltenyi Biotec) and analyzed using FlowJo V10 (TreeStar software).

2.6.3 Drug treatments

For all cell lines, IC_{50} values were measured by seeding $5x10^3$ cells/well in triplicate in a 96-well plate and allowed to adhere for 24 hours. The following day, 0-500μM concentrations of either vehicle (DMSO), arsenate (As_2O_4) (Sigma-Aldrich, #A6756), arsenic trioxide (As_2O_3) (Sigma-Aldrich, #17971), 3-bromopyruvate (3BP) (Sigma-Aldrich, #16490), iodoacetate (IA) (Sigma-Aldrich, #I2512), or koningic acid (KA) were added. After 24 hours, cell viability assays were carried out using MTT as previously described. IC_{50} values of drug concentrations were used unless otherwise stated.

2.6.4 Cell viability assays

For all cell lines, $5x10^3$ cells/well were seeded in triplicate a 96-well plate and allowed to adhere for 24 hours. The following day, vehicle or KA was added to each well at the respective concentrations. After 24 hours, the media was aspirated and replaced with 100 μl phenol-red free RPMI-1640 (Gibco) and 12mM 3-[4,5-Dimethylthiazol-2-yl]-2,5-diphenyltetrazolium (MTT) (Thermo Fisher Scientific, #M6494) was added to the cells. After 4 hours, the media containing MTT was aspirated and 50 μl DMSO was added to dissolve the formazan and read at 540nm. For HEK293T cells, 100μl of SDS-HCl solution was added to each well and incubated for 4 hours at 37˚C, followed by absorbance reading at 570nm.

2.6.5 Nutrient supplementation in media

For HCT116 and KA-sensitive cell lines, $5x10^3$ cells/well were seeded in triplicate with complete RPMI-1640 media in 96-well plates and allowed to adhere for 24 hours. The following day, the respective treatment media was added in the absence or presence of KA at the cell lines' IC_{50}. MTT assays were carried out as previously described. All treatment media used were as follows: Low Glucose Media: RPMI-1640 with 0.5mM glucose (VWR, #97061-168), 10% heat-inactivated FBS, 100 U/ml penicillin and 100 μg/ml streptomycin with or without 3mM N-acetyl-cysteine (NAC) (Sigma-Aldrich, #A9165); Pyruvate Media: RPMI-1640 with 5mM pyruvate (Santa Cruz Biotechnology, #sc-208397), 10% heat-inactivated FBS, 100 U/ml penicillin and 100 μg/ml streptomycin with or without 3mM NAC; Lactate Media: RPMI-1640 with 5mM lactate (Santa Cruz, Biotechnology, #sc-253582), 10% heat-inactivated FBS, 100 U/ml penicillin and 100 μg/ml streptomycin with or without 3mM NAC; Serine Media: RPMI-1640 with 2mM additional serine (Amresco, #1B1103), 10% heat-inactivated FBS, 100 U/ml penicillin and 100 μg/ml streptomycin with or without 3mM NAC; Serine and Lactate Media: RPMI-1640 with 2mM additional serine, 5mM lactate, 10% heat-inactivated FBS, 100 U/ml penicillin and 100 μg/ml streptomycin; 3-phosphoglycerate (3PG) Media: RPMI-1640 with 2mM 3PG (Sigma-Aldrich, #P8877), 10% heat-inactivated FBS, 100 U/ml penicillin and 100 μg/ml streptomycin. Cells were grown at 37 °C with 5% CO_2.

2.6.6 Tumor cell line sensitivity analysis

One-dose and five-dose screens were carried out by the Developmental

Therapeutics Program (DTP) at the National Cancer Institute at National Institutes of Health (Bethesda, MD USA) on a panel of 59 independent cancer cell lines (Shoemaker, 2006). For the one-dose screen, 10μM KA or 0.01% DMSO (Vehicle) was used and for the five-dose screen, concentrations of 0-100μM KA or vehicle was used. The tumor cell lines were all grown in RPMI-1640 media containing 5% FBS and 2mM L-glutamine. Cells were seeded at 5,000 to 40,000 cells/well, depending on cell line doubling time, in 96-well plates containing 100μl media and incubated at 37˚C, 5% CO_2 for 24 hours before addition of KA. After 24 hours, two plates of each cell line were fixed *in situ* with TCA, to represent a measurement of the population of each cell line at the time of treatment. Following addition of vehicle or KA, the plates were incubated for 48 hours at 37˚C, 5% CO_2. For adherent cells, cold TCA was added to fix the cells *in situ* and incubated for 60 minutes at 4˚C. The supernatant was discarded, and the plates were washed five times with tap water and left to air dry. Sulforhodamine (SRB) solution at 0.4% (w/v) in 1% acetic acid was added to each well, and plates were incubated for 10 minutes at room temperature. After staining, unbound dye was removed by washing five times with 1% acetic acid that the plates were left to air dry. Bound stain was solubilized with 10 mM trizma base, and the absorbance was read at 515nm. For suspension cells, the methodology remained the same except the assay was terminated by fixing settled cells at the bottom of the wells by adding 80% TCA. Time zero (Tz), control growth (C), treatment growth (Ti) with the drug at one and five concentration levels, percent growth inhibition (GI), and lethal concentrations (LC) were recorded. Data for the BT-474 cell line was added to the one-dose screen and five-dose screen.

2.6.7 GAPDH activity assay

Using a GAPDH Activity Assay Kit (BioVision, #K680), all cells were seeded at $1x10^6$ cells per 10cm plate with either 0.01% DMSO (Vehicle) or KA. After 24 hours, cells were lysed, NADH standard curve was made, and cells were measured at 450 nm in kinetic mode for 60 minutes at 37˚C according to the manufacturer's instructions.

2.6.8 Lentiviral transfection and transduction

KAr-GAPDH cDNA was made by *de novo* gene synthesis (Origene) and subcloned into pLenti-C-Myc-DDK-IRES-Puro Expression Vector (KAr-GAPDH) (Origene/Blue Heron). HEK293T cells were seeded at $1x10^6$ cells per 10 cm plate in DMEM (Gibco) supplemented with 10% Heat-Inactivated FBS, 100 U/mL penicillin, and 100 mg/ml streptomycin and allowed to adhere and reach 70% confluency. After, 6 µg KAr-GAPDH, (Origene/Blue Heron, cDNA: D14519.1) or empty vector (EV) (Origene, #PS100069), 4 µg PsPAX2 packaging vector (Addgene, #12260), and 2 µg PMD2.G envelope expressing plasmid (Addgene, #12259) were diluted into 600µl jetPRIME buffer (Polyplus Transfection, #114-07) and vortexed. Next, 24µl jetPRIME transfection reagent (Polyplus Transfection, #114-07) was added to the mixture, vortexed for 10 seconds, and centrifuged for 30 seconds. The mixture was left to incubate for 10 minutes at room temperature. Next, 600 µl of the transfection mix was added to each plate dropwise into serum containing DMEM, evenly distributed, and incubated at 37˚C, 5% CO_2. The transfection medium was replaced with fresh medium after 4 hours and returned to the incubator for 24 hours. Virus was collected and filtered with 0.4 µm filter (VWR International). HCT116 cells were seeded at 50% confluency per 10 cm plate in RPMI-

1640 (Gibco) supplemented with 10% Heat-Inactivated FBS, 100 U/mL penicillin and 100 mg/ml streptomycin and allowed to adhere overnight. The next day, virus-rich media was added to cells (1:1 with fresh RPMI-1640 media) for 24 hours. After, virus-rich media was removed, and cells were plated with fresh RPMI-1640 media. HEK293T and HCT116 cells were incubated with 1 μg/ml puromycin for 48 hours and EV and KAr-GAPDH expressing HEK293T and HCT116 cells were verified by western blotting.

2.6.9 Immunoblotting

Samples were homogenized in 200 μl 1X RIPA buffer (VWR International) supplemented with 100 μM phenylmethylsulfonyl fluoride (PMSF), 2 μg/μl aprotinin, 5 μg/ml pepstatin, 1X phosphatase inhibitor cocktail, and 2 mM Dithiothreitol (DTT). And centrifuged at 14,000 rpm for 30 minutes at 4˚C. The supernatant was transferred to a clean tube and a Bradford Assay (Bio-Rad) was carried out to quantify protein concentration. Protein samples were loaded onto TGX stain-free precast gels (Bio-Rad) and transferred to polyvinylidene difluoride (PVDF) membranes. Membranes were blocked in 5% dry non-fat milk in TBST and incubated with anti-GAPDH (Abcam, #ab9485) 1:2500 in 5% BSA in TBST and anti-Actin 1:2000 (Thermo Scientific, #MA5-15739) in 5% dry non-fat milk in TBST. Horseradish peroxidase-conjugated anti-mouse (Rockland, #610-1302) and anti-rabbit (Rockland, #611-1302), 1:2000, were used as secondary antibodies. Chemiluminescent signals were detected with Clarity Western ECL Detection Kit (Bio-Rad, #1705061) and imaged using the ChemiDoc Touch Imaging System (Bio-Rad).

2.6.10 Culture and isolation of koningic acid from *Trichoderma virens*

Trichoderma virens (G-4) (ATCC, MYA-297) was cultured aerobically at 26.8˚C for 5 days on potato dextrose agar (Fisher scientific, #DF0013-17-6) plates (25 cm). Tween-20 (0.1% in H_2O, 15 mL) was added to each plate and spores were scraped off the surface of the agar and fungal tissue using a cell spreader. The concentration of spore suspensions was determined by counting spores using a hemocytometer. Then, 1 L of liquid medium in a 2 L Erlenmeyer flask was inoculated with $1x10^6$ spores mL^{-1}. The culture broth consisted of malt extract medium containing 3% malt extract (BD Biosciences, #211677), 2% glucose (VWR, #97061-168), and 0.1% peptone (BD Biosciences, #211677). Liquid cultures were placed at 25˚C with shaking at 200 rpm for 7 days.

After 7 days, liquid fungal cultures including fungal tissue and media were frozen using a dry ice acetone bath, and lyophilized. The lyophilized residues were extracted with 500 mL of methanol (Fisher Scientific, #A452) (containing 0.2 % acetic acid (Fisher Scientific, #A38-500)) for 3.5 hours with vigorously stirring. Extracts were filtered over cotton, evaporated to dryness, and stored in 8 mL vials.

2.6.11 Isolation and purification of koningic acid

Methanol extracts derived from 1 L cultures were fractionated using large-scale reverse-phase flash chromatography on a Teledyne ISCO CombiFlash chromatography system with a Teledyne C18 gold (100 gram) column with acetonitrile (organic phase) and 0.1 % acetic acid in water (aqueous phase) as solvents at a flow rate of 60 mL/min. A linear ramp from 0 % organic to 100 % organic over 30 min was used and fractions

containing KA were collected, evaporated to dryness, and transferred to 8 mL glass vials. Then, KA was dissolved in a minimal volume of methanol and further purified via semi-preparative HPLC using an Agilent XDB C-18 column (25 cm x 10 mm, 5 μm particle diameter) acetonitrile (organic phase) and 0.1 % acetic acid in water (aqueous phase) as solvents at a flow rate of 3.6 mL/min. A solvent gradient scheme was used, starting at 5 % organic for 3 min, followed by a linear increase to 100 % organic over 27 min, holding at 100 % organic for 5 min, then decreasing back to 5 % organic over 0.1 min, and holding at 5 % organic for the final 4.9 min, for a total of 40 min. Fractions containing pure KA were collected, evaporated to dryness, and transferred to 8 mL glass vials and stored at -20 ˚C.

2.6.12 U-^{13}C-glucose stable isotope labeling

All cells (300,000 cells/well) were plated in a 6-well plate and allowed to adhere to the plate for 24 hours. Cells were then treated with either vehicle or KA for 6 hours, then replaced with RPMI-1640 media containing 11mM U^{13}C-glucose (Cambridge Isotope Laboratories, Inc., #CLM-1396) and vehicle or KA for 0-24 hours. Metabolites were then extracted.

2.6.13 Metabolite extraction

Metabolite extraction and subsequent Liquid-Chromatography coupled to High Resolution Mass Spectrometry (LC-HRMS) for polar metabolites of each cell line was carried out using a Q Exactive Plus as previously described (Liu et al., 2014a; Liu et al., 2014b). For culture from adherent cell lines, media was quickly aspirated. Next, 1 mL of extraction solvent (80% methanol/water) cooled to -80˚C was added immediately to each

well and the plates were then transferred to -80˚C for 15 minutes. After, the plates were removed, and the cells were scraped into the extraction solvent on dry ice. For tissue, the sample was homogenized in liquid nitrogen and then 5 to 10 mg was weighed in a new Eppendorf tube. Ice-cold extraction solvent (200 µl) was added to each tissue sample and homogenized using a tissue homogenizer. The homogenate was incubated on ice for 10 minutes. For plasma or media, 20 µl was transferred to a new Eppendorf tube containing 80 µl HPLC grade water. Next, 400 µl of ice-cold methanol was added to the sample for a final methanol concentration of 80% (*v/v*). Samples were incubated on ice for 10 minutes. For absolute quantitation of KA in plasma, 0-10µM KA standards were added to extraction solvent before centrifugation. All metabolite extractions were centrifuged at 20,000 *g* at 4˚C for 10 minutes. Finally, the solvent in each sample was evaporated using a speed vacuum for metabolite analysis. For polar metabolite analysis, the cell metabolite extract was first dissolved in 15 µl water, followed by dilution with 15 µl methanol/acetonitrile (1:1 *v/v*) (optima LC-MS grade, Fisher Scientific, methanol, #A456; acetonitrile, #A955). Samples were centrifuged at 20,000 *g* for 10 minutes at 4˚C and the supernatants were transferred to LC vials. The injection volume for polar metabolite analysis was 5 µl.

2.6.14 Liquid chromatography

An XBridge amide column (100 x 2.1 mm i.d., 3.5 µm; Waters) was employed on a Dionex (Ultimate 3000 UHPLC) for compound separation at room temperature. Mobile phase A is water with 5mM Ammonium Acetate, pH 6.9, and mobile phase B is 100% Acetonitrile. The gradient is linear as follows: 0 minutes, 85% B; 1.5 minutes, 85% B;

5.5 minutes, 35% B; 10 minutes, 35% B; 10.5 minutes, 35% B; 10.6 minutes, 10% B; 12.5 minutes, 10% B; 13.5 minutes, 85% B; and 20 minutes, 85% B. The flow rate was 0.15 ml/min from 0 to 5.5 minutes, 0.17 ml/min from 6.9 to 10.5 minutes, 0.3 ml/min from 10.6 to 17.9 minutes, and 0.15 ml/min from 18 to 20 minutes. All solvents are LC-MS grade and purchased from Fisher Scientific.

2.6.15 Mass spectrometry

The Q Exactive Plus MS (Thermo Scientific) is equipped with a heated electrospray ionization probe (HESI) and the relevant parameters are as listed: evaporation temperature, 120˚C; sheath gas, 30; auxillary gas, 10; sweep gas, 3; spray voltage, 3.6 kV for positive mode and 2.5 kV for negative mode. Capillary temperature was set at 320˚C, and S lens was 55. A full scan range from 70 to 900 (*m/z*) was used. The resolution was set at 70,000. The maximum injection time was 200 ms. Automated gain control (AGC) was targeted at $3x10^6$ ions. For targeted MS/MS analysis of KA, the isolation width of the precursor ion was set at 1.5 (*m/z*), high energy collision dissociation (HCD) was 35%, and max IT was 100 ms. The resolution and AGC were 70,000 and 200,000 respectively.

2.6.16 Peak extraction and data analysis

Raw data collected from LC-Q Exactive Plus MS was processed on Sieve 2.0 (Thermo Scientific). Peak alignment and detection were performed according to the protocol described by Thermo Scientific. For a targeted metabolite analysis, the method “peak alignment and frame extraction” was applied. An input file of theoretical *m/z* and detected retention time of 197 known metabolites was used for targeted metabolite

analysis with data collected in positive mode, while a separate input file of 262 metabolites was used for negative mode. *m/z* width was set to 10 ppm. The output file including detected *m/z* and relative intensity in different samples was obtained after data processing. If the lowest integrated mass spectrometer signal (MS intensity) was less than 1000 and the highest signal was less than 10,000, then this metabolite was considered below the detection limit and excluded for further data analysis. If the lowest signal was less than 1000, but the highest signal was more than 10,000, then a value of 1000 was imputed for the lowest signals. Mass isotopomer distributions (MID) were calculated and samples were normalized by comparing the ratio of glucose-derived labeled metabolites to unlabeled metabolites within each sample. Quantitation and statistics were calculated using Microsoft Excel and GraphPad Prism 6.0.

2.6.17 Kinetic flux profiling

The time-dependent lactate labeling pattern was modeled as with the following equation:

$$\frac{[X^*]}{X^T} = 1 - e^{-\frac{f_X}{X^T}t}$$

In which $[X^*]$ is the concentration of labeled lactate, X^T is the total concentration (both labeled and unlabeled) of lactate, f_X is the lactate production flux. This model was fit to lactate MIDs using the fit() function in MATLAB to determine relative lactate production fluxes. Relative lactate pool sizes were estimated from MS signal intensities.

2.6.18 Thermodynamic and kinetic analysis

Mathematical model of glycolysis downloaded from the BioModels Database

repository (EMBL-EBI, http://www.ebi.ac.uk/biomodels-main/, MODEL1504010000) was first translated to C++ code using the SBML translator module in the Systems Biology Workbench (http://sbw.sourceforge.net/) (Bergmann and Sauro, 2006; Sauro et al., 2003) then simulated using the ODE solver gsl_odeiv2_step_msbdf in the GNU Scientific Library (Free Software Foundation, http://www.gnu.org/software/gsl/). FCC of an enzymatic step was computed by replacing V_{max} of the enzyme with $1.01V_{max}$ and $V_{max}/1.01$ while keeping all other parameters fixed, computing the corresponding steady state lactate fluxes (f_{Lac}), then estimating FCC accordingly: $FCC = \frac{\log f_{Lac}(1.01V_{max}) - \log f_{Lac}(\frac{V_{max}}{1.01})}{2\log 1.01}$. ΔGs were calculated from standard reaction free energies and steady state concentrations of the metabolites. Extent of the Warburg Effect was tuned by increasing V_{max}s of the glycolytic enzymes GLUT, HK, PFK, PGK, MCT from 0.1 to 10 folds of their original values and decreasing V_{max} of PDH from 10 to 0.1 folds of its original value simultaneously. Extent of the Warburg Effect was quantified by ratio of lactate production flux to oxidative phosphorylation flux.

2.6.19 Integrative analysis and drug response and multi-omics data

All correlations were carried out using pearson or spearman correlations to GI_{50} values of KA to each of the 59 cell lines tested from the NCI-60 cell line panel using GraphPad Prism 6.0 or R Statistical Programming (The R Foundation, https://www.r-project.org/). Metabolic consumption and excretion rates from NCI-60 cell line panel were acquired from Jain *et al*. 2012 (Jain et al., 2012). Cell size and doubling time were acquired from Dolfi et al. 2013 (Dolfi et al., 2013). Gene expression analyses were

completed by manually dividing the 59 cell lines tested with KA into two groups (KA-resistant and KA-sensitive) based on the distribution of GI_{50} values. Gene set enrichment analysis (GSEA) was then performed (The Broad Institute, http://software.broadinstitute.org/gsea/index.jsp) using all of the genes for differential expression analysis between KA-sensitive and KA-resistant cell lines. For protein expression analyses the efficacy of KA (in terms of GI50) were plotted against the absolute protein quantification of glycolytic genes in the NCI-60 cell line panel. Protein quantification data was obtained from Gholami et al. 2013 (Gholami et al., 2013) and genes were filtered and mapped to their KEGG biochemical pathways as previously described in Madhukar et al. 2015 (Madhukar et al., 2015). P-values, R^2, Pearson correlation values were calculated using the cor.test function within R. Mutation and copy number alterations (CNAs) were obtained from cBioPortal (http://www.cbioportal.org) for Cancer Genomics. Random distributions for the Q-Q plots were generated by permuting the original data 1000 times and calculating Spearman correlation coefficients accordingly. Error bars on the Q-Q plots represent for standard deviation of the quantiles of the 1000 random distributions. Drug activity z-scores of the targeted therapies calculated from their GI_{50} values on the NCI-60 cell line panel were available from CellMiner (National Cancer Institute, https://discover.nci.nih.gov/cellminer/). ROC curves were created for the targeted therapies using the perfcurve() function in MATLAB (MathWorks, Inc, https://www.mathworks.com/product/matlab.html), by labeling the cell lines according to presence of the genomic feature targeted and using drug activities as predictive scores. For KA, cell lines were labeled ‘high’ or ‘low’ based on whether the

glucose or lactate flux in this cell line is higher or lower than the median value among all cell lines and ROC curves were created similarly.

2.6.20 Koningic acid docking to GAPDH

The virtual compound screening ZINC Database (http://zinc.docking.org) was used to obtain a ready-to-dock format (mol2) of KA (ZINC 15272438) (Irwin and Shoichet, 2005; Irwin et al., 2012). Next, docking between KA and the human GAPDH structure was performed using molecular docking on the Swiss Dock server using default settings (http://www.swissdock.ch) (Grosdidier et al., 2011). Since previous studies have already shown that the epoxide group of KA interacts with GAPDH active site cysteine 152 via alkylation, the highest scoring binding model with this interaction was used to infer the drug docking (Sakai et al., 1988, 1991). The 3-D structure of the docked model was analyzed using UCSF Chimera 1.10.2 (http://www.rbvi.ucsf.edu/chimera) (Pettersen et al., 2004). Amino acid hydrophobicity was assigned to the structure as an attribute in Chimera with a pre-defined hydrophobicity scale (Kyte and Doolittle, 1982).

2.6.21 GAPDH protein multiple sequence alignment comparisons

All multiple sequence alignments were carried out using Clustal Omega https://www.ebi.ac.uk/Tools/msa/clustalo) (Sievers et al., 2011). For phylogenetic analyses, outputs from Clustal Omega were used and inputted into Clustal W2-Phylogeny (https://www.ebi.ac.uk/Tools/phylogeny/clustalw2_phylogeny/) (Larkin et al., 2007) to generate a phylogenetic tree from the homology alignment. Percent Identity Matrices were calculated based on the data output from Clustal W2-Phylogeny.

2.6.22 Analysis of metabolomics data

GENE-E and Morpheus software were used for hierarchal clustering and heatmap generation (The Broad Institute, https://software.broadinstitute.org/GENE-E/index.html). For hierarchal clustering, spearman correlation parameters were implemented for row and column parameters, with the exception of putative GAPDH drug response data, in which hierarchal clustering for row parameters only was used. Quantile normalization was used to normalize the data, with the exception of glycolysis data in HCT116 cells, in which and $\log_2$ normalization was used.

For pathway enrichment analyses, MetaboAnalyst 3.0 was used (http://www.metaboanalyst.ca/faces/home.xhtml) (Xia et al., 2015). To do this, HMDB IDs from the metabolites that were significantly enriched in their respective treatment groups (greater than $\pm\log_2(2)$ fold change with a $p<0.05$) were inputted. The pathway library that was chosen was *Homo sapiens* and Fishers' Exact test was the method employed for over-representation analysis. For pathway topology analysis, relative betweenness centrality was chosen as the node importance measure.

2.6.23 Animal experiments

All animal experiments were performed in compliance with guidelines of the Animal Welfare Act and the guide for the care and use of laboratory animals following protocols approved by the Duke University Institutional Animal Care and Use Committee (IACUC) protocol number A011-16-01. For BT-474 tumor bearing mice, 6-week old female *Foxn1*^{nu} mice (The Jackson Laboratory, 007850) were ovariectomized and subcutaneously implanted at surgery with 0.72 mg/60 day estradiol pellets (Innovative

Research of America, #SE-121). Septra antibiotic treatment (Hi-Tech Pharmacal, 50383-823-16) (drinking water) was initiated at this time and continued throughout the study. Two days later, $3x10^6$ BT-474 breast cancer cells (mixed 1:1 with Matrigel) (Corning, #354234) were injected orthotopically into the mammary fat pad. For MDA-MB-231 tumor bearing mice, 6-week old female *nu/nu* mice (internal breeding colony) were injected orthotopically with $3x10^6$ MDA-MB-231 breast cancer cells (mixed 1:1 with Matrigel) into the mammary fat pad. Tumor volume, animal body weight, and behavior were evaluated 3 times weekly until tumors reached $200mm^3$ volume. At that point, BT-474 tumor bearing mice were randomized to the following treatment groups for daily intraperitoneal (IP) injections to determine the maximum tolerated dose (MTD): vehicle (5% DMSO/95% sterile saline), 1 mg/kg KA, 2.5 mg/kg KA, 5 mg/kg KA, and 10 mg/kg KA. MDA-MB-231 tumor bearing mice were randomized to vehicle (5% DMSO/95% sterile saline) and 1 mg/kg KA. KA was resuspended in DMSO prior to dilution in saline immediately prior to use. Mice were evaluated during treatment daily for behavior and 3X weekly for weight loss. Mice receiving >1 mg/kg KA were euthanized 24-48 hours after administration due to humane endpoints (behavior, hematuria, and anemia), and 1 mg/kg KA was determined to be the MTD. Tumor measurements were taken three times weekly for 2 weeks. For efficacy studies, after 2 weeks of treatment, the mice were anesthetized with isoflurane and euthanized by cervical dislocation 30 minutes after the final administration of KA prior to harvest of tumors and tissues for analysis. For pharmacokinetics analysis, mice were treated with vehicle or 1 mg/kg KA from 0-24 hours, and anesthetized and euthanized at different time points by the same methods

already described, followed by tumor and tissue collection. For metabolomics, tumors, tissue, and plasma were flash frozen in liquid nitrogen. For immunohistochemistry, tumors and tissue were fixed in 10% formalin. For complete blood count (CBC) analysis, whole blood was mixed with 0.9% sodium chloride (1:200) and cells were counted using a hemocytometer.

2.6.24 Paraffin embedding and immunohistochemistry

All paraffin embedding, tissue sectioning, and immunohistochemical (IHC) staining was carried out by Duke University Pathology Research Histology and Immunohistochemistry Laboratory shared resource facility. For tissue embedding and sectioning, previously established protocols were followed (Fischer et al., 2007). For hematoxylin and eosin (H&E) staining of tissue sections, standard protocols were used (Fischer et al., 2008). For Ki67 staining for cell proliferation, Ki67 was detected by biotinylated goat anti-rabbit 1:300 (Thermo Scientific, # BA-1000) and the ABC Elite (Vector, #PK-7100). For GAPDH staining to detect GAPDH localization, GAPDH was detected by the anti-rabbit HQ 1:200 (Abcam, #760-4815) and the anti-HQ system (Roche/Ventana, #760-4820). All slides were observed and photographed under the microscope.

To quantify Ki-67 staining, ImageJ (National Institute of Health, https://imagej.nih.gov/ij/index.html) was used. To do this, a threshold was set (8-Bit Auto Threshold) until all the stained areas were selected. Next, specific parameters were chosen for measurements (area, min & max gray value, area fraction, limit to threshold). After, intensity measurements were performed, and output was area. The areas were

compared to the background to achieve percentage of staining.

2.6.25 Quantification and statistical analysis

Unless otherwise noted, all error bars were reported ±SEM with n=3 independent biological measurements and statistical tests resulting in p-value computations were computed using a student's t-test two tailed. Tumor volumes in the animal studies were analyzed by 2-way ANOVA of time matched values, followed by Bonferroni multiple comparison test. All statistics were computed using GraphPad Prism 6 (GraphPad, https://www.graphpad.com/scientific-software/prism).

2.6.26 Data and software availability

Metabolomics data have been deposited in Mendeley Data and are accessible through http://dx.doi.org/10.17632/wmk2prwynj.1.

2.7 References

Barber, R.D., Harmer, D.W., Coleman, R.A., and Clark, B.J. (2005). GAPDH as a housekeeping gene: analysis of GAPDH mRNA expression in a panel of 72 human tissues. Physiol Genomics *21*, 389-395.

Bergmann, F.T., and Sauro, H.M. (2006). SBW - A modular framework for systems biology. Proceedings of the 2006 Winter Simulation Conference, Vols 1-5, 1637-+.

Bowden, A.C. (1999). Metabolic control analysis in biotechnology and medicine. Nat Biotechnol *17*, 641-643.

Campbell-Burk, S., Jones, K., and Shulman, R. (1987). Phosphorus-31 NMR saturation-transfer measurements in Saccharomyces cerevisiae: characterization of phosphate exchange reactions by iodoacetate and antimycin A inhibition. Biochemistry *26*, 7483-7492.

Collins, F.S., and Varmus, H. (2015). A new initiative on precision medicine. N Engl J Med *372*, 793-795.

Dai, J., Weinberg, R.S., Waxman, S., and Jing, Y.K. (1999). Malignant cells can be sensitized to undergo growth inhibition and apoptosis by arsenic trioxide through modulation of the glutathione redox system. Blood *93*, 268-277.

Davidson, S.M., Papagiannakopoulos, T., Olenchock, B.A., Heyman, J.E., Keibler, M.A., Luengo, A., Bauer, M.R., Jha, A.K., O'Brien, J.P., Pierce, K.A*., et al.* (2016). Environment Impacts the Metabolic Dependencies of Ras-Driven Non-Small Cell Lung Cancer. Cell Metab *23*, 517-528.

Dolfi, S.C., Chan, L.L.-Y., Qiu, J., Tedeschi, P.M., Bertino, J.R., Hirshfield, K.M., Oltvai, Z.N., and Vazquez, A. (2013). The metabolic demands of cancer cells are coupled to their size and protein synthesis rates. Cancer & metabolism *1*, 1.

Endo, A., Hasumi, K., Sakai, K., and Kanbe, T. (1985). Specific inhibition of glyceraldehyde-3-phosphate dehydrogenase by koningic acid (heptelidic acid). The Journal of antibiotics *38*, 920-925.

Fell, D.A. (1992). Metabolic control analysis: a survey of its theoretical and experimental development. Biochem J *286 (Pt 2)*, 313-330.

Fischer, A.H., Jacobson, K.A., Rose, J., and Zeller, R. (2007). Paraffin embedding tissue samples for sectioning. CSH protocols *2008*, pdb. prot4989-pdb. prot4989.

Fischer, A.H., Jacobson, K.A., Rose, J., and Zeller, R. (2008). Hematoxylin and eosin staining of tissue and cell sections. Cold Spring Harbor Protocols *2008*, pdb. prot4986.

Galluzzi, L., Kepp, O., Vander Heiden, M.G., and Kroemer, G. (2013). Metabolic targets for cancer therapy. Nat Rev Drug Discov *12*, 829-846.

Ganapathy-Kanniappan, S., Geschwind, J.-F.H., Kunjithapatham, R., Buijs, M., Vossen, J.A., Tchernyshyov, I., Cole, R.N., Syed, L.H., Rao, P.P., and Ota, S. (2009). Glyceraldehyde-3-phosphate dehydrogenase (GAPDH) is pyruvylated during 3-bromopyruvate mediated cancer cell death. Anticancer research *29*, 4909-4918.

Garber, K. (2016). Cancer anabolic metabolism inhibitors move into clinic (Nature Research).

Gholami, A.M., Hahne, H., Wu, Z.X., Auer, F.J., Meng, C., Wilhelm, M., and Kuster, B. (2013). Global Proteome Analysis of the NCI-60 Cell Line Panel. Cell Reports *4*, 609-

620.
Grosdidier, A., Zoete, V., and Michielin, O. (2011). SwissDock, a protein-small molecule docking web service based on EADock DSS. Nucleic Acids Res *39*, W270-277.
Hay, N. (2016). Reprogramming glucose metabolism in cancer: can it be exploited for cancer therapy? Nature Reviews Cancer.
Heinrich, R., and Schuster, S. (1996). The regulation of cellular systems (New York: Chapman & Hall).
Hensley, C.T., Faubert, B., Yuan, Q., Lev-Cohain, N., Jin, E., Kim, J., Jiang, L., Ko, B., Skelton, R., Loudat, L.*, et al.* (2016). Metabolic Heterogeneity in Human Lung Tumors. Cell *164*, 681-694.
Iorio, F., Knijnenburg, T.A., Vis, D.J., Bignell, G.R., Menden, M.P., Schubert, M., Aben, N., Goncalves, E., Barthorpe, S., Lightfoot, H.*, et al.* (2016). A Landscape of Pharmacogenomic Interactions in Cancer. Cell *166*, 740-754.
Irwin, J.J., and Shoichet, B.K. (2005). ZINC--a free database of commercially available compounds for virtual screening. J Chem Inf Model *45*, 177-182.
Irwin, J.J., Sterling, T., Mysinger, M.M., Bolstad, E.S., and Coleman, R.G. (2012). ZINC: a free tool to discover chemistry for biology. J Chem Inf Model *52*, 1757-1768.
Israelsen, W.J., Dayton, T.L., Davidson, S.M., Fiske, B.P., Hosios, A.M., Bellinger, G., Li, J., Yu, Y., Sasaki, M., Horner, J.W.*, et al.* (2013). PKM2 isoform-specific deletion reveals a differential requirement for pyruvate kinase in tumor cells. Cell *155*, 397-409.
Jain, M., Nilsson, R., Sharma, S., Madhusudhan, N., Kitami, T., Souza, A.L., Kafri, R., Kirschner, M.W., Clish, C.B., and Mootha, V.K. (2012). Metabolite profiling identifies a key role for glycine in rapid cancer cell proliferation. Science *336*, 1040-1044.
Jung, D.W., Kim, W.H., Seo, S., Oh, E., Yim, S.H., Ha, H.H., Chang, Y.T., and Williams, D.R. (2014). Chemical targeting of GAPDH moonlighting function in cancer cells reveals its role in tubulin regulation. Chem Biol *21*, 1533-1545.
Kyte, J., and Doolittle, R.F. (1982). A simple method for displaying the hydropathic character of a protein. J Mol Biol *157*, 105-132.
Larkin, M.A., Blackshields, G., Brown, N.P., Chenna, R., McGettigan, P.A., McWilliam, H., Valentin, F., Wallace, I.M., Wilm, A., Lopez, R.*, et al.* (2007). Clustal W and Clustal X version 2.0. Bioinformatics *23*, 2947-2948.
Lehninger, A.L., Nelson, D.L., and Cox, M.M. (2013). Lehninger principles of biochemistry, 6th edn (New York: W.H. Freeman).
Liberti, M.V., and Locasale, J.W. (2016). The Warburg effect: how does it benefit cancer cells? Trends in biochemical sciences *41*, 211-218.
Liu, X., Romero, I.L., Litchfield, L.M., Lengyel, E., and Locasale, J.W. (2016). Metformin Targets Central Carbon Metabolism and Reveals Mitochondrial Requirements in Human Cancers. Cell Metab *24*, 728-739.
Liu, X., Ser, Z., Cluntun, A.A., Mentch, S.J., and Locasale, J.W. (2014a). A strategy for sensitive, large scale quantitative metabolomics. J Vis Exp.
Liu, X., Ser, Z., and Locasale, J.W. (2014b). Development and quantitative evaluation of a high-resolution metabolomics technology. Anal Chem *86*, 2175-2184.
Locasale, J.W. (2013). Serine, glycine and one-carbon units: cancer metabolism in full circle. Nat Rev Cancer *13*, 572-583.

Madhukar, N.S., Warmoes, M.O., and Locasale, J.W. (2015). Organization of enzyme concentration across the metabolic network in cancer cells. PLoS One *10*, e0117131.
Mayers, J.R., Torrence, M.E., Danai, L.V., Papagiannakopoulos, T., Davidson, S.M., Bauer, M.R., Lau, A.N., Ji, B.W., Dixit, P.D., Hosios, A.M*., et al.* (2016). Tissue of origin dictates branched-chain amino acid metabolism in mutant Kras-driven cancers. Science *353*, 1161-1165.
Mulleder, M., Calvani, E., Alam, M.T., Wang, R.K., Eckerstorfer, F., Zelezniak, A., and Ralser, M. (2016). Functional Metabolomics Describes the Yeast Biosynthetic Regulome. Cell *167*, 553-565 e512.
Németi, B., and Gregus, Z. (2005). Reduction of arsenate to arsenite by human erythrocyte lysate and rat liver cytosol–characterization of a glutathione-and NAD-dependent arsenate reduction linked to glycolysis. Toxicological Sciences *85*, 847-858.
Noor, E., Bar-Even, A., Flamholz, A., Reznik, E., Liebermeister, W., and Milo, R. (2014). Pathway thermodynamics highlights kinetic obstacles in central metabolism. PLoS computational biology *10*, e1003483.
Pettersen, E.F., Goddard, T.D., Huang, C.C., Couch, G.S., Greenblatt, D.M., Meng, E.C., and Ferrin, T.E. (2004). UCSF Chimera—a visualization system for exploratory research and analysis. Journal of computational chemistry *25*, 1605-1612.
Raez, L.E., Papadopoulos, K., Ricart, A.D., Chiorean, E.G., Dipaola, R.S., Stein, M.N., Rocha Lima, C.M., Schlesselman, J.J., Tolba, K., Langmuir, V.K*., et al.* (2013). A phase I dose-escalation trial of 2-deoxy-D-glucose alone or combined with docetaxel in patients with advanced solid tumors. Cancer Chemother Pharmacol *71*, 523-530.
Sakai, K., Hasumi, K., and Endo, A. (1988). Inactivation of rabbit muscle glyceraldehyde-3-phosphate dehydrogenase by koningic acid. Biochim Biophys Acta *952*, 297-303.
Sakai, K., Hasumi, K., and Endo, A. (1990). Two glyceraldehyde-3-phosphate dehydrogenase isozymes from the koningic acid (heptelidic acid) producer Trichoderma koningii. European journal of biochemistry / FEBS *193*, 195-202.
Sakai, K., Hasumi, K., and Endo, A. (1991). Identification of koningic acid (heptelidic acid)-modified site in rabbit muscle glyceraldehyde-3-phosphate dehydrogenase. Biochim Biophys Acta *1077*, 192-196.
Sauro, H.M., Hucka, M., Finney, A., Wellock, C., Bolouri, H., Doyle, J., and Kitano, H. (2003). Next generation simulation tools: the Systems Biology Workbench and BioSPICE integration. OMICS *7*, 355-372.
Shestov, A.A., Liu, X., Ser, Z., Cluntun, A.A., Hung, Y.P., Huang, L., Kim, D., Le, A., Yellen, G., Albeck, J.G*., et al.* (2014). Quantitative determinants of aerobic glycolysis identify flux through the enzyme GAPDH as a limiting step. Elife *3*, e03342.
Shoemaker, R.H. (2006). The NCI60 human tumour cell line anticancer drug screen. Nat Rev Cancer *6*, 813-823.
Sievers, F., Wilm, A., Dineen, D., Gibson, T.J., Karplus, K., Li, W., Lopez, R., McWilliam, H., Remmert, M., and Söding, J. (2011). Fast, scalable generation of high-quality protein multiple sequence alignments using Clustal Omega. Molecular systems biology *7*, 539.
Svensson, R.U., Parker, S.J., Eichner, L.J., Kolar, M.J., Wallace, M., Brun, S.N.,

Lombardo, P.S., Van Nostrand, J.L., Hutchins, A., Vera, L.*, et al.* (2016). Inhibition of acetyl-CoA carboxylase suppresses fatty acid synthesis and tumor growth of non-small-cell lung cancer in preclinical models. Nat Med *22*, 1108-1119.
Timmerman, L.A., Holton, T., Yuneva, M., Louie, R.J., Padro, M., Daemen, A., Hu, M., Chan, D.A., Ethier, S.P., van 't Veer, L.J.*, et al.* (2013). Glutamine Sensitivity Analysis Identifies the xCT Antiporter as a Common Triple-Negative Breast Tumor Therapeutic Target. Cancer cell *24*, 450-465.
Vander Heiden, M.G. (2013). Exploiting tumor metabolism: challenges for clinical translation. J Clin Invest *123*, 3648-3651.
Vander Heiden, M.G., Cantley, L.C., and Thompson, C.B. (2009). Understanding the Warburg effect: the metabolic requirements of cell proliferation. Science *324*, 1029-1033.
Vander Heiden, M.G., and DeBerardinis, R.J. (2017). Understanding the Intersections between Metabolism and Cancer Biology. Cell *168*, 657-669.
Vezina, C., Kudelski, A., and Sehgal, S.N. (1975). Rapamycin (AY-22,989), a new antifungal antibiotic. I. Taxonomy of the producing streptomycete and isolation of the active principle. The Journal of antibiotics *28*, 721-726.
Watanabe, H., Hasumi, K., Fukushima, Y., Sakai, K., and Endo, A. (1993). Cloning of two isozymes of Trichoderma koningii glyceraldehyde-3-phosphate dehydrogenase with different sensitivity to koningic acid. Biochim Biophys Acta *1172*, 43-48.
Weinberg, S.E., and Chandel, N.S. (2015). Targeting mitochondria metabolism for cancer therapy. Nat Chem Biol *11*, 9-15.
Xia, J., Sinelnikov, I.V., Han, B., and Wishart, D.S. (2015). MetaboAnalyst 3.0—making metabolomics more meaningful. Nucleic acids research *43*, W251-W257.
Yuneva, M.O., Fan, T.W., Allen, T.D., Higashi, R.M., Ferraris, D.V., Tsukamoto, T., Mates, J.M., Alonso, F.J., Wang, C., Seo, Y.*, et al.* (2012). The metabolic profile of tumors depends on both the responsible genetic lesion and tissue type. Cell Metab *15*, 157-170.

CHAPTER 3: EVOLVED RESISTANCE TO GAPDH INHIBITION RESULTS IN LOSS OF THE WARBURG EFFECT BUT RETAINS A DIFFERENT STATE OF GLYCOLYSIS[3]

3.1 Background and context

The previous chapter established koningic acid (KA) as a specific inhibitor of glyceraldehyde-3-phosphate dehydrogenase (GAPDH) with efficacy specifically in cells and tumors undergoing the Warburg Effect (WE). While these findings are a major advance to the therapeutic relevance of the WE, there remains a surprising lack of clarity in the field as to whether the WE is distinct from glycolysis. In this chapter, I used KA as a tool to toggle between transition states away from the WE by developing an evolved resistance model to GAPDH inhibition with KA and found that glycolysis can exist in multiple states with distinct metabolic outputs. More specifically, I found that cells which have evolved resistance to KA gain a selective pressure to lose the WE but remain dependent on glucose uptake and glycolysis. Thus, this study demonstrates that the WE and glycolysis are not simply one and the same, but rather can exist separately from one another with distinct metabolic functional outputs. Together, these findings providing rationale for continued efforts for therapeutic targeting of the WE.

---

[3] This chapter was adapted and modified from work currently under peer review: Liberti, M.V., Allen, A.E., Singleton, K.R., Guo, Z., Liu, J.O., Wood, K.C., and Locasale, J.W., 2018. Evolved resistance to GAPDH inhibition results in loss of the Warburg Effect but retains a different state of glycolysis. *In review*. Author Contributions: Conceptualization, M.V.L. and J.W.L.; Metabolomics, M.V.L.; Cell viability assays, M.V.L. and A.E.A., Nutrient restriction assays, M.V.L., Data analysis, M.V.L, A.E.A., K.R.S., K.C.W., Provision of essential reagents, Z.G., J.O.L.; All other experiments, M.V.L.; Writing, M.V.L. and J.W.L.; Supervision, M.V.L. and J.W.L.

3.2 Abstract

Aerobic glycolysis or the Warburg Effect (WE) is characterized by increased glucose uptake and incomplete oxidation to lactate. Although ubiquitous, the biological role of the WE is controversial and whether glucose metabolism is functionally different during fully oxidative glycolysis or during the WE is unknown. To investigate this question, I evolved resistance to koningic acid (KA), a natural product shown to be a specific inhibitor of glyceraldehyde-3-phosphate dehydrogenase (GAPDH), a rate-controlling glycolytic enzyme during the WE. I find that KA-resistant cells lose the WE but conduct glycolysis and remain dependent on glucose and central carbon metabolism. Consequentially this altered state of glycolysis leads to differential metabolic activity and requirements including emergent activities in and dependencies on fatty acid metabolism. Together, these findings reveal that, contrary to some recent reports, aerobic glycolysis is a functionally distinct entity from conventional glucose metabolism and leads to distinct metabolic requirements and biological functions.

3.3 Introduction

Glycolysis, the uptake and metabolism of glucose, is a set of chemical reactions conserved to the most primitive of organisms and is fundamental to sustaining life (Bar-Even et al., 2012). Together with the catabolism of amino acids and lipids, glycolysis is a component of central carbon metabolism. The breakdown of glucose to pyruvate allows for the generation of energy in the form of ATP and reducing equivalents. In addition, glucose can be diverted into biosynthetic pathways for anabolic metabolism and for the process of metabolizing glucose to confer signaling functionality by, for example, coupling to the generation of reactive oxygen species and the mediation of chromatin state (Chandel, 2015).

Given the numerous biological functions that are conferred through glycolysis, it is reasonable to assume that glucose metabolism would exist in a number of distinct phenotypically defined states. For example, aerobic glycolysis or the Warburg Effect (WE) (increased glucose uptake and incomplete oxidation to lactate in the presence of oxygen) is thought to constitute a switch from the more common form of metabolism observed in differentiated cells involving fully oxidative glycolysis (DeRisi et al., 1997; Vander Heiden et al., 2009). This altered form of glucose metabolism has been thought to result in differential functionality including variations in anabolic metabolism. However, recent studies have questioned whether a switch from mitochondrial metabolism occurs during the WE (Sellers et al., 2015) which is consistent with original observations (Crabtree, 1929; Warburg et al., 1927). Furthermore, other work has challenged whether the WE has any specific role in anabolic metabolism (DeBerardinis et al., 2007; Hosios et al., 2016). Indeed, studies have defined metabolic requirements of

cancer to exist in two states - dependent or independent on glycolysis (Boudreau et al., 2016; Pusapati et al., 2016). If this is the case, then the WE would not be biologically distinct from other aspects of glucose metabolism. Thus, there is a surprising lack of clarity in the current literature as to whether the WE is a biologically defined state (Liberti and Locasale, 2016).

Metabolic control analysis has indicated that GAPDH exerts more control over glycolysis during the WE (Bakker et al., 2000; Shestov et al., 2014) and thus partial inhibition of GAPDH has a large differential effect on reducing glycolysis in WE conditions (Liberti et al., 2017). As a proof of concept, a natural product, koningic acid (KA), was shown to be selective for GAPDH as expression of a resistant allele of GAPDH ablates all changes in metabolism induced by the compound (Kumagai et al., 2008; Liberti et al., 2017; Watanabe et al., 1993). The compound is also selective against the fitness of cells specifically undergoing aerobic glycolysis (Kornberg et al., 2018; Liberti et al., 2017). Furthermore, numerous studies have suggested that targeting of GAPDH may be beneficial (Ganapathy-Kanniappan et al., 2009; Louie et al., 2016; Yun et al., 2015), in retrospect through partial inhibition of GAPDH during aerobic glycolysis. Thus, KA is a valuable probe to study the WE and to determine whether it has any specific biological function outside of glycolysis.

In this study, I sought to address the question of whether the WE can be phenotypically defined apart from glycolysis and fully oxidative glucose metabolism. Using a series of pharmacological and metabolomic approaches, I provide evidence that glucose metabolism exists in a number of defined metabolic states. Using acquired

resistance to GAPDH inhibition as a model and KA as a tool, I show that cells can evolve loss of the WE but continue to conduct and remain dependent on glycolysis. Consequently, these cells that have a selection pressure to lose the WE display widespread changes in metabolism downstream of glycolysis changes including a marked rewiring of fatty acid metabolism. Thus, my study provides evidence that the WE can be a biologically distinct form of glucose metabolism.

3.4 Results

3.4.1 GAPDH inhibition leads to different outcomes from targeting glucose uptake

I first sought to determine whether disrupting GAPDH activity results in different outcomes from other perturbations to glycolysis. Since GAPDH has differential rate control in cells undergoing the WE (i.e. high glucose uptake and lactate secretion) (Liberti et al., 2017), I used a high WE cell line, BT-549, and compared inhibition of GAPDH with KA to inhibition of glucose uptake and deprivation of glucose from the culture media (Figure 3.1A). First, I measured the IC_{50} of E11, a validated, highly potent inhibitor of GLUT-1 and thus glucose uptake (Liu et al., 2017) (Figure A2.S1A), and compared cell viability of BT-549 treated with doses of KA above and below the known IC_{50} (Liberti et al., 2017) and/or E11. I found that co-treatment of KA and E11 caused more significant decreases in cell viability than with either compound alone (Figure 3.1B). These data suggest that GAPDH inhibition is different from inhibition of GLUT-1.

I further found significant changes between KA treated cells and cells cultured in glucose-deprived media (Figure 3.1C). To assess these differences, I used liquid

chromatography coupled to high resolution mass spectrometry (LC-HRMS) based metabolomics, which revealed gross differences in global metabolism when comparing KA treated cells to glucose-deprived cells (Figure 3.1D). An analysis of glycolysis indicated an accumulation of glycolytic intermediates upstream and depletion of those downstream of GAPDH in cells treated with KA, whereas glucose-deprived conditions revealed an overall depletion of metabolites throughout glycolysis (Figure 3.1E). Thus, cells treated with KA respond differently from cells deprived of glucose or targeted with GLUT-1 inhibition. These data provide rationale that glycolysis could exist in multiple states given that the global metabolic and phenotypic responses to disruption of the pathway at different steps are different.

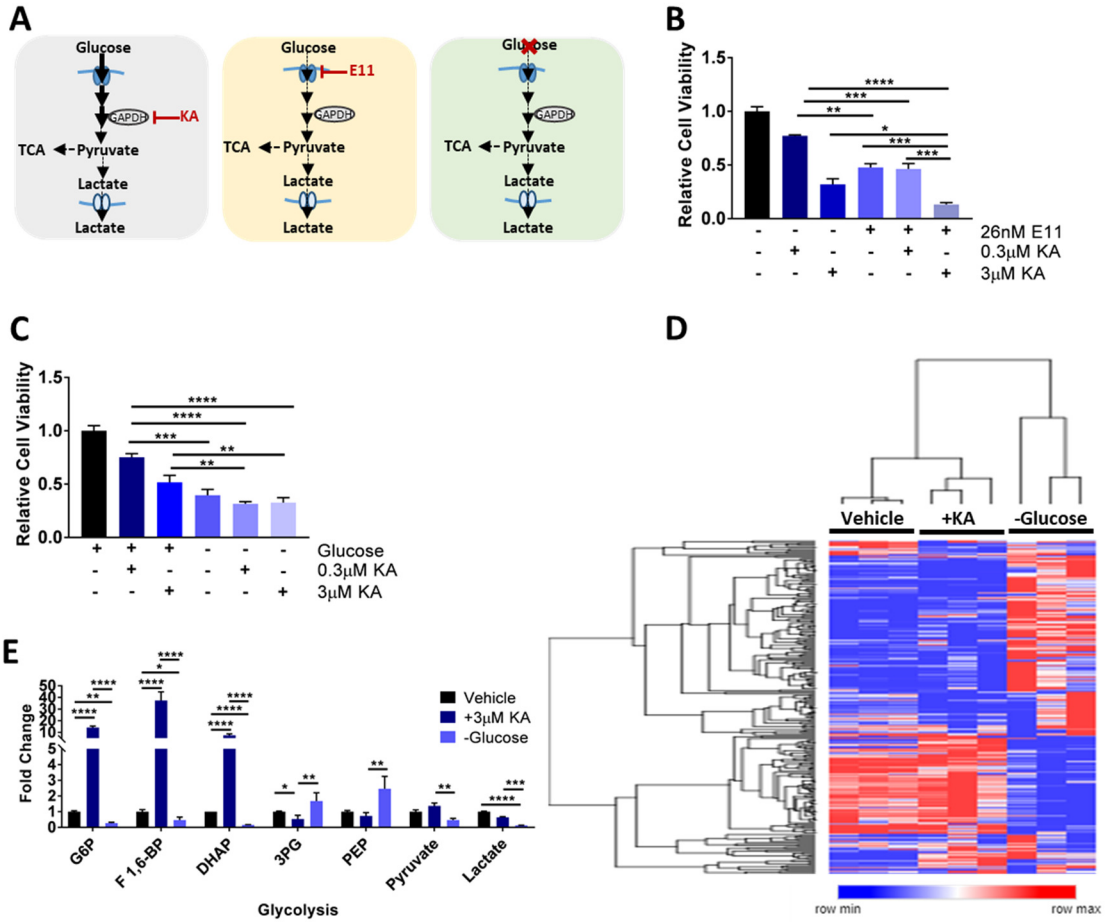

Figure 3.1. GAPDH inhibition leads to different outcomes from targeting glucose uptake.
(A) Schematic representing the comparison of KA treatment to glucose transporter-1 (GLUT-1) inhibition with E11 or deprivation of glucose from the growth media. **(B)** Cell viability of BT-549 breast cancer cells treated with E11 (26nM) with or without KA (0.3μM or 3μM) after 24 hours. *p<0.05, **p<0.01, ***p<0.001, ****p<0.0001 as determined by One-Way ANOVA. **(C)** Cell viability of BT-549 breast cancer cells cultured in complete or glucose restricted media and treated with or without KA (0.3μM or 3μM) after 24 hours. *p<0.05, **p<0.01, ***p<0.001, ****p<0.0001 as determined by One-Way ANOVA. **(D)** Hierarchical clustered heatmap quantile normalized of BT-549 cells with condition annotations of global metabolic responses to vehicle, 3μM KA, or glucose restricted conditions for 6 hours. **(E)** BT-549 glycolysis profile for vehicle, KA, or glucose restricted conditions for 6 hours.
G6P, glucose-6-phosphate; F 1,6-BP, fructose 1,6-bisphosphate; DHAP, dihydroxyacetone phosphate; 3PG, 3-phosphoglycerate; PEP, phosphoenolpyruvate.
All data are represented as mean ± SEM from n=3 biological replicates.
*p<0.05, **p<0.01, ***p<0.001, ****p<0.0001 as determined by Two-Way ANOVA unless otherwise indicated.

3.4.2 Cells evolve resistance to GAPDH inhibition independent of drug metabolism

To investigate the possibility that glycolysis could exist in different biological states, I hypothesized that cells could transition from the WE to another state of glucose metabolism when faced with a selective pressure against maintaining glycolysis in a certain state. Given that KA was previously shown to be selectively toxic to cells undergoing the WE, I suspected that it could be a useful tool to investigate this concept. I cultured BT-549 cells with incrementally increasing concentrations of KA and monitored their growth rate over a period of 20 weeks (Figures 3.2A and 3.2B). Once cells developed resistance to 3μM KA, three clonal cell populations were isolated and maintained in 3μM KA for the remainder of the study (BT-549(R)1-3) (Figure 3.2C). IC_{50} values for KA in each of these clones were found to be greater than 200μM compared to the parental cells that exhibited an IC_{50} of ~1μM KA (Figure 3.2D).

For this system to be an effective model for evolving a transition out of the WE, it was necessary to first determine whether resistance to KA was occurring due to mechanisms outside of cellular metabolism. There are several known pharmacological mechanisms that are commonly implicated in drug resistance which include alterations in drug metabolism and target disengagement (Holohan et al., 2013). To determine whether resistance to KA developed due to altered drug metabolism such as a difference in drug efflux, I used LC-HRMS to measure intracellular concentrations of KA in BT-549 sensitive and acquired resistant cells as well as in MCF-7 KA-intrinsic resistant cells (Figure 3.2E). Intracellular concentrations of KA in BT-549 acquired resistant cells remained consistent with concentrations detected in BT-549 parental and MCF-7 intrinsic

resistant cells that were treated with 3μM KA (Figures 3.2F and A2.S2A).

To determine whether KA was still engaging its target, the catalytic site of GAPDH (Endo et al., 1985; Sakai et al., 1988), I carried out a GAPDH activity assay in the presence or absence of KA and found that KA maintains target engagement through decreasing GAPDH activity in BT-549 acquired resistant cells comparable to BT-549 parental cells (Figures 3.2G, A2.S2B and A2.S2C) and MCF-7 cells (Figure A2.S2D). Together, these data suggest that acquired resistant cells retain normal KA drug metabolism properties with continued target engagement at the active site of GAPDH. Thus, independent of drug pharmacology, biological mechanisms related to glucose metabolism may underlie the resistance to GAPDH inhibition.

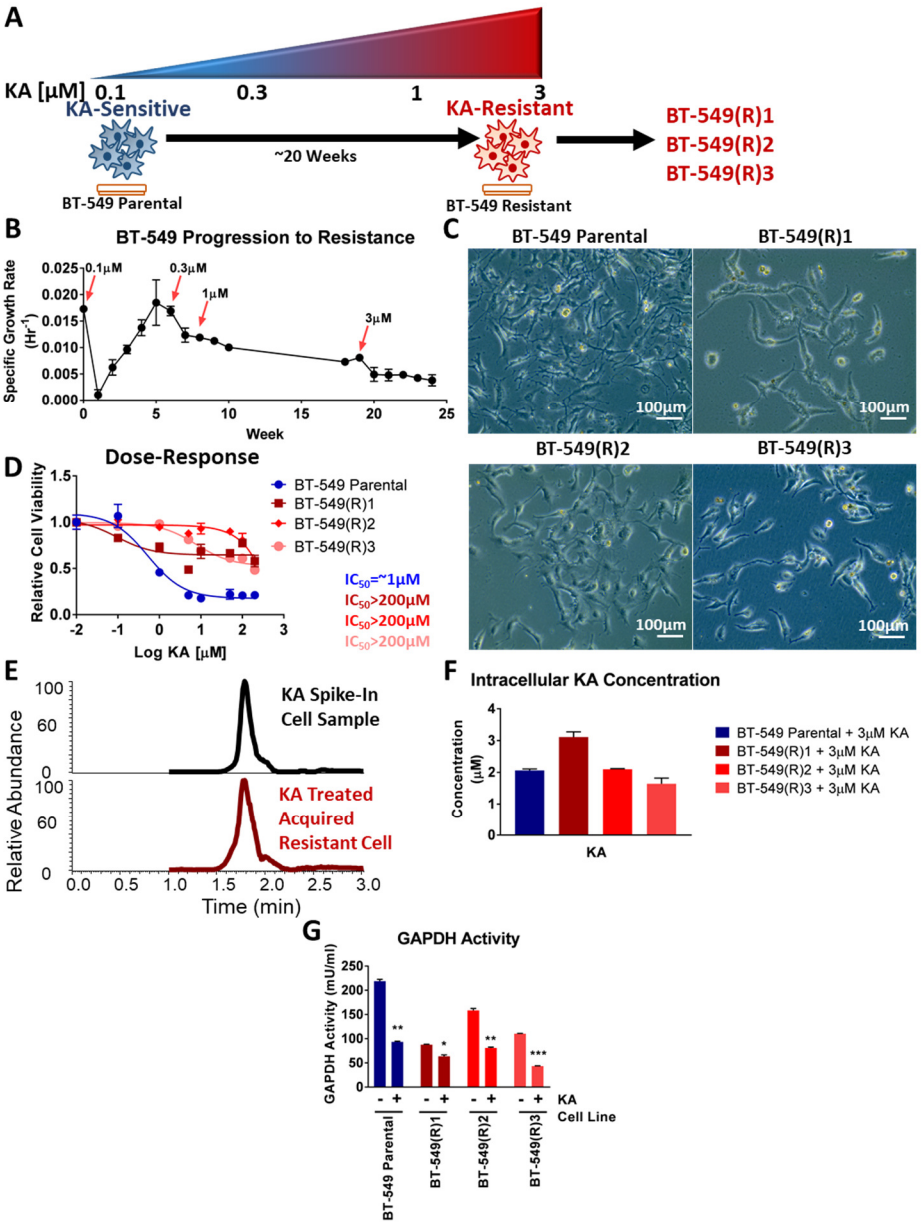

Figure 3.2 Cells evolve resistance to GAPDH inhibition independent of drug metabolism.
(A) Schematic representing progression to acquired resistance model of BT-549 cells. After 20 weeks of incrementally increasing doses of KA clonal populations of acquired resistant cells were isolated and maintained in 3µM KA for the duration of the study. **(B)** Recorded growth rates of BT-549 cells during the 20-week period of progression to acquired resistance. **(C)** Representative images of BT-549 parental (top left) and 3 clonal acquired resistant cells (top right, bottom row). **(D)** Cell viability of BT-549 parental and acquired resistant cells treated with 0-200µM KA and reported IC_{50} values. **(E)** Mass spectra of KA in a spike-in sample and KA treated acquired resistant cell using liquid chromatography-mass spectrometry (LC-MS) with a representative sample. **(F)** Intracellular KA concentrations from BT-549 parental and acquired resistant cells treated with 3µM KA. **(G)** Relative GAPDH activity in BT-549 parental and acquired resistant cells in response to vehicle or 3µM KA (n=2).
All data are represented as mean ± SEM from n=3 biological replicates unless otherwise indicated.
*p<0.05, **p<0.01, ***p<0.001, ****p<0.0001 as determined by multiple t-tests.

3.4.3 Acquired resistant cells remain dependent on glycolysis but lose the Warburg effect

Given that these cells evolved resistance to the glycolytic enzyme GAPDH, I sought to determine whether they continued to depend on glycolysis for survival. I treated BT-549 acquired resistant cells with KA and found that resistant cells still undergo glycolysis marked by increases in fructose 1,6-bisphosphate (F 1,6-BP) compared to BT-549 parental, which are indicative of slower rates of glycolysis (Shestov et al., 2014; van Heerden et al., 2014) and decreases in lactate levels, suggestive of a lower WE (Figure 3.3A).

Given the low lactate levels in the acquired resistant cells, I next sought to examine lactate production from glucose using uniformly labeled (U-^{13}C)-glucose in BT-549 parental and acquired resistant cells. I found decreased lactate production in the acquired resistant cells compared to untreated parental cells at levels comparable to the lactate production observed in the parental cells treated with 3μM KA (Figure 3.3B). Furthermore, I also measured excreted lactate from cells in spent media from 0-6 hours and found significantly less excreted lactate from BT-549 acquired resistant cells compared to parental cells treated with either vehicle or KA, with a similar finding after 24 hours (Figures 3.3C, 3.3D, A2.S3A). In addition, the decreases in lactate levels were not immediately reversible upon removal of KA (Figure A2.S3B). Thus, acquired resistant cells evolved a loss of the WE.

Since acquired resistant cells no longer undergo the WE, I asked whether they remained dependent on glucose uptake. I treated the acquired resistant cells with E11

and/or KA and determined cell viability. While these cells remained resistant to KA as expected, I surprisingly observed differences in sensitivity upon treatment with E11 in combination with KA (Figure 3.3E). To further investigate this differential dependence on glycolysis, I studied the response to glucose deprivation. After 24 hours of culture in glucose-deprived growth media and KA, I found that the viability of BT-549 acquired resistant cells decreased compared to cells cultured in full growth media and maintained in KA (Figure 3.3F). In addition, metabolite profiling of BT-549 acquired resistant cells in glucose-deprived growth media compared to those maintained in 3μM KA revealed global differences in overall metabolic levels (Figure 3.3G). Together, these data indicate that BT-549 acquired resistant cells remain dependent on glycolysis for survival but no longer exhibit or require the WE.

I further found that acquired resistant cells displayed decreased carbon contribution from glucose through glycolysis, the pentose phosphate pathway, and the citric acid (TCA) cycle (Figures A2.S3C-A2.S3G). Taken together, these data further clarify the existence of multiple states of glucose metabolism.

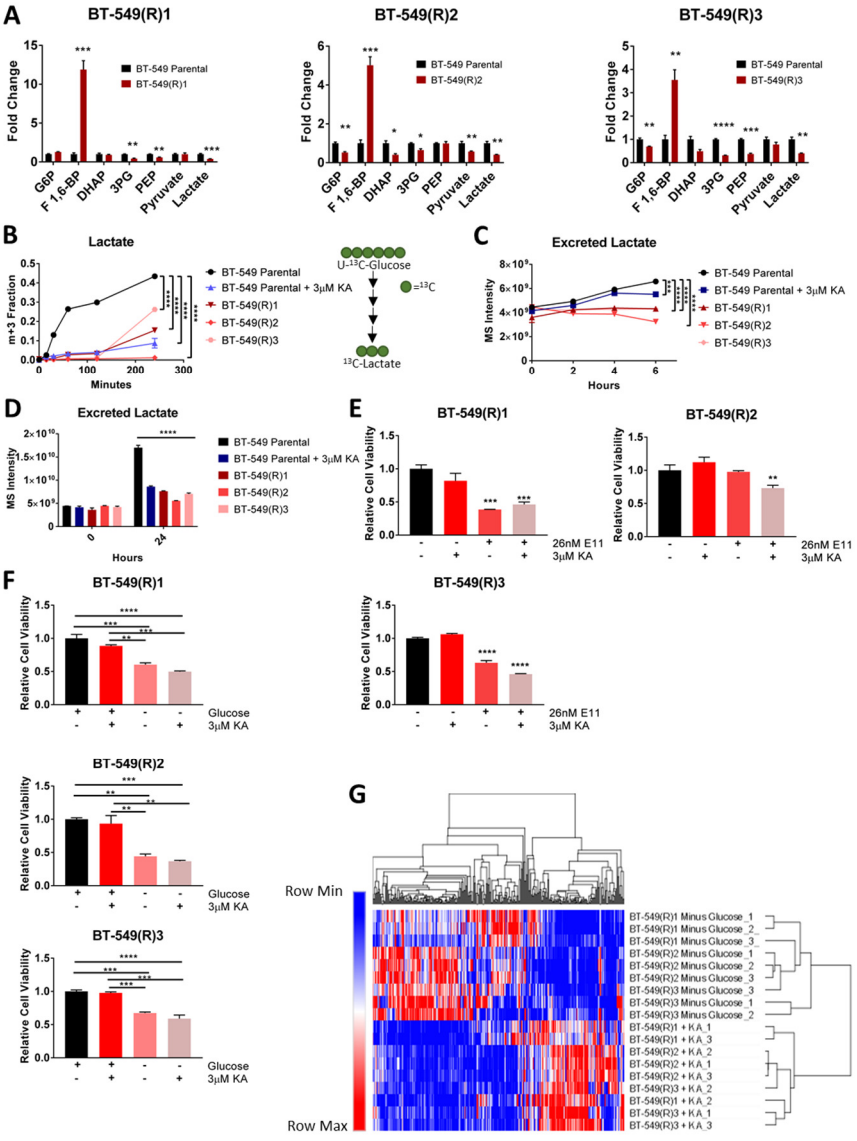

Figure 3.3. Acquired resistant cells remain dependent on glycolysis but lose the Warburg Effect.
(A) Glycolytic metabolite levels. *p<0.05, **p<0.01, ***p<0.001, ****p<0.0001 as determined by multiple t-tests. **(B)** ^{13}C-lactate from (U-^{13}C)-glucose in BT-549 parental treated with vehicle or 3μM KA and acquired resistant cells for 0-4 hours. **(C)** Excreted lactate detected in media from 0-4 hours. **(D)** Excreted lactate detected in media after 24 hours. **(E)** Cell viability of BT-549 acquired resistant cancer cells treated with E11 (26nM) with or without KA (3μM) after 24 hours. *p<0.05, **p<0.01, ***p<0.001, ****p<0.0001 as determined by One-Way ANOVA. **(F)** Cell viability of BT-549 acquired resistant cancer cells cultured in complete or glucose restricted media and treated with or without KA (3μM) after 24 hours. *p<0.05, **p<0.01, ***p<0.001, ****p<0.0001 as determined by One-Way ANOVA. **(G)** Hierarchical clustered heatmap quantile normalized of BT-549 cells with condition annotations of global metabolic responses to vehicle, 3μM KA, or glucose restricted conditions for 6 hours.
G6P, glucose-6-phosphate; F 1,6-BP, fructose 1,6-bisphosphate; DHAP, dihydroxyacetone phosphate; 3PG, 3-phosphoglycerate; PEP, phosphoenolpyruvate.
All data are represented as mean ± SEM from n=3 biological replicates.
*p<0.05, **p<0.01, ***p<0.001, ****p<0.0001 as determined by Two-Way ANOVA unless otherwise indicated.

3.4.4 Changes in fatty acid metabolism emerge as a functional output of evolved resistance to KA.

My data thus far indicate a transition from the utilization of the WE to loss of the WE in acquired resistant cells to KA. To understand the temporal dynamics of metabolism that result with the observed change in the state of glucose metabolism, I extracted metabolites from cells at different times over the 20-week time course during progression to resistance (Figure 3.4A). Metabolite profiling revealed global differences with glycolysis most prominently affected in the parental cells, and changes to fatty acid, one-carbon and nucleotide metabolism most apparent in acquired resistant cells (Figures 4B and 4C). Over half of the common changes in each of the clones relative to the parental cells were related to fatty acid metabolism (Figure 3.4D). I found increased sensitivity to cerulenin, a fatty acid synthase inhibitor that inhibits fatty acid oxidation by increasing malonyl-CoA levels (Hu et al., 2003; Loftus et al., 2000; Thupari et al., 2001), in the acquired resistant cells compared to the parental cells and also found no significant change in MCF-7 cells (Figures A2.S4A-A2.S4C). Additionally, the acquired resistant cells treated with cerulenin exhibited a differential metabolic response (Figures 3.5A and A2.S4D). Next, I asked whether cerulenin differentially affected acyl-carnitine levels, signatures of fatty acid metabolism (Gao et al., 2018; Koves et al., 2008), in BT-549 acquired resistant cells compared to BT-549 parental cells. While I found that BT-549 parental cells exhibited few changes in acyl-carnitine levels upon co-treatment with KA and cerulenin, I found that when acquired resistant cells are maintained in KA, acyl-carnitines are elevated but upon co-treatment with cerulenin many of them significantly

decrease (Figures 3.5B and A2.S4E).

Since the biguanide metformin has been shown to decrease fatty acid and mitochondrial metabolism (Owen et al., 2000), I asked whether metformin displayed similar effects to cerulenin. Using the measured IC_{50} of metformin in BT-549 parental cells (Figure A2.S4F), my collaborator Anna Allen and I co-treated parental and acquired resistant cells with metformin and KA, which revealed decreases in cell viability of both BT-549 sensitive cells and acquired resistant cells, albeit to a lesser extent in BT-549(R)2 cells and no significant response in the non-glycolytic MCF-7 cells (Figures A2.S4G and S4H). I also found that upon co-treatment with KA and metformin compared to KA alone, acyl-carnitines were to a larger extent significantly decreased in acquired resistant cells than in parental cells (Figures 3.5C-3.5D and A2.S4I-A2.S4J), thus confirming that distinct metabolic phenotypes related to fatty acid metabolism occur downstream of the differences in glycolysis.

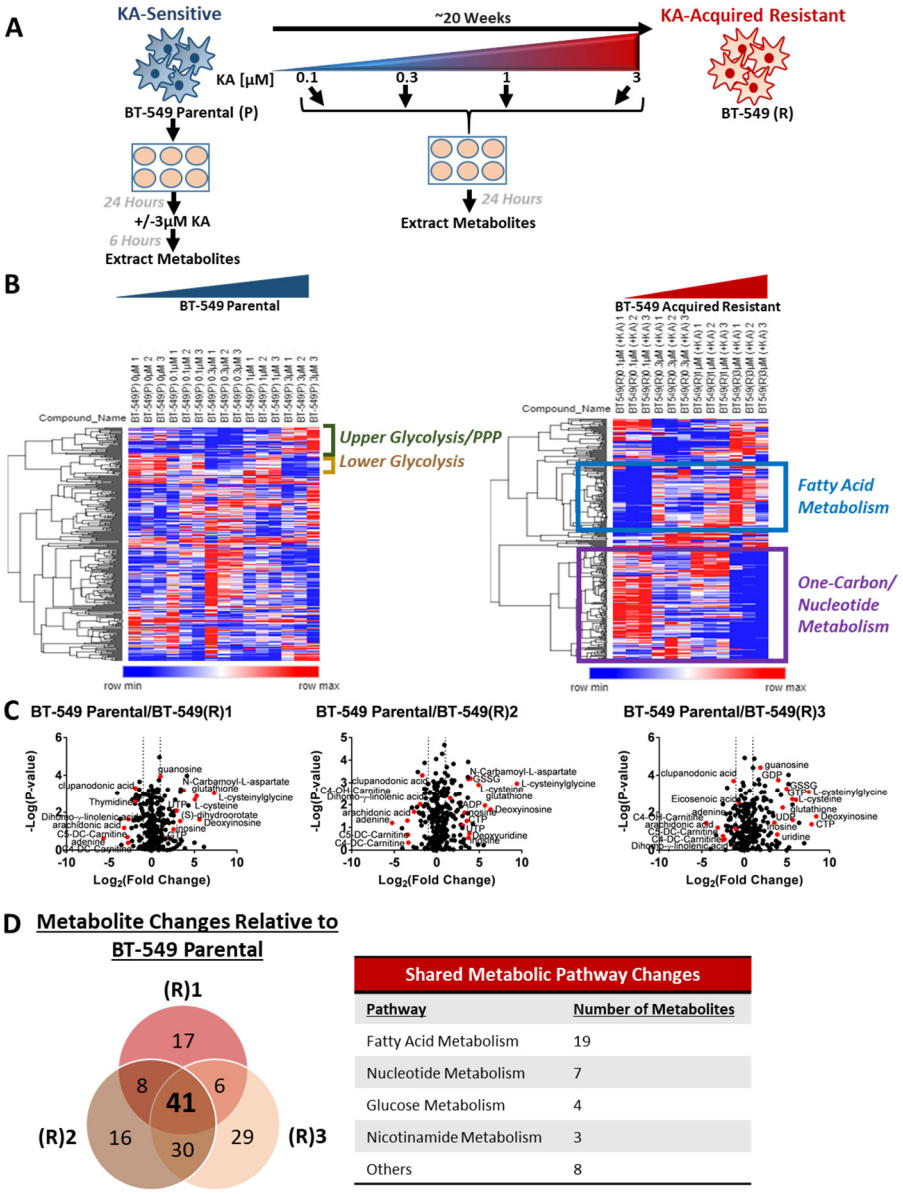

Shared Metabolic Pathway Changes	
Pathway	**Number of Metabolites**
Fatty Acid Metabolism	19
Nucleotide Metabolism	7
Glucose Metabolism	4
Nicotinamide Metabolism	3
Others	8

Figure 3.4. Changes in fatty acid metabolism emerge as a functional output of evolved resistance to KA.
(A) Schematic of experimental setup for metabolomics during evolution to acquired resistance to KA. **(B)** Hierarchical clustered heatmap quantile normalized of 0-3μM KA dose-response in BT-549 parental and 0-3μM evolved resistance in BT-549 acquired resistant cells with pathways denoted. **(C)** Volcano plots showing metabolite profiles of BT-549 acquired resistant cells maintained in 3μM KA compared to BT-549 parental cells treated with vehicle. Log_2 fold change versus $-log_{10}$ p-value. Dotted lines along x-axis represent ± $log_2(1)$ fold change and dotted line along y-axis represents $-log_{10}(0.05)$. Metabolites ± $log_2(1)$ fold change shown as red points with metabolite names denoted. All other metabolites are black points. **(D)** Venn diagram indicating the overlap of metabolic changes among KA-resistant clones based on average ±$log_2(1)$ fold changes compared to BT-549 parental cells treated with vehicle.
G6P, glucose-6-phosphate; F 1,6-BP, fructose 1,6-bisphosphate; DHAP, dihydroxyacetone phosphate; 3PG, 3-phosphoglycerate; PEP, phosphoenolpyruvate.
All data are represented as mean ± SEM from n=3 biological replicates.
*p<0.05, **p<0.01, ***p<0.001, ****p<0.0001 as determined by Two-Way ANOVA.

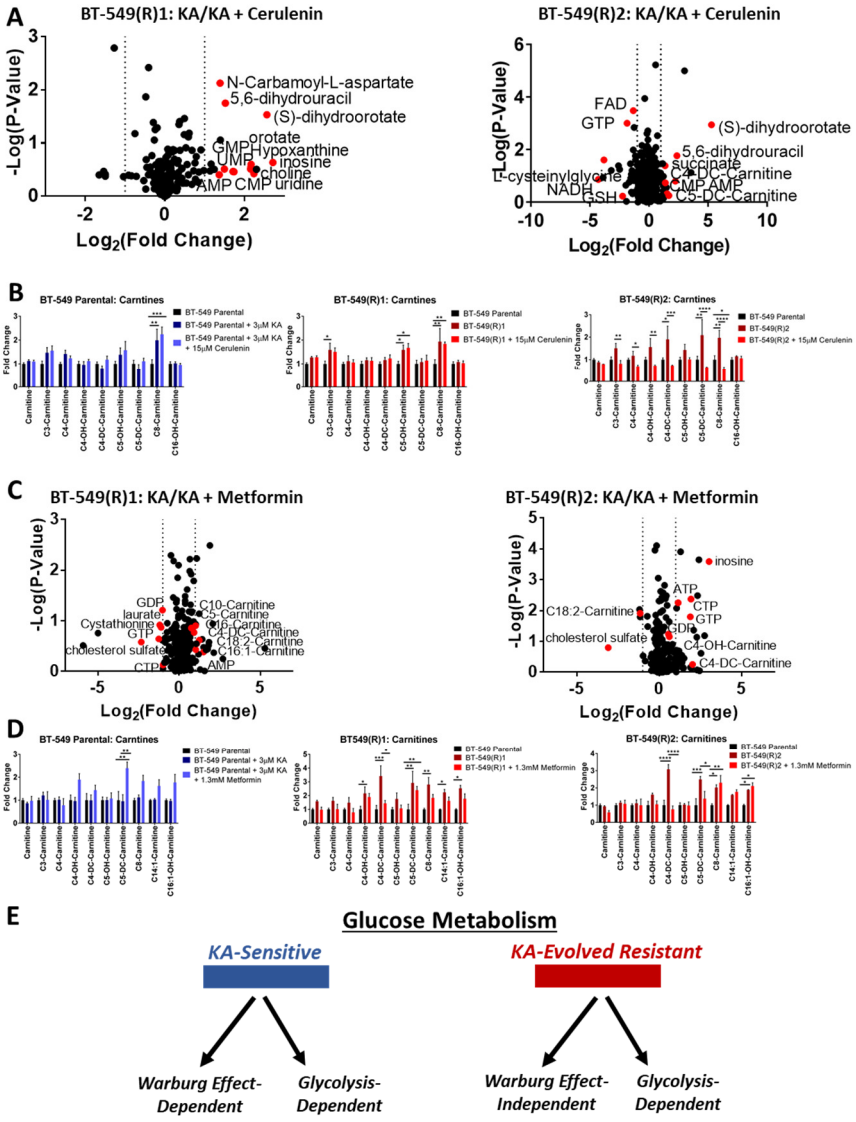

Figure 3.5. Changes in fatty acid metabolism occur downstream of differences in glycolysis in acquired resistance to KA.

(A) Volcano plots showing metabolite profiles of BT-549 acquired resistant (R)1 and (R)2 cells maintained in KA (3μM) with or without cerulenin (15μM). Log_2 fold change versus $-log_{10}$ p-value. Dotted lines along x-axis represent ± $log_2(1)$ fold change and dotted line along y-axis represents $-log_{10}(0.05)$. Metabolites ± $log_2(1)$ fold change shown as red points with metabolite names denoted. All other metabolites are black points. **(B)** Acyl-carnitine levels in BT-549 parental and acquired resistant cells maintained in KA (3μM) and treated with or without cerulenin (15μM) for 6 hours. **(C)** Volcano plots showing metabolic profiles of BT-549 acquired resistant (R)1 and (R)2 cells maintained in KA (3μM) with or without metformin (1.3mM) as in (A). **(D)** Acyl-carnitine levels in BT-549 parental and acquired resistant cells maintained in KA (3μM) and treated with or without metformin (1.3mM) for 6 hours. **(E)** Schematic representing different phenotypically-defined glucose metabolism states.

GMP, guanosine monophosphate; UMP, uridine monophosphate; AMP, adenosine monophosphate; CMP, cytidine monophosphate; FAD, flavin adenine dinucleotide; NADH, nicotinamide adenine dinucleotide; GSH, reduced glutathione; CTP, cytidine triphosphate; SAH, s-adenosyl-l-homocysteine;

All data are represented as mean ± SEM from n=3 biological replicates.

*p<0.05, **p<0.01, ***p<0.001, ****p<0.0001 as determined by Two-Way ANOVA.

3.5 Discussion

Previous work has shown that GAPDH has a specific regulatory role in aerobic glycolysis (Kornberg et al., 2018; Liberti et al., 2017; Shestov et al., 2014; Yun et al., 2015). My current study extends from this understanding to show that evolved resistance to a specific GAPDH inhibitor, KA, loses the WE, thus demonstrating that glucose metabolism can exist in different states. In particular, I demonstrate that cells can exist in at least two separate states of glucose metabolism including WE-dependent and glycolysis-dependent or WE-independent and glycolysis-dependent (Figure 3.5E). Glycolysis has been thoroughly studied using models that ablate the expression of glycolytic enzymes or completely block the pathway (Christofk et al., 2008; Israelsen et al., 2013; Patra et al., 2013; Pusapati et al., 2016) which reduces overall or eliminates altogether the activity of glycolysis. My model of evolved resistance to KA is useful to study glucose metabolism regulation without complete pathway inhibition. Instead, I was able to place a selection pressure against the fitness of using the WE during proliferation. Moreover, using metabolomics, I further demonstrate that the resulting pressure to lose the WE retains a requirement for glycolysis but alters several metabolic outputs in central carbon metabolism. For example, fatty acid metabolism is upregulated and selectively required in cells. Furthermore, the temporal dynamics of metabolic alterations could be captured from early to late timepoints of this evolution. In physiology, such as within a tumor microenvironment, it is likely that this range of metabolic plasticity allows for rapid adaptation to a dynamic environment.

With my system of acquired resistance to KA, I was able to study glycolysis under

different configurations of metabolic activity as cells transition from the WE to another glycolytic state. I provide clear evidence for a distinction between the WE and glucose metabolism. Interestingly, previous literature and related drug development efforts have worked under the model that glycolysis functions as a binary switch (i.e. glucose dependent or independent) (Boudreau et al., 2016; Pusapati et al., 2016). In these cases, glucose dependence is identical to aerobic glycolysis. My findings show that although KA-resistant cells no longer undergo the WE, they undergo glycolysis with less lactate production and remain dependent on glucose uptake. Thus, my data indicate that glucose metabolism exists functionally in a set of states. By evolving resistance to GAPDH inhibition with KA, I show that WE-undergoing cells that lose aerobic glycolysis do not simply switch to increased oxidative phosphorylation but maintain glucose metabolism in a separate biological state.

While aerobic glycolysis has been extensively studied over the years, whether the WE has a function aside from glycolysis has been challenged (Faubert et al., 2017; Hosios et al., 2016). My findings provide evidence for the WE existing as a biologically functional state of glucose metabolism. From a therapeutic perspective, elucidating the WE as a distinct phenomenon from glucose metabolism provides rationale for continued efforts to target the WE while keeping all other forms of glycolysis intact. Such efforts are underway including various studies particularly focusing on the targeting of GAPDH (Kornberg et al., 2018; Louie et al., 2016; Yun et al., 2015). Previous studies already indicate the feasibility and tolerability of targeting GAPDH therapeutically (Kornberg et al., 2018; Liberti et al., 2017). Although this study by itself does not resolve whether the

WE is in fact driving cancer or whether it is a metabolic consequence of cancer progression, my study does confirm that the WE is in fact a real biological phenomenon with different biological and metabolic properties.

3.6 Experimental Procedures

3.6.1 Cell culture

BT-549 and MCF-7 cells were cultured in full media containing RPMI-1640 (Gibco), 10% heat-inactivated fetal bovine serum (FBS), 100U/ml penicillin and 100µg/ml streptomycin. BT-549 and MCF-7 cells were obtained from the American Tissue Culture Collection (ATCC). Koningic acid (KA)-resistant BT-549 cells were cultured and maintained in full media containing RPMI-1640, 10% heat-inactivated FBS, 100U/ml penicillin,100µg/ml streptomycin, and 3µM KA (isolated in-house) (Liberti et al., 2017). Cells were cultured in a 37ºC, 5% CO_2 atmosphere.

3.6.2 Time to progression to resistance assay

Cells were allowed to progress to resistance as previously described (Singleton et al., 2017). To allow cells to acquire resistance to KA, BT-549 breast cancer cells were first seeded in triplicate in 15cm plates at $3x10^6$ cells per plate in normal media. After 24 hr, the normal growth media was replaced with fresh media at the indicated KA treatment. After seven days, cells were lifted with 0.25% trypsin (Cellgro) and counted using Moxi Z mini automated cell counter. All cells up to $1x10^6$ cells were centrifuged at 1,500 rpm for 3 min and resuspended in 10ml of media and plated into a 15 cm plate with fresh treatment. For each measurement, once cell number reached $3x10^6$ cells two weeks in a

row, the dose was increased as indicated. This procedure was repeated weekly for 20 weeks. Weekly growth rates (μ) were calculated from the number of cells plated the previous week (N_0) and the number of cells counted on the current week (N) according to the formula

$$\ln N = \ln N_0 + \mu t$$

where t is elapsed time in hr. These growth rates were then used to project total cell number as if no cells had been discarded.

3.6.3 Cell viability assays

For all cell lines, $5x10^4$ cells/well were seeded in triplicate in a 96-well plate and allowed to adhere for 24 hr. The following day, vehicle or treatment was added to each well at the respective concentrations. After 24 hr, the media was aspirated and replaced with 100μL phenol-red free RPMI-1640 and 12mM 3-[4,5-Dimethylthiazol-2-yl]-2,5-diphenyltetrazolium (MTT) (Thermo Fisher Scientific, #M6494) was added to the cells. After 4 hr, the media containing MTT was aspirated and 50 μL DMSO was added to dissolve the formazan and read at 540nm.

3.6.4 Drug treatments

For all cell lines, IC_{50} values of KA were measured by seeding $5x10^4$ cells/well in triplicate in a 96-well plate and allowed to adhere for 24 hr. The following day, media was changed and concentrations of either vehicle (H_2O or DMSO), KA, E11 (Liu et al., 2017), cerulenin (Sigma-Aldrich, #C2389), or metformin (Santa Cruz Biotechnology, #202000A), were added. After 24 hr, cell viability assays were carried out using MTT as previously described.

3.6.5 Nutrient restriction in media

For all cell lines, $5x10^4$ cells/well were seeded in triplicate with complete RPMI-1640 media in 96-well plates and allowed to adhere for 24 hr. On the following day, the respective treatment media was added in the absence or presence of KA at the indicated treatments. MTT assays were carried out as previously described. Treatment media used was as follows: Minus glucose (-Glucose): RPMI-1640 with glutamine lacking glucose containing 10% dialyzed FBS (D-FBS) (Life Technologies), 100U/ml penicillin, and 100µg/ml streptomycin. Cells were grown at 37ºC with 5% CO_2.

3.6.6 GAPDH activity assay

GAPDH activity assay kit (BioVision, #K680) was used. All cells were seeded at $1x10^6$ cells per 10cm plate with either vehicle or KA. After 24 hr, cells were lysed, NADH standard curve was made, and cells were measured at 450nm in kinetic mode for 60 min at 37ºC according to the manufacturer's instructions.

3.6.7 Microscopy

Cells were seeded at a density of $5x10^3$ cells per well in 6-well plates and allowed to adhere for 24 hours prior to treatment. After 48 hours, images were captured using a Leica DM IL LED microscope equipped with a Leica MC170HD camera at 10x objective using LAS EZ software (Leica). Scale bars = 100µm.

3.6.8 U-^{13}C-glucose stable isotope labeling

Cells were seeded at $3x10^5$ cells/well in a 6-well plate and allowed to adhere for 24 hr. After, cells were treated with either vehicle or KA for 6 hr, then replaced with RPMI-1640 media containing 11mM U^{13}C-glucose (Cambridge Isotope Laboratories,

#CLM-1396) and vehicle or KA for 0-4 hr. Metabolites were then extracted.

3.6.9 Extracellular metabolite excretion measurements

Cells were seeded at $3x10^5$ cells/well in a 6-well plate and allowed to adhere for 24 hr. After, cells were treated with vehicle or KA and 15µl media was collected from 0-4 hr and 24hr. Metabolites were then extracted.

3.6.10 Metabolite extraction

Metabolite extraction and subsequent Liquid Chromatography coupled to High Resolution Mass Spectrometry (LC-HRMS) for polar metabolites of each cell line was carried out using a Q Exactive Plus as previously described (Liu et al., 2014a; Liu et al., 2014b). For culture from adherent cell lines, media was quickly aspirated. Next, 1ml of extraction solvent (80% methanol/water) cooled to -80ºC overnight was added immediately to each well and the plates were then transferred to -80ºC for 15 min. After, the plates were removed, and cells were scraped into the extraction solvent on dry ice. For media extractions, 15µl media was collected at 0-24 hr. Next, 15µl extraction solvent (80% methanol/water) (optima LC-MS grade, Fisher Scientific, methanol, #A456; water, #W6) was added to the media. For absolute quantification of KA in cells, media was quickly aspirated, and cells were washed with 0.9% NaCl before following extraction for culture from adherent cells. 0.7µM KA in water was spiked into extraction solvent before centrifugation. All metabolite extractions were centrifuged at 20,000 *g* at 4ºC for 10 min. Finally, the solvent in each sample was evaporated using a speed vacuum for metabolite analysis. For polar metabolite analysis, the cell metabolite extract was first dissolved in 15µl water, followed by dilution with 15 µl methanol/acetonitrile (1:1 *v/v*) (optima LC-

MS grade, Fisher Scientific, methanol, #A456; acetonitrile, #A955). Samples were centrifuged at 20,000 *g* for 10 min at 4ºC and the supernatants were transferred to LC vials. The injection volume for polar metabolite analysis was 5µl.

3.6.11 Liquid chromatography

An XBridge amide column (100 x 2.1 mm i.d., 3.5µm; Waters) was used on a Dionex (Ultimate 3000 UHPLC) for compound separation at room temperature. Mobile phase A is water with 5mM ammonium acetate, pH 6.9, and mobile phase B is 100% acetonitrile. The gradient is linear as follows: 0 min, 85% B; 1.5 min, 85% B; 5.5 min, 35% B; 10 min, 35% B; 10.5 min, 35% B; 10.6 min, 10% B; 12.5 min, 10% B; 13.5 min, 85% B; and 20 min, 85% B. The flow rate was 0.15 ml/min from 0 to 5.5 min, 0.17 ml/min from 6.9 to 10.5 min, 0.3 ml/min from 10.6 to 17.9 min, and 0.15 ml/min from 18 to 20 min. All solvents are LC-MS grade and purchased from Fisher Scientific.

3.6.12 Mass spectrometry

An XBridge amide column (100 x 2.1 mm i.d., 3.5µm; Waters) was used on a Dionex (Ultimate 3000 UHPLC) for compound separation at room temperature. Mobile phase A is water with 5mM ammonium acetate, pH 6.9, and mobile phase B is 100% acetonitrile. The gradient is linear as follows: 0 min, 85% B; 1.5 min, 85% B; 5.5 min, 35% B; 10 min, 35% B; 10.5 min, 35% B; 10.6 min, 10% B; 12.5 min, 10% B; 13.5 min, 85% B; and 20 min, 85% B. The flow rate was 0.15 ml/min from 0 to 5.5 min, 0.17 ml/min from 6.9 to 10.5 min, 0.3 ml/min from 10.6 to 17.9 min, and 0.15 ml/min from 18 to 20 min. All solvents are LC-MS grade and purchased from Fisher Scientific.

3.6.13 Peak extraction and data analysis

Raw data collected from LC-Q Exactive Plus MS was processed on Sieve 2.0 (Thermo Scientific). Peak alignment and detection were performed according to the protocol described by Thermo Scientific. For a targeted metabolite analysis, the method "peak alignment and frame extraction" was applied. An input file of theoretical *m/z* and detected retention time of 197 known metabolites was used for targeted metabolite analysis with data collected in positive mode, while a separate input file of 262 metabolites was used for negative mode. *m/z* width was set to 10 ppm. The output file including detected *m/z* and relative intensity in different samples was obtained after data processing. If the lowest integrated mass spectrometer signal (MS intensity) was less than 1000 and the highest signal was less than 10,000, then this metabolite was considered below the detection limit and excluded for further data analysis. If the lowest signal was less than 1000, but the highest signal was more than 10,000, then a value of 1000 was imputed for the lowest signals. Mass isotopomer distributions (MID) were calculated and samples were normalized by comparing the ratio of glucose-derived labeled metabolites to unlabeled metabolites within each sample. Quantitation and statistics were calculated using Microsoft Excel and GraphPad Prism 7.0.

3.6.14 Analysis of metabolomics data

GENE-E and Morpheus software were used for hierarchal clustering and heatmap generation (The Broad Institute, https://software.broadinstitute.org/GENE-E/index.html). For hierarchal clustering, spearman correlation parameters were implemented for row and column parameters, with the exception of BT-549 parental and

acquired resistant drug response data, in which hierarchal clustering for row parameters only was used. Quantile normalization was used to normalize the data.

3.6.15 Quantification and statistical analysis

Unless otherwise noted, all error bars were reported ± SEM with n = 3 independent biological measurements and statistical tests resulting in p value computations were computed using a Student's t test two tailed, multiple t-tests, one-way ANOVA. or two-way ANOVA of log transformed data followed by Tukey's multiple comparisons. All statistics were computed using GraphPad Prism 7 (GraphPad, http://www.graphpad.com/scientific-software/prism/).

3.7 References

Bakker, B.M., Westerhoff, H.V., Opperdoes, F.R., and Michels, P.A. (2000). Metabolic control analysis of glycolysis in trypanosomes as an approach to improve selectivity and effectiveness of drugs. Molecular and biochemical parasitology *106*, 1-10.

Bar-Even, A., Flamholz, A., Noor, E., and Milo, R. (2012). Rethinking glycolysis: on the biochemical logic of metabolic pathways. Nat Chem Biol *8*, 509-517.

Boudreau, A., Purkey, H.E., Hitz, A., Robarge, K., Peterson, D., Labadie, S., Kwong, M., Hong, R., Gao, M., Del Nagro, C.*, et al.* (2016). Metabolic plasticity underpins innate and acquired resistance to LDHA inhibition. Nat Chem Biol *12*, 779-786.

Chandel, N.S. (2015). Navigating metabolism.

Christofk, H.R., Vander Heiden, M.G., Harris, M.H., Ramanathan, A., Gerszten, R.E., Wei, R., Fleming, M.D., Schreiber, S.L., and Cantley, L.C. (2008). The M2 splice isoform of pyruvate kinase is important for cancer metabolism and tumour growth. Nature *452*, 230-U274.

Crabtree, H.G. (1929). Observations on the carbohydrate metabolism of tumours. Biochemical journal *23*, 536.

DeBerardinis, R.J., Mancuso, A., Daikhin, E., Nissim, I., Yudkoff, M., Wehrli, S., and Thompson, C.B. (2007). Beyond aerobic glycolysis: Transformed cells can engage in glutamine metabolism that exceeds the requirement for protein and nucleotide synthesis. Proceedings of the National Academy of Sciences of the United States of America *104*, 19345-19350.

DeRisi, J.L., Iyer, V.R., and Brown, P.O. (1997). Exploring the metabolic and genetic control of gene expression on a genomic scale. Science *278*, 680-686.

Endo, A., Hasumi, K., Sakai, K., and Kanbe, T. (1985). Specific inhibition of glyceraldehyde-3-phosphate dehydrogenase by koningic acid (heptelidic acid). The Journal of antibiotics *38*, 920-925.

Faubert, B., Li, K.Y., Cai, L., Hensley, C.T., Kim, J., Zacharias, L.G., Yang, C., Do, Q.N., Doucette, S., Burguete, D.*, et al.* (2017). Lactate Metabolism in Human Lung Tumors. Cell *171*, 358-371 e359.

Ganapathy-Kanniappan, S., Geschwind, J.F.H., Kunjithapatham, R., Buijs, M., Vossen, J.A., Tchernyshyov, I., Cole, R.N., Syed, L.H., Rao, P.P., Ota, S.*, et al.* (2009). Glyceraldehyde-3-phosphate Dehydrogenase (GAPDH) Is Pyruvylated during 3-Bromopyruvate Mediated Cancer Cell Death. Anticancer Research *29*, 4909-4918.

Gao, X., Lee, K., Reid, M.A., Sanderson, S.M., Qiu, C.P., Li, S.Q., Liu, J., and Locasale, J.W. (2018). Serine Availability Influences Mitochondrial Dynamics and Function through Lipid Metabolism. Cell Reports *22*, 3507-3520.

Holohan, C., Van Schaeybroeck, S., Longley, D.B., and Johnston, P.G. (2013). Cancer drug resistance: an evolving paradigm. Nat Rev Cancer *13*, 714-726.

Hosios, A.M., Hecht, V.C., Danai, L.V., Johnson, M.O., Rathmell, J.C., Steinhauser, M.L., Manalis, S.R., and Vander Heiden, M.G. (2016). Amino Acids Rather than Glucose Account for the Majority of Cell Mass in Proliferating Mammalian Cells. Developmental Cell *36*, 540-549.

Hu, Z.Y., Cha, S.H., Chohnan, S., and Lane, M.D. (2003). Hypothalamic malonyl-CoA

as a mediator of feeding behavior. Proceedings of the National Academy of Sciences of the United States of America *100*, 12624-12629.
Israelsen, W.J., Dayton, T.L., Davidson, S.M., Fiske, B.P., Hosios, A.M., Bellinger, G., Li, J., Yu, Y., Sasaki, M., Horner, J.W.*, et al.* (2013). PKM2 isoform-specific deletion reveals a differential requirement for pyruvate kinase in tumor cells. Cell *155*, 397-409.
Kornberg, M.D., Bhargava, P., Kim, P.M., Putluri, V., Snowman, A.M., Putluri, N., Calabresi, P.A., and Snyder, S.H. (2018). Dimethyl fumarate targets GAPDH and aerobic glycolysis to modulate immunity. Science *360*, 449-453.
Koves, T.R., Ussher, J.R., Noland, R.C., Slentz, D., Mosedale, M., Ilkayeva, O., Bain, J., Stevens, R., Dyck, J.R., Newgard, C.B.*, et al.* (2008). Mitochondrial overload and incomplete fatty acid oxidation contribute to skeletal muscle insulin resistance. Cell Metab *7*, 45-56.
Kumagai, S., Narasaki, R., and Hasumi, K. (2008). Glucose-dependent active ATP depletion by koningic acid kills high-glycolytic cells. Biochem Biophys Res Commun *365*, 362-368.
Liberti, M.V., Dai, Z.W., Wardell, S.E., Baccile, J.A., Liu, X.J., Gao, X., Baldi, R., Mehrmohamadi, M., Johnson, M.O., Madhukar, N.S.*, et al.* (2017). A Predictive Model for Selective Targeting of the Warburg Effect through GAPDH Inhibition with a Natural Product. Cell Metabolism *26*, 648-+.
Liberti, M.V., and Locasale, J.W. (2016). The Warburg effect: how does it benefit cancer cells? Trends in biochemical sciences *41*, 211-218.
Liu, J., Jingxin, W., and Guo, Z. (2017). Rapaglutins, novel inhibitors of glut and use thereof, W.I.P. Organization, ed. (The Johns Hopkins University).
Liu, X., Ser, Z., Cluntun, A.A., Mentch, S.J., and Locasale, J.W. (2014a). A strategy for sensitive, large scale quantitative metabolomics. J Vis Exp.
Liu, X., Ser, Z., and Locasale, J.W. (2014b). Development and quantitative evaluation of a high-resolution metabolomics technology. Anal Chem *86*, 2175-2184.
Loftus, T.M., Jaworsky, D.E., Frehywot, G.L., Townsend, C.A., Ronnett, G.V., Lane, M.D., and Kuhajda, F.P. (2000). Reduced food intake and body weight in mice treated with fatty acid synthase inhibitors. Science *288*, 2379-2381.
Louie, S.M., Grossman, E.A., Crawford, L.A., Ding, L., Camarda, R., Huffman, T.R., Miyamoto, D.K., Goga, A., Weerapana, E., and Nomura, D.K. (2016). GSTP1 Is a Driver of Triple-Negative Breast Cancer Cell Metabolism and Pathogenicity. Cell Chemical Biology *23*, 567-578.
Owen, M.R., Doran, E., and Halestrap, A.P. (2000). Evidence that metformin exerts its anti-diabetic effects through inhibition of complex 1 of the mitochondrial respiratory chain. Biochemical Journal *348*, 607-614.
Patra, K.C., Wang, Q., Bhaskar, P.T., Miller, L., Wang, Z., Wheaton, W., Chandel, N., Laakso, M., Muller, W.J., and Allen, E.L. (2013). Hexokinase 2 is required for tumor initiation and maintenance and its systemic deletion is therapeutic in mouse models of cancer. Cancer cell *24*, 213-228.
Pusapati, R.V., Daemen, A., Wilson, C., Sandoval, W., Gao, M., Haley, B., Baudy, A.R., Hatzivassiliou, G., Evangelista, M., and Settleman, J. (2016). mTORC1-Dependent Metabolic Reprogramming Underlies Escape from Glycolysis Addiction in Cancer Cells.

Cancer Cell *29*, 548-562.
Sakai, K., Hasumi, K., and Endo, A. (1988). Inactivation of rabbit muscle glyceraldehyde-3-phosphate dehydrogenase by koningic acid. Biochim Biophys Acta *952*, 297-303.
Sellers, K., Fox, M.P., Bousamra, M., Slone, S.P., Higashi, R.M., Miller, D.M., Wang, Y., Yan, J., Yuneva, M.O., and Deshpande, R. (2015). Pyruvate carboxylase is critical for non–small-cell lung cancer proliferation. The Journal of clinical investigation *125*, 687-698.
Shestov, A.A., Liu, X., Ser, Z., Cluntun, A.A., Hung, Y.P., Huang, L., Kim, D., Le, A., Yellen, G., Albeck, J.G.*, et al.* (2014). Quantitative determinants of aerobic glycolysis identify flux through the enzyme GAPDH as a limiting step. Elife *3*, e03342.
Singleton, K.R., Crawford, L., Tsui, E., Manchester, H.E., Maertens, O., Liu, X.J., Liberti, M.V., Magpusao, A.N., Stein, E.M., Tingley, J.P.*, et al.* (2017). Melanoma Therapeutic Strategies that Select against Resistance by Exploiting MYC-Driven Evolutionary Convergence. Cell Reports *21*, 2796-2812.
Thupari, J.N., Pinn, M.L., and Kuhajda, F.P. (2001). Fatty acid synthase inhibition in human breast cancer cells leads to malonyl-CoA-induced inhibition of fatty acid oxidation and cytotoxicity. Biochem Biophys Res Commun *285*, 217-223.
van Heerden, J.H., Wortel, M.T., Bruggeman, F.J., Heijnen, J.J., Bollen, Y.J., Planque, R., Hulshof, J., O'Toole, T.G., Wahl, S.A., and Teusink, B. (2014). Lost in transition: start-up of glycolysis yields subpopulations of nongrowing cells. Science *343*, 1245114.
Vander Heiden, M.G., Cantley, L.C., and Thompson, C.B. (2009). Understanding the Warburg effect: the metabolic requirements of cell proliferation. Science *324*, 1029-1033.
Warburg, O., Wind, F., and Negelein, E. (1927). The Metabolism of Tumors in the Body. J Gen Physiol *8*, 519-530.
Watanabe, H., Hasumi, K., Fukushima, Y., Sakai, K., and Endo, A. (1993). Cloning of two isozymes of Trichoderma koningii glyceraldehyde-3-phosphate dehydrogenase with different sensitivity to koningic acid. Biochim Biophys Acta *1172*, 43-48.
Yun, J., Mullarky, E., Lu, C., Bosch, K.N., Kavalier, A., Rivera, K., Roper, J., Chio, II, Giannopoulou, E.G., Rago, C.*, et al.* (2015). Vitamin C selectively kills KRAS and BRAF mutant colorectal cancer cells by targeting GAPDH. Science *350*, 1391-1396.

CHAPTER 4: RATIONAL DESIGN OF SELECTIVE ALLOSTERIC INHIBITORS OF PHGDH AND SERINE SYNTHESIS WITH ANTI-TUMOR ACTIVITY[4]

4.1 Background and context

The previous chapter established that multiple states of glucose metabolism exist and that the Warburg Effect is a real biological phenomenon. As mentioned in Chapter 1, the Warburg Effect is involved in various important biosynthesis pathways. One such pathway is the serine biosynthesis pathway, which is important for glycine synthesis for donation into one-carbon metabolism that contributes to amino acid and nucleotide synthesis, as well as redox regulation. 3-phosphoglycerate dehydrogenase (PHGDH) is the rate-limiting enzyme that diverts glucose flux into serine synthesis at the 3-phosphoglycerate (3PG) step. In this chapter, my collaborator Qian Wang developed and validated novel allosteric PHGDH inhibitors and I generated CRISPR-*Cas9* mediated *PHGDH* knockout (KO) cells to demonstrate that the compounds are specific for PHGDH. I show that PHGDH inhibition affects *de novo* serine biosynthesis and metabolism downstream of serine synthesis. This study importantly contributes to our current understanding of how PHGDH is required for tumor growth.

---

[4] This chapter was adapted and modified from published work: Wang, Q.*, Liberti, M.V.*, Liu, P., Deng, X., Liu, Y., Locasale, J.W. and Lai, L., 2017. Rational design of selective allosteric inhibitors of PHGDH and serine synthesis with anti-tumor activity. *Cell Chemical Biology*, *24*(1), pp.55-65. (*denotes equal contribution). Author contributions: Conceptualization, L.L. and Q.W.; Study Design and Data Analysis, Q.W., M.V.L., J.W.L., and L.L.; Allosteric site prediction and virtual screening studies, molecular cloning, mutagenesis, protein expression and purification experiments, enzymatic assays, SPR assays, cell-based assays, and *in vivo* studies, Q.W.; CRISPR/*Cas9* experiments, MTT assays, and breast cancer cell metabolomics, M.V.L.; Chemical synthesis and purity analysis of compounds, P.L., X.D., and Y.L.; Writing, Q.W., M.V.L., J.W.L., and L.L.

4.2 Abstract

Metabolic reprogramming in cancer cells facilitates growth and proliferation. Increased activity of the serine biosynthetic pathway through the enzyme 3-phosphoglycerate dehydrogenase (PHGDH) contributes to tumorigenesis. With a small substrate and a weak binding cofactor (NAD^+), the development of inhibitors for PHGDH remains challenging. Instead of targeting the PHGDH active site, my collaborator Qian Wang computationally identified two potential allosteric sites and virtually screened compounds that can bind to these sites. With subsequent characterization, Qian and I successfully identified PHDGH non-NAD^+ competing allosteric inhibitors that attenuate its enzyme activity, selectively inhibit *de novo* serine synthesis in cancer cells, and reduce tumor growth *in vivo*. Our study not only identifies novel allosteric inhibitors for PHGDH to probe its function and potential as a therapeutic target, but also provides a general strategy for the rational design of small molecule modulators of metabolic enzyme function.

4.3 Introduction

It has long been known that tumor cells exhibit altered glucose metabolism characterized by increased glucose uptake and incomplete oxidation to lactate in the presence of oxygen (Warburg, 1956; Zhao et al., 2016) With the surge of interest in understanding cancer cell metabolism, it is now widely accepted that metabolic rearrangements accompanying malignant transformation also involve numerous other pathway alterations such as the increased flux of the pentose phosphate pathway (PPP), elevated rates of lipid biosynthesis, high glutamine consumption, maintenance of redox homeostasis, and alterations in autophagy (Pavlova and Thompson, 2016). Therefore, targeting the metabolic enzymes in these pathways provides a promising strategy for cancer therapy.

The gene encoding 3-phosphoglycerate dehydrogenase (PHGDH), an enzyme that catalyzes the first committed step of serine biosynthesis, is also involved in metabolic reprogramming in cancer. PHGDH was identified as a focus of recurrent copy number gain across a large set of tumors (Beroukhim et al., 2010). The *PHGDH* gene that is located at chromosome 1p12 showed copy number gain in 16% of all cancers including 40% of melanoma and some triple negative breast cancers (Locasale et al., 2011; Possemato et al., 2011). Cancer cells with *PHGDH* amplifications are sensitive to PHGDH depletion, which indicates that the enzyme is required for the growth of certain tumor cells.

Recent studies have identified different regulatory mechanisms that can activate PHGDH through both transcriptional regulation and changes in its activity via

posttranslational modifications (DeNicola et al., 2015; Ding et al., 2013; Ma et al., 2013; Ou et al., 2015). Additional studies have found several underappreciated functions for *de novo* synthesis of serine and the use of one-carbon metabolism including epigenetic maintenance and NADPH production that is important for biosynthesis and controlling the levels of reactive oxygen species (Fan et al., 2014; Mentch et al., 2015). Together these findings demonstrate that PHGDH is an attractive anti-cancer target, and that designing PHGDH inhibitors may be a fruitful enterprise.

Human PHGDH contains four domains: nucleotide-binding, substrate-binding, regulatory and intervening domains. Currently, only the crystal structure containing the first two domains of PHGDH is available (Turnbull, 2006) (PDB code: 2G76). The substrate-binding pocket of PHGDH is rather small, approximately 100-200 $Å^3$, and the physiological concentration of its cofactor NAD^+ is as high as 0.3 mM (Yamada et al., 2006). These properties likely increase the difficulties of designing substrate-competitive inhibitors. Meanwhile, considering NAD^+ or NADH is a widely used cofactor, which also easily causes the problem of specificity, Dr. Luhua Lai's lab focused on designing allosteric inhibitors for PHGDH that do not compete with the native ligand. Allosteric regulation can be achieved by various effectors, ranging from small molecules to macromolecules (Merdanovic et al., 2013) and can have high specificity, as allosteric binding sites are usually not evolutionarily conserved. Computational methods for rational design of allosteric effectors are emerging (Ma et al., 2013; Wagner et al., 2016) and a number of successful application examples have been reported. For example, using the two-state Go model-based allosteric site prediction method that the Lai lab developed

(Qi et al., 2012), they obtained novel allosteric inhibitors for *Escherichia coli* (*E. coli)* phosphoglycerate dehydrogenase (Wang et al., 2014). Novel enzyme activators were also found using combined computational and experimental approach (Meng et al., 2015), providing an alternative way to control disease-related molecular networks (Pei et al., 2014).

In the present study, Qian first computationally identified two potential allosteric sites in PHGDH and used them to virtually screen a compound library. Qian and I tested selected compounds for their inhibition activities using recombinant enzymes, cancer cell lines, and tumor xenograft models. Two distinct compounds with activity in cells were found, PKUMDL-WQ-2101 and PKUMDL-WQ-2201. I independently confirmed their specificity using CRISPR-*Cas9* gene-targeting of *PHGDH* and metabolomics, while Qian used chemical compound pull-down in cancer cells. Recently, three studies have reported compounds that have activity against PHGDH by using high-throughput experimental screening. One series of PHGDH inhibitors showed activities in enzymatic and cell-based assays, but the binding mechanism, selectivity towards PHGDH, and efficacy *in vivo* were unclear (Mullarky et al., 2016). Another series of inhibitors with bioactivities in enzymatic and cell-based assays, as well as a xenograft model, do not have clear binding sites (Pacold et al., 2016). The third series of inhibitors were found by a fragment screen that binds to the adenine subsite with only millimolar protein binding affinities and no further biological activities were reported (Unterlass et al., 2018). To our knowledge, the present study is the first successful example of using a structure-based approach to discover allosteric inhibitors that directly and specifically target PHGDH.

4.4 Results

4.4.1 Allosteric site prediction and identification of novel allosteric inhibitors

Qian identified two potential allosteric sites, I and II, computationally using a cavity detection algorithm based on defined geometric criteria (Yuan et al., 2011) (Figure 4.1A). Site I is close to the active site and the NAD^+/NADH-cofactor binding site and shares residues Gly 78, Val 79, Asp 80, Asn 81 and Val 82 with the active site. Site II is located in the substrate binding domain. Molecular docking across a large virtual compound library was then conducted (Friesner et al., 2004; Halgren et al., 2004). Ninety-eight compounds were selected and then acquired to test their abilities to regulate PHGDH activity.

Qian then identified two inhibitors, PKUMDL-WQ-2101 in site I and PKUMDL-WQ-2201 in site II (Figure 4.1B), to significantly affect the PHGDH activity in a concentration-dependent manner. She also performed competition experiments, mutagenesis studies, and synergism experiments to find that PKUMDL-WQ-2101 and PKUMDL-WQ-2201 do indeed bind to site I and site II respectively. Together, these experiments confirm the docking results found of each compound in their respective sites and provide rationale for further investigating them as selective allosteric inhibitors of PHGDH.

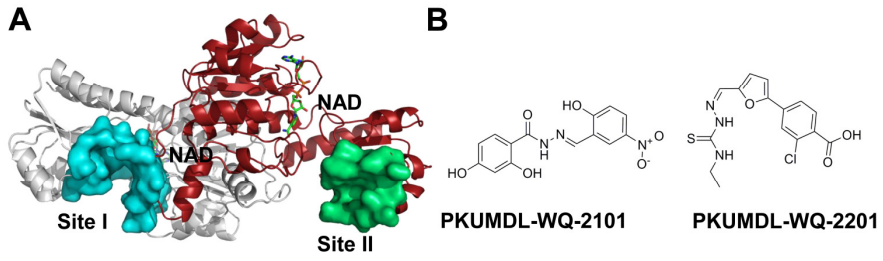

Figure 4.1. Identification of novel allosteric inhibitors of PHGDH.[5]
(A) Potential allosteric sites in PHGDH (PDB code: 2G76). The sites were predicted by the program of CAVITY and illustrated by the surface mode.The cofactor NAD^+ was indicated in sticks. PHGDH forms a dimer in the crystal structure, site I and II exist in each monomer, and only one site I and one site II is shown in the figure for clarity. **(B)** Chemical structures of PHGDH inhibitors.

4.4.2 Cellular effects of PKUMDL-WQ-2101 and PKUMDL-WQ-2201

The effects of the compounds against a panel of cancer cell lines along with one immortalized human breast epithelial cell line were evaluated. PKUMDL-WQ-2101 and PKUMDL-WQ-2201 showed dose-dependent suppression effects on the cell viability at micromolar concentrations, with good selectivity for *PHGDH*-amplified breast cancer cell lines (Figures 4.2A and 4.2B). Qian and I found that the IC_{50} values of PKUMDL-WQ-2101 in the two *PHGDH*-amplified breast cancer cell lines (MDA-MB-468 and HCC70) were 7.70 and 10.8 μM, which were 3- to 4-, 8- to 12-, and 14- to 20-fold more active than its IC_{50}s in *PHGDH*-non-amplified cell lines, MDA-MB-231, ZR-75-1 and MCF-7 cell lines, respectively. We also found that for PKUMDL-WQ-2201, the IC_{50} values were 6.90 μM in MDA-MB-468 and 10.0 μM in HCC70 cell lines, which were 13- to 18-fold more active than that of ZR-75-1. No bioactivities in the other three

[5] Credit goes to Qian Wang.

PHGDH-non-amplified breast cancer cell lines tested were measurable. Meanwhile, PKUMDL-WQ-2101 and PKUMDL-WQ-2201 exerted weak cytotoxic effects on the MCF-10A cell line, which was consistent with previous observations of PHGDH requirements using genetic approaches (Locasale et al., 2011).

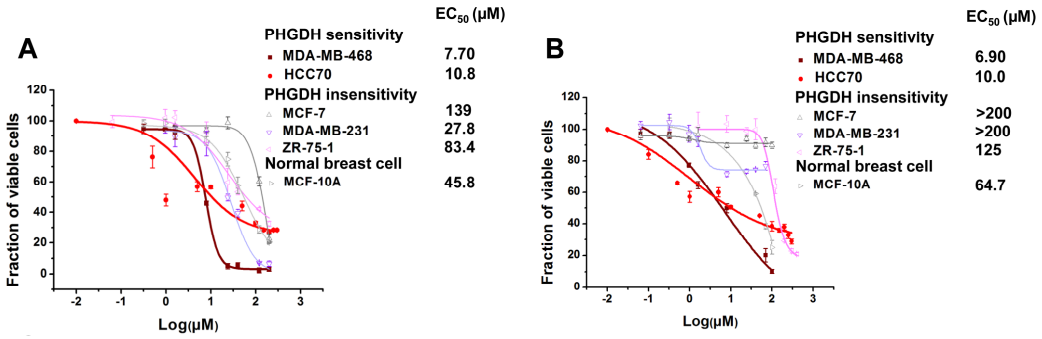

Figure 4.2 Bioactivities of PKUMDL-WQ-2101 and PKUMDL-WQ-2201 in cell based assays.[6]
(A-B) Growth inhibition activity of PKUMDL-WQ-2101 **(A)** and PKUMDL-WQ-2201 **(B)** in MDA-MB-468, HCC70, MCF-7, MDA-MB-231, ZR-75-1 and MCF-10A cells, respectively. Cells were exposed to vehcile or various concentrations of PKUMDL-WQ-2101 for 72h followed by MTT assay. The IC_{50} value of PKUMDL-WQ-2201 for MCF-7 and MDA-MB-231 was larger than 200 μM, so the corresponding dose-response curve was not presented here.

4.4.3 CRISPR-*Cas9*-mediated *PHGDH* KO and PHGDH Inhibition by PKUMDL-WQ-2101 and PKUMDL-WQ-2201

To further evaluate the activity and selectivity of the compounds, I developed a CRISPR-*Cas9*-mediated *PHGDH* gene knockout (KO). I designed a single-guide RNA (sgRNA) with a protospacer adjacent motif (PAM) sequence specifically targeting a coding region in exon 8 of the *PHGDH* gene, predicted to result in a frame shift mutation and loss-of-function (Mali et al., 2013; Shalem et al., 2014) (Figure 4.3A). A clonal

[6] Figure credit goes to Qian Wang.

population of SKOV3 ovarian cancer cells was obtained and able to grow in the absence of *PHGDH*. Complete knockout was confirmed with immunoblotting in reference to a cell line created by targeting a sgRNA against *GFP* (Figure 4.3B). A 6-day growth curve revealed the ability of *PHGDH* KO cells to grow, albeit more slowly than the *GFP* KO control cells ($p<0.01$, two-tailed multiple t-test) (Figure 4.3C). I then evaluated the compounds PKUMDL-WQ-2101 and PKUMDL-WQ-2201 on these cell lines. The *GFP* KO cells exhibited sensitivity to PKUMDL-WQ-2101 (IC_{50}= 37.3 μM) (Figure A3.S1A) and, albeit to a lesser extent to PKUMDL-WQ-2201 (IC_{50} = 291.5.3 μM) (Figure A3.S1B). To further understand the specificity of these compounds, 6-day proliferation assays were carried out in SKOV3 control and *PHGDH* KO cells. *GFP* KO cell growth was significantly suppressed after treatment with PKUMDL-WQ-2101 ($p<10^{-3}$, two-tailed student's t-test) (Figure 4.3D), whereas *PHGDH* KO cells were able to proliferate in the presence of the compound with no significant inhibition (Figure 4.3E). Similarly, albeit to a lesser extent, proliferation in SKOV3 control cells was suppressed after 6 days in the presence of PKUMDL-WQ-2201 ($p<0.05$, two-tailed student's t-test) (Figure 4.3F), whereas *PHGDH* KO cell growth remained unaffected ($p>0.99$, two-tailed student's t-test) (Figure 4.3G). Chemical compound pull-down assays were also carried out by Qian to verify PKUMDL-WQ-2101 with the best binding affinity was specifically bound to PHGDH in MDA-MB-468 cells (Figures A3.S1C-A3.S1E). These results indicated that the cytotoxicity to these compounds appears to a large extent specific to PHGDH and serine synthesis.

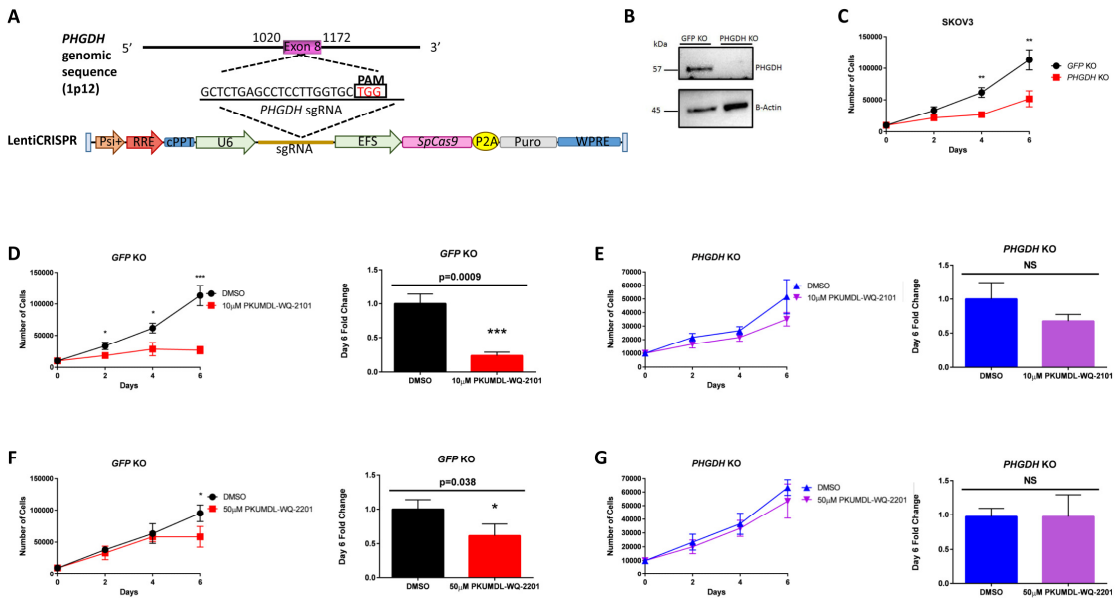

Figure 4.3. CRISPR-Cas9 mediated *PHGDH* KO and PHGDH inhibition by PKUMDL-WQ-2101 and PKUMDL-WQ-2201.
(A) Overview of LentiCRISPR system and sgRNA design generated for targeted *PHGDH* deletion in SKOV3 ovarian cancer cells. **(B)** Western blot analysis for SKOV3 *GFP* KO control and SKOV3 *PHGDH* KO cells with actin as a loading control. **(C)** Growth curve comparing SKOV3 *GFP* KO control and *PHGDH* KO over 6 days. **(D)** Growth curves of SKOV3 *GFP* KO control and **(E)** *PHGDH* KO cells after 6 days of treatment with vehicle or 10μM PKUMDL-WQ-2101 followed by cell counting. **(F)** Growth curves of SKOV3 *GFP* KO control or **(G)** *PHGDH* KO cells after 6 days of treatment with vehicle or 50μM PKUMDL-WQ-2201 followed by cell counting.
All values represent the mean ± SEM from n=3 biological replicates.
P-values were obtained from a two-tailed student's t-test, *P< 0.05, **p<0.01, ***P<0.001.
See Figure A3.S4 for PKUMDL-WQ-2101 and 2201 bioactivies on SKOV3 *GFP* KO cells and results of PKUMDL-WQ-2101 pull down assays.

4.4.4 PKUMDL-WQ-2101 and PKUMDL-WQ-2201 inhibit the serine biosynthesis pathway in cells

I then investigated the effects of *PHGDH* KO on serine metabolism. Liquid chromatography coupled to high resolution mass spectrometry (LC-HRMS) and stable isotope labeling were used to monitor the conversion of uniformly labeled U-^{13}C-glucose to metabolites in the serine metabolic network in both SKOV3 *GFP* KO control and SKOV3 *PHGDH* KO cells (Figure 4.4A). I detected ^{13}C-glucose incorporation in both

serine and glycine in SKOV3 *GFP* KO cells, but not in SKOV3 *PHGDH* KO cells, confirming that the knockout fully abrogated *de novo* serine synthesis (Figure 4.4B). Both compounds (about IC_{50}) also produced comparable metabolic effects on the serine metabolic network and reduced glucose incorporation into serine and glycine metabolites by more than 50% (Figures 4.4C and 4.4D). I further investigated pathways downstream of serine upon inhibition of PHGDH with PKUMDL-WQ-2101 and PKUMDL-WQ-2201. Given that serine is essential for nucleotide synthesis (Locasale, 2013), I investigated whether ^{13}C-glucose consumption into nucleotides was altered after treatment. I analyzed the mass isotopomer distribution (MID) of one pyrimidine and purine synthesis by measuring uridine triphosphate (UTP) and adenosine triphosphate (ATP), and determined whether a difference in the mass shift of 1 or 2 (m+1 or m+2), known to result from incorporation of serine or glycine, was observed. I also monitored any changes in m+6 or m+7, which correspond to labeling from both the pentose phosphate and serine biosynthesis pathways. Upon treatment with both PKUMDL-WQ-2101 and PKUMDL-WQ-2201, decreases in m+2, m+6, and m+7 glucose labeling were observed in UTP and ATP, indicating a direct effect of PHGDH inhibition on nucleotide synthesis (Figure 4.4E and 4.4F). A sharp decrease in the m+5 peak was also observed due to a decrease in ribose labeling from the pentose phosphate pathway, suggesting that PHGDH ablation likely exerts effects on nucleotide synthesis through affecting glycolysis or occurs indirectly as a product of on-target cytotoxicity of the compound. I excluded interpretation of the m+1 peak due to the confounding influence of natural abundance isotopes. I also analyzed glucose incorporation into glutathione, another

metabolite belonging to a pathway downstream of serine and glycine synthesis, in which decreases in m+2 were found in cells treated with both compounds (Figure 4.4G). All together, these data suggest that PHGDH inhibition by PKUMDL-WQ-2101 and PKUMDL-WQ-2201 decreases *de novo* serine synthesis and metabolism downstream of the serine synthesis pathway, with effects comparable to *PHGDH* genetic deletion.

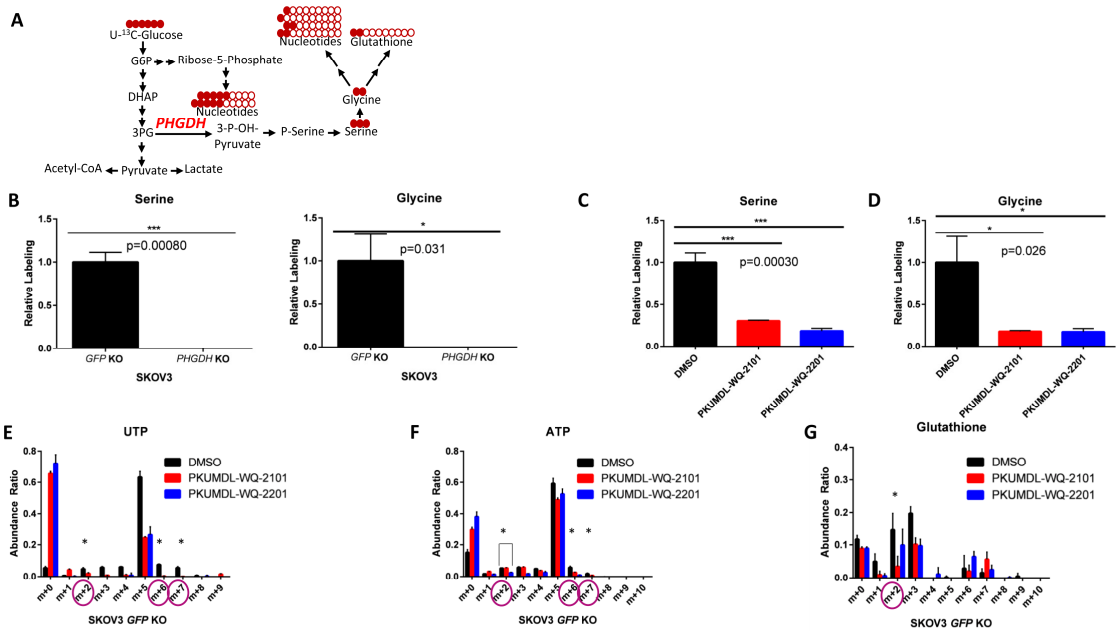

Figure 4.4. PKUMDL-WQ-2101 and PKUMDL-WQ-2201 inhibit the serine biosynthesis pathway in cells.
(A) Schematic of U-^{13}C-glucose stable isotope labeling used to detect carbon labeling from glucose (red) in metabolites part of the serine metabolic network. **(B)** 13C-serine and 13C-glycine labeling from glucose in SKOV3 *GFP* KO control cells compared to SKOV3 *PHGDH* KO cells after 24 hours. **(C)**13C-serine and **(D)** ^{13}C-glycine labeling from glucose in SKOV3 *GFP* KO cells after 24 hour treatment with 37 μM PKUMDL-WQ-2101 and 291 μM PKUMDL-WQ-2201, followed by subsequent U-^{13}C-glucose labeling. **(E)** Mass isotopomer distribution (MID) of UTP and **(F)** ATP after 24 hour treatment with 37 μM PKUMDL-WQ-2101 and 291 μM PKUMDL-WQ-2201, followed by subsequent U-^{13}C-glucose labeling. **(G)** Glutathione after 24 hour treatment with 37 μM PKUMDL-WQ-2101 and 291 μM PKUMDL-WQ-2201, followed by subsequent U-13C-glucose labeling.
All values represent the mean ± SEM from n=3 biological replicates.
Difference is significant by One-Way ANOVA, *P< 0.05, **p<0.01, ***P<0.001.

4.4.5 PKUMDL-WQ-2101 and PKUMDL-WQ-2201 inhibit tumor growth of amplified cell lines

Previous studies have questioned whether PHGDH inhibition is required for

longer term tumor maintenance (Chen et al., 2013). To further understand the role of PHGDH in tumor growth and maintenance in mice, Qian injected MDA-MB-468 and MDA-MB-231 cells into the fourth mammary pad of NOD.CB17 Scid/J mice. Tumor volumes were monitored every 2 days. She found that both PKUMDL-WQ-2101 and PKUMDL-WQ-2201 exhibited substantial inhibitory effects on MDA-MB-468 xenografts compared with vehicle-treated mice after 30 days of drug delivery (Figure 4.5A-4.5F). For MDA-MB-231 xenografts, neither PKUMDL-WQ-2101 nor PKUMDL-WQ-2201 affected tumor growth (Figure A3.S2A and A3.S2B) further confirming the specificity of the compounds and anti-tumor efficacy in *PHGDH*-amplified tumors. Together, these findings confirm the bioactivity and selectivity for PHGDH *in vivo*.

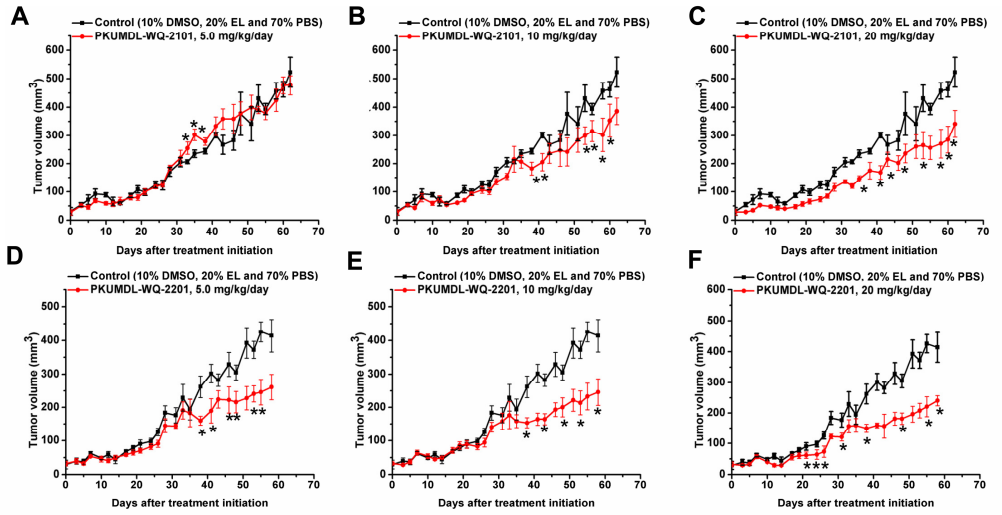

Figure 4.5. Bioactivities of PKUMDL-WQ-2101 and PKUMDL-WQ-2201 *in vivo*.[7]
(A-F) After 30 days of drug delivery, treatment with PKUMDL-WQ-2101 **(A-C)** or PKUMDL-WQ-2201 **(D-F)** significantly suppressed the growth of tumors compared with control-treated group. Data represent the mean ± SEM independent experiments.
Difference is significant by two-tailed multiple t-test, *p < 0.05.
See Figure A3.S2 for PKUMDL-WQ-2101 and 2201 biactivities on MDA-MB-231 xenografts and mice growth curves.

[7] Credit goes to Qian Wang.

4.5 Discussion

Using a structure-based drug design approach, the Luhua lab successfully identified compounds that bound to the predicted allosteric sites and effectively inhibited the enzyme activity of PHGDH. These compounds exhibited sub-micromolar to micromolar binding affinities and inhibited cancer cell growth in the micromolar range. PKUMDL-WQ-2101 and PKUMDL-WQ-2201 showed good activity and selectivity to PHGDH over-expressing breast cancer cells. Both compounds are novel allosteric inhibitors with unique structures and no previous biological activities reported. PKUMDL-WQ-2101 and PKUMDL-WQ-2201 inhibit PHGDH activity primarily through forming hydrogen bonds with site I and site II respectively, limiting the movement of rigid domains and preventing the active sites from closing, thus stabilizing PHGDH in the inactive conformation. Thus, our study provides the first successful example of PHGDH allosteric inhibitor discovery using a structure-based approach.

PHGDH has been shown to be a promising therapeutic target in cancers and has gained attention in recent years. PHGDH is the rate-limiting step for diverting glycolysis into serine synthesis at the 3-phosphoglycerate step, which is then converted to glycine, a reaction important for contribution to one-carbon metabolism, redox homeostasis, and nucleotide synthesis (Locasale, 2013; Locasale et al., 2011; Possemato et al., 2011). In addition, previous studies have shown that *PHGDH*-amplified cancer cells are highly sensitive to PHGDH inhibition (Locasale et al., 2011; Possemato et al., 2011). Therefore, the use of CRISPR-*Cas9* mediated *PHGDH* KO in a *PHGDH*-amplified cell line would

render cells nonviable. Thus, I use CRISPR-*Cas9* technology to develop *PHGDH* KO cells using a *PHGDH*-non-amplified cancer cell line, SKOV3, and provide a genetic evaluation of the relative on- and off-target effects of each compound to show that PKUMDL-WQ-2101 has high selectivity for *PHGDH* control but not KO cells. These results shed light on the utility of genetic perturbations to inform pharmacological specificity.

Moreover, it is well established that while *de novo* serine synthesis contributes only a small fraction of total serine pools in cells, its inhibition in *PHGDH*-amplified cancer cells and tumors affects a multitude of biological processes including cell signaling and proliferation (DeNicola et al., 2015; Kottakis et al., 2016; Locasale et al., 2011; Possemato et al., 2011), contributing to its promise as an anti-tumor target. My findings demonstrate that allosteric inhibition of PHGDH with PKUMDL-WQ-2101 and PKUMDL-WQ-2201 affect downstream metabolic consequences of *de novo* serine synthesis with apparent decreases in nucleotide pools and reduced glutathione, which together contribute to decreases in cell proliferation. In addition, both compounds were shown to suppress *PHGDH*-amplified breast cancer tumor growth in mice. Thus, I anticipate that the use of these novel allosteric inhibitors will serve as useful tools to better understand the metabolic and cellular implications of serine synthesis in cancer cells as well as how PHGDH is required for tumor growth.

Since PHGDH has gained traction over the past several years as a potential therapeutic target in cancer, three recent studies have reported compounds with activities against PHGDH. One study reported an example of a PHGDH inhibitor by screening a

library of 800,000 drug-like compounds (Mullarky et al., 2016). The best compound, CBR-5884, inhibited PHGDH enzymatic activity with an IC_{50} of 33 ± 12 μM in a time-dependent manner. CBR-5884 was speculated to be a covalent inhibitor binding to a Cys in the non-active site and disrupting the enzyme oligomerization state. At 30 μM, CBR-5884 inhibited the growth of MDA-MB-468 cells by 35% to 60% in serine-replete media, and by 80% to 90% in serine-deplete media. Neither a direct binding test nor postulated binding site was reported. CBR-5884 was unstable in mouse plasma and could not be used for *in vivo* testing. Another study reported three PHGDH inhibitors by first screening a 400,000-compound NIH Molecular Libraries Small Molecule Repository (MLSMR) library and then optimizing the lead compounds (Pacold et al., 2016). The best compound, NCT-503, exhibited an IC_{50} value of 2.5 ± 0.6 μM and showed some selectivity in PHGDH-amplified breast cancer cell lines and had bioactivities in a xenograft model. Although NCT-503 was found not to be substrate competitive, its specific binding site remains unknown. The third study reported 15 fragments with PHGDH inhibition activities by first screening a library of 600 fragments, then validating the fragments by using the thermal shift assay, isothermal titration calorimetry (ITC) competition experiments and X-ray crystallography (Unterlass et al., 2018). All 15 fragments bound to the adenine subsite with millimolar binding affinities. However, fragment activities in cells and tumors were not reported. In the present study, we successfully discovered novel allosteric inhibitors for PHGDH using structure-based design approach with the best IC_{50} of 28.1 ± 1.3 μM for enzyme inhibition. PKUMDL-WQ-2101 and PKUMDL-WQ-2201 were confirmed to specifically bind to PHGDH in PHGDH-amplified breast cancer cells

with IC_{50} values less than 10 μM in serine-replete media, which was better than that of CBR-5884 and similar to that of NCT-503. Furthermore, PKUMDL-WQ-2101 and PKUMDL-WQ-2201 also suppressed tumor growth in mice. The Luhua lab started from purposely designing allosteric inhibitors for the predicted allosteric sites, while CBR-5884 and NCT-503 were found from high-throughput screening. Nevertheless, all the compounds inhibit PHGDH by an allosteric effect, demonstrating that allosteric inhibition is a promising strategy to suppress its activity. More allosteric inhibitors for PHGDH can be expected in the future.

In the past decade, considerable efforts have been devoted to identifying agents to suppress oncogenesis and tumor progression (Hanahan and Weinberg, 2011), and subsequently developing drugs to selectively kill cancer cells based on their metabolic alterations. Several drug candidates were successfully discovered and entered into clinical trials, such as AZD3965 (Birsoy et al., 2013; Sonveaux et al., 2008) and TCD-717 (Clem et al., 2011). Some anti-metabolite agents have even been used in the clinic for years including 5-fluorouracil, methotrexate, and gemcitabine (Galluzzi et al., 2013). We are hopeful that PKUMDL-WQ-2101 and PKUMDL-WQ-2201 may be an additional starting point for further targeting cancer metabolism. In conclusion, we have successfully discovered PHGDH allosteric inhibitors targeting the predicted allosteric sites by using virtual screening and experimental validation. The compounds reported can be further optimized and developed for next-generation anti-cancer therapies.

4.6 Experimental Procedures

4.6.1 Allosteric site prediction and virtual screening

Potential allosteric sites in PHGDH N-terminal fragment structure containing the substrate binding and the nucleotide binding domains (PDB code: 2G76) were identified using the CAVITY program (Yuan et al., 2011, 2013) and then applied to screen for potential allosteric inhibitors. The program Glide Standard Precise (SP) mode and Extra Precise (XP) mode were used to do the molecular docking studies and screen the SPECS library (Friesner et al., 2004; Halgren et al., 2004). The top 5% compounds from the XP mode were chosen for manual selection and purchased from SPECS for experimental testing.

4.6.2 Molecular cloning, protein expression, and purification

The full-length PHGDH or PSAT1 open reading frame (Seajet Scientific, Beijing, China) was amplified by polymerase chain reaction (PCR). The PCR fragments were ligated into the pET21a (+) vector, confirmed by DNA sequencing (Genewiz, Beijing, China), and transformed to the BL21 (DE3) strain of *Escherchia coli* (*E. coli*). Recombinant cell was cultivated at 37℃ until the OD_{600} reached 0.6-0.8. Then, PHGDH or PSAT1 expression was induced and the cells were grown for another 8 h at 25℃. Cells were harvested by centrifugation (6000 rpm, 15 min) and broken by sonication. Insoluble material was separated by centrifugation (17000 rpm, 30 min) and the supernatant was purified using a nickel-nitrilotriacetic column (HisTrap HP; GE Healthcare) and then a gel-filtration column (Sephacryl S-200 HR, GE Healthcare). The final purity of the protein was >95% as judged by SDS−PAGE. Protein concentrations were measured via

Nanodrop 2000 (Thermo Scientific, USA).

4.6.3 Enzyme assay

Due to the unavailability of PHGDH direct-substrate phosphohydroxypyruvate (PHP), the enzyme activity of PHGDH was measured accompanied with the upstream of PSAT1 catalytic reaction. The activity of recombinant PHGDH was measured by monitoring the reduced nicotinamide adenine dinucleotide (NADH) to nicotinamide adenine dinucleotide (NAD^+) change in fluorescence emission at 456 nm (excitation at 338 nm).

To evaluate the effects of compounds on PHGDH activity, compounds were first pre-incubated with enzyme samples in the assay buffer (25 mM HEPES, pH 7.1, 400 mM KCl, 5 μM phosphopyridoxa (PLP), 0.5 mM α-ketoglutarate, 150 μM NADH, 1 mM DTT) for 10 min at 25℃, then the reaction was started by adding L-phospho-O-serine (Pser). Each compound was dissolved in DMSO at a final concentration of 5%, which did not affect the assay signal. Fluorescence signals were recorded for 3 min with a kinetics mode program using on a plate reader (Synergy, Biotek). IC_{50} values were obtained by fitting the data to a three-parameter Hill model of the graph of log dose against percentage inhibition from at least three sets of experiments. Percentages of inhibition were calculated according to the following equation:

$$\frac{\mathrm{Vo} - \mathrm{Vi}}{\mathrm{Vo} - \mathrm{Vn}}$$

in which Vo and Vi represent the maximum reaction rate of the enzyme incubated without or with compounds, and Vn represents the maximum degradation rate of NADH.

4.6.4 Surface plasmon resonance (SPR) experiments

The binding affinities of compounds towards PHGDH were assayed using the SPR-based Biacore T200 instrument (GE Healthcare). PHGDH was immobilized on a CM5 sensor chip by using standard amine-coupling at 25℃ with running buffer PBS-P (20 mM phosphate buffer, 2.7 mM NaCl, 137 mM KCl, 0.05% surfactant P-20, pH 7.4), respectively, as described previously. A reference flow cell was activated and blocked in the absence of PHGDH. In the direct binding experiments between PHGDH and compounds, PHGDH immobilization level was fixed at 800 response units (RU), and then different concentrations of compounds containing 5% DMSO were serially injected into the channel to evaluate binding affinity. Regeneration was achieved by extended washing with the running buffer after each sample injection. The equilibrium dissociation constants (K_D) of the compounds were obtained by fitting the data sets to 1:1 Langmuir binding model using Biacore T200 Evaluation Software.

Circular dichroism

WT PHGDH and its mutants were dissolved to a final concentration of 0.2 mg/ml in PBS buffer (20 mM phosphate buffer, 2.7 mM NaCl, 137 mM KCl, pH 7.4). CD spectra was recorded using 1-mm quartz cuvettes for the far ultraviolet region (190-260 nm) on a MOS 450 AF/CD (Biologic, France) at 25°C. The spectra were corrected by subtracting a buffer blank and were averaged over three accumulations and smoothed by standard noise reduction provided with the instrument.

4.6.5 Competition experiments

To investigate competition effects between the compounds and the cofactor

NADH, we performed compound-cofactor competition experiments as follows:

Before Pser was added to start the reaction, the enzyme sample was pre-incubated with the cofactor and the compound for 10 min at 25℃. The compound was kept at a constant inhibitory concentration (50 μM), while NADH concentration was gradually increased from 5 to 40 μM. At these concentrations, the compounds inhibited PHGDH activity by ~50% when the NADH concentration was 150 μM.

4.6.5 Mutagenesis experiments

All mutagenesis experiments were carried out according to the instructions of the QuikChangeSite-Directed Mutagenesis (SBS Genetech Co., Beijing, China). The plasmid pET-21a(+)-containing wild-type (WT) PHGDH was mutated to obtain the mutants. The DNA sequences of all mutants were verified by DNA sequencing. The protein expression and activity assays of the mutants were performed as described for the WT.

4.6.6 Cell culture

MDA-MB-468, MDA-MB-231, and ZR-75-1 from China Infrastructure Cell Line Resources, and SKOV3 and HCC70 from ATCC were maintained in RPMI-1640 culture medium (Gibco) supplemented with 10% fetal bovine serum and 1% penicillin/ml/streptomycin. MCF-7 from China Infrastructure Cell Line Resources and HEK293T from ATCC were maintained in Dulbecco's modified Eagle's medium (DMEM, Gibco) supplemented with 10% fetal bovine serum and 1% penicillin/ml/streptomycin. MCF-10A from China Infrastructure Cell Line Resources was maintained in DMEM/F12 (1:1) medium (Gibco) and supplemented with 5% horse serum, 10 μg/ml insulin, 0.1 μg/ml cholera toxin, 0.5 μg/ml hydrocortisone, and 0.02

μg/ml epidermal growth factor (EGF).

4.6.7 Proliferation assays

SKOV3 *GFP* KO and *PHGDH* KO cells (10,000 cells/well) were plated into 24-well culture plates in triplicate. After 24 hours, cells were treated with DMSO or compound. Each day, cells were counted by trypan-blue exclusion test for cell viability at a 1:1 ratio using a hemocytometer.

4.6.8 MTT assays

MDA-MB-468 (5000 cells/well), HCC70 (5000 cells/well), MCF-7 (3000 cells/well), MDA-MB-231 (2000 cells/well), ZR-75-1 (4000 cells/well), and MCF-10A (3000 cells/well) in exponential growth were plated into 96-well culture plates and allowed to adhere overnight. The number of viable cells was assessed by spectrophotometry at 490 nm using a BioTek Synergy4 microplate reader after 3 days of treatment and calculated as the percentage of absorbance of treated cells relative to that of solvent controls.

SKOV3 WT/KO cells (30,000 cells/well) were plated in a 96-well plate. The following day, media was aspirated and replaced with 100 μl phenol-red free RPMI-1640 (Gibco) and 12mM Methyl thiazolyldiphenyl-tetrazoliumbromide (MTT, Thermo Fisher Scientific) was added to the cells. After 4 hours, the media containing MTT was aspirated and 50 μl DMSO was added to dissolve the formazan and read at 540nm.

4.6.9 Synergistic experiments between PKUMDL-WQ-2101 and PKUMDL-WQ-2201 in enzymatic assays and cell-based assays

For enzymatic assay, one concentration among 0, 1, 5, 12.5, 25, 50, 100, 200 μM

of PKUMDL-WQ-2101 was successively mixed with different concentrations of PKUMDL-WQ-2201 (0, 1, 5, 12.5, 25, 50, 100, 200 μM), and the mixture was then pre-incubated with enzyme samples to test their effects on PHGDH activity.

For cell-based assays, MDA-MB-468 cells (5000 cells/well) were plated in 96-well plates, allowed to adhere overnight and incubated with the different combinations of PKUMDL-WQ-2101 (0, 0.1, 0.5, 1, 2.5, 5, 7.5, 10 μM) and PKUMDL-WQ-2201 (0, 0.1, 0.5, 1, 2.5, 5, 7.5, 10 μM) for three days. The IC_{50} values of the combinations were measured by MTT methods.

4.6.10 CRISPR-*Cas9* sgRNA design

To design specific sgRNAs to target *PHGDH*, an online tool called E-CRISP (Heigwer et al., 2014) software database e-crisp.org was used. Target sequences complementary to the gRNA, followed by a PAM sequence of NGG, were generated which is required for double stranded DNA cuts by Cas9 nuclease. sgRNAs were ranked by off-target effects and target-site homology using the BowTie2 alignment program. Outputs of sgRNAs specific to the *PHGDH* genomic sequence were generated with an average specificity score, annotation score, and efficacy score. This resulted in 5 sgRNAs with a score of 100% across all scores. One sgRNA (GCTCTGAGCCTCCTTGGTGC) efficiently knocked out *PHGDH* and used for this study.

4.6.11 Cell transfection, transduction, and puromycin selection

LentiCRISPR transfer plasmid (Addgene Plasmid 49535), LentiCRISPR- EGFP sgRNA 1 (Addgene Plasmid 51760), PMD2.G VSV-G envelope expressing plasmid (Addgene Plasmid 12259), and PsPAX.2 lentiviral packaging plasmid (Addgene Plasmid

12260) were purchased. The target sequence of the sgRNA is GCTCTGAGCCTCCTTGGTGC (exon 8 of *PHGDH*). The plasmids, along with the synthesized LentiCRISPR-*PHGDH* sgRNA were virally transfected into HEK293T cells using polyethylemine (PEI) (Polysciences, Inc) to generate either LentiCRISPR-PHGDH or LentiCRISPR-EGFP virus for 48 hours. The day before transduction, SKOV3 cells were plated in 3 x 10cm^2 tissue culture dishes. The day of transduction, 4 mL of DMEM supplemented with 10% FBS, 100U/ml penicillin and 100mg/ml streptomycin was added to one dish, while 4mL of LentiCRISPR-PHGDH or LentiCRISPR-EGFP were added to the other dishes of SKOV3 cells. Next, 2.5 µl of 1 mg/ml polybrene transfection reagent (Millipore) was added to each plate. Virally infected SKOV3 cells and control plate were incubated at 37˚C. After 24 hours, media from each plate was aspirated and fresh RPMI-1640 (sigma), 10% FBS, 100U/ml penicillin, 100mg/ml streptomycin with 2 µg/ml puromycin was added for 3 days. Virally infected LentiCRISPR-PHGDH and LentiCRISPR-EGFP plates were compared to the non-transduced plate to ensure complete cell death of those cells. To ensure complete gene knockout of transduced cell lines, cell cloning by serial dilution was performed using a 96-well plate on puromycin-resistant cells. After 4 days, wells were checked for single cells. Those wells containing single cells were allowed to reach confluency for 3 weeks and subsequently seeded in 6-well then 10cm^2 plates and validated by western blotting.

4.6.12 Immunoblotting

Protein was extracted from cells using 1X RIPA buffer (Rockland Immunochemicals, Inc.) and centrifuged at 2000 rpm for 30 minutes at 4˚C. Protein

concentrations were measured using Bradford Protein Assay (Bio-Rad) and loaded onto 7.5% SDS-PAGE gels transferred to PVDF membranes. Membranes were blocked in 5% dry milk in TBST and incubated with anti-β-actin (Cell Signaling 8H10D10) 1:2000 or anti-PHGDH (Sigma-Aldrich WH0026227M1) 1:1000. Horseradish peroxidase conjugated anti-mouse (Rockland 611G4302), 1:2000 was used as secondary antibody. Chemiluminescent signals were detected with Clarity Western ECL Detection Kit (Bio-Rad) and imaged using a ChemiDoc MP System (Bio-Rad).

4.6.13 U-^{13}C-glucose stable isotope labeling

SKOV3 cells (300,000 cells/well) were plated in a 6-well plate and allowed to adhere to the plate. Cells were then replaced with RPMI-1640 media containing 11mM U^{13}C-glucose (Cambridge Isotope Laboratories, Inc.) and incubated for 24 hours. For U^{13}C-glucose tracing with drug treatments, cells were first treated with their corresponding compounds for 24 hours, followed by media replacement with 11mM U-^{13}C-glucose and corresponding drug treatment. Metabolites were then extracted.

4.6.14 Metabolite extraction

For culture from adherent SKOV3 cells, media was quickly aspirated. Next, 1mL of extraction solvent (80% methanol/water) cooled to -80˚C was added immediately to each well and the dishes were then transferred to -80˚C for 15 min. After, the plates were removed, and cells were scraped into the extraction solvent on dry ice. All metabolite extractions were centrifuged at 20,000*g* at 4˚C for 10 min. Finally, the solvent in each sample was evaporated using a speed vacuum for metabolite analysis. For polar metabolite analysis, the cell metabolite extract was dissolved in 15 µl

methanol/acetonitrile (1:1 *v/v*) (LC-MS optima grade, Thermo Scientific). Samples were centrifuged at 20,000*g* for 10 min at 4˚C and the supernatants were transferred to Liquid Chromatography (LC) vials. The injection volume for polar metabolite analysis was 2 µL.

4.6.15 Liquid chromatography

An Xbridge amide column (100 x 2.1mm i.d., 3.5 µm; Waters) is employed on a Dionex (Ultimate 3000 UHPLC) for compound separation at room temperature. Mobile phase A is 5mM ammonium acetate and, pH 6.0, and mobile phase B is 100% acetonitrile. The gradient is linear as follows: 0 min, 85% B; 1.5 min, 85% B; 5.5 min, 35% B; 10 min, 35% B; 10.5 min, 35% B; 14.5 min, 35% B; 15 min, 85% B; and 20 min, 85% B. The flow rate was 0.15 mL/min from 0 to 10 min and 15 to 20 min, and 0.3 mL/min from 10.5 to 14.5 min. All solvents are LC-MS grade and purchased from Fisher Scientific.

4.6.16 Mass spectrometry

The Q ExactivePlus MS (Thermo Scientific) is equipped with a heated electrospray ionization probe (HESI) and the relevant parameters are as listed: evaporation temperature, 120˚C; sheath gas, 30; auxillary gas, 10; sweep gas, 3; spray voltage, 3.6kV for positive mode and 2.5kV for negative mode. Capillary temperature was set at 320˚C, and S lens was 55. A full scan range from 60 to 900 (m/z) was used. The resolution was set at 70,000. The maximum injection time was 200 ms. Automated gain control (AGC) was targeted at 3,000,000 ions.

4.6.17 Peak extraction and data analysis

Raw data collected from LC-Q Exactive Plus MS is processed on Sieve 2.0 (Thermo Scientific). Peak alignment and detection are performed according to the protocol described by Thermo Scientific. For a targeted metabolite analysis, the method "peak alignment and frame extraction" is applied. An input file of theoretical m/z and detected retention time of 197 known metabolites is used for targeted metabolite analysis with data collected in positive mode, while a separate input file of 262 metabolites is used for negative mode. m/z width is set to 10 ppm. The output file including detected m/z and relative intensity in different samples is obtained after data processing. If the lowest integrated mass spectrometer signal (MS intensity) is less than 1000 and the highest signal is less than 10,000, then this metabolite is considered below the detection limit and excluded for further data analysis. If the lowest signal is less than 1000, but the highest signal is more than 10,000, then a value of 1000 is imputed for the lowest signals. Serine and glycine samples were normalized by comparing relative labeling of glucose-derived labeled metabolites from treated with vehicle samples. For all other samples, mass isotopomer distributions (MID) were calculated and samples were normalized by comparing the ratio of glucose-derived labeled metabolites to unlabeled metabolites within each sample. Quantitation and statistics were calculated using Microsoft Excel and GraphPad Prism 6.

4.6.18 Pull-down assays

Biotinylated PKUMDL-WQ-2101 targeting endogenous PHGDH in MDA-MB-468 cells was performed using M-280 streptavidin Dynabeads (Invitrogen). As described

in the protocol of manufacturer, 100 µl suspension of beads was first washed three times with 100 µl PBS buffer (20 mM phosphate buffer, 2.7 mM NaCl, 137 mM KCl, pH 7.4); 100 µl 60 µM biotinylated PKUMDL-WQ-2101 (5% DMSO) or biotin (5% DMSO) was then added to the beads, gently rotated at 25℃for 1h, washed three times with 200 µl PBST buffer (PBS buffer, 0.5% Tween 20), blotted with 100 µl 5% BSA buffer (final concentration 1 mg/ml) and washed three times with 200 µl PBST buffer; MDA-MB-468 cells were lysed according to the instruction of NP40 (Invitrogen), and 200 µl 20 mg/ml cell lysate supernatant was then added to free streptavidin beads, biotin immobilized beads and PKUMDL-WQ-2101-biotin immobilized beads respectively, gently rotated at 25℃ for 1h. Another 80 µl 2 mg/ml cell lysate supernatant was directly mixed with 20 µl 5x SDS loading buffer, boiled at 95℃for 10 min and collected for further western blot analysis; after three times wash with PBST buffer, the beads were finally resuspended in 80 µl washing buffer and 20 µl 5x SDS loading buffer, followed by heating at 80℃for 10 min.

Proteins were resolved by 12% SDS/PAGE and transferred on to polyvinylidenedifluoride (PVDF) membranes (Millipore) for western blot analysis. The membranes were then blocked with 30 ml TBST buffer (136.9 mM NaCl, 2.68 mM KCl, 24.8 mM Tris (pH 7.4) with HCl, and0.1% Tween 20) contained 5% dry milk while being gently shaken at 25℃for 1h. After blocking, the membranes were incubated with a 1:500 dilution of mouse monoclonal PHGDH antibody (Santa Cruz) and then 1:500 dilution of horseradish peroxidase-conjugated goat anti-mouse IgG antibody (Santa Cruz). PHGDH was detected by chemiluminescence (Vigorous Biotechnology).

Two biological replicate samples were generated and analyzed for PKUMDL-WQ-2101 and cell lysate supernatant.

4.6.19 MDA-MB-468 and MDA-MB-231 xenograft mouse models

PKUMDL-WQ-2101 and PKUMDL-WQ-2201 bioactivity assay *in vivo* - All animal experiments were performed in compliance with guidelines of the Animal Welfare Act and the guide for the care and use of laboratory animals following protocols approved by the Institutional Animals Care and Use Committee (IACUC). MDA-MB-468 or MDA-MB-231 cells were injected into the fourth mammary fat pad of NOD.CB17 Scid/J mice at 2×10^5 or 5×10^5 cells per injection site, respectively (Vital River Laboratory Animal Technology Co., Ltd., Beijing, China). For MDA-MB-468, when the average tumor volume reached 30 mm^3, the mice were randomized into 7 groups (n=5): vehicle control (10%DMSO, 20% EL and 70% PBS, IP); 20, 10, and 5 mg/kg/day PKUMDL-WQ-2101 or PKUMDL-WQ-2201 (IP), respectively. For MDA-MB-231, after the tumor was palpable, the mice were randomized into 3 groups (n=5): vehicle control (10%DMSO, 20% EL and 70% PBS, IP); 20 mg/kg/day PKUMDL-WQ-2101 (IP); 20 mg/kg/day PKUMDL-WQ-2201 (IP). The tumor volume was calculated using the formula width $(mm)^2\times$ length (mm) $\times$ 0.5.

4.7 References

Beroukhim, R., Mermel, C.H., Porter, D., Wei, G., Raychaudhuri, S., Donovan, J., Barretina, J., Boehm, J.S., Dobson, J., Urashima, M.*, et al.* (2010). The landscape of somatic copy-number alteration across human cancers. Nature *463*, 899-905.

Birsoy, K., Wang, T., Possemato, R., Yilmaz, O.H., Koch, C.E., Chen, W.W., Hutchins, A.W., Gultekin, Y., Peterson, T.R., Carette, J.E.*, et al.* (2013). MCT1-mediated transport of a toxic molecule is an effective strategy for targeting glycolytic tumors. Nat Genet *45*, 104-108.

Chen, J., Chung, F., Yang, G., Pu, M., Gao, H., Jiang, W., Yin, H., Capka, V., Kasibhatla, S., and Laffitte, B. (2013). Phosphoglycerate dehydrogenase is dispensable for breast tumor maintenance and growth. Oncotarget *4*, 2502.

Clem, B.F., Clem, A.L., Yalcin, A., Goswami, U., Arumugam, S., Telang, S., Trent, J.O., and Chesney, J. (2011). A novel small molecule antagonist of choline kinase-alpha that simultaneously suppresses MAPK and PI3K/AKT signaling. Oncogene *30*, 3370-3380.

DeNicola, G.M., Chen, P.H., Mullarky, E., Sudderth, J.A., Hu, Z., Wu, D., Tang, H., Xie, Y., Asara, J.M., Huffman, K.E.*, et al.* (2015). NRF2 regulates serine biosynthesis in non-small cell lung cancer. Nat Genet *47*, 1475-1481.

Ding, J., Li T Fau - Wang, X., Wang X Fau - Zhao, E., Zhao E Fau - Choi, J.-H., Choi Jh Fau - Yang, L., Yang L Fau - Zha, Y., Zha Y Fau - Dong, Z., Dong Z Fau - Huang, S., Huang S Fau - Asara, J.M., Asara Jm Fau - Cui, H.*, et al.* (2013). The histone H3 methyltransferase G9A epigenetically activates the serine-glycine synthesis pathway to sustain cancer cell survival and proliferation. cell metabolism *18*, 896-907.

Fan, J., Ye, J., Kamphorst, J.J., Shlomi, T., Thompson, C.B., and Rabinowitz, J.D. (2014). Quantitative flux analysis reveals folate-dependent NADPH production. Nature *510*, 298-302.

Friesner, R.A., Banks, J.L., Murphy, R.B., Halgren, T.A., Klicic, J.J., Mainz, D.T., Repasky, M.P., Knoll, E.H., Shelley, M., Perry, J.K.*, et al.* (2004). Glide: a new approach for rapid, accurate docking and scoring. 1. Method and assessment of docking accuracy. Journal of medicinal chemistry *47*, 1739-1749.

Galluzzi, L., Kepp, O., Vander Heiden, M.G., and Kroemer, G. (2013). Metabolic targets for cancer therapy. Nat Rev Drug Discov *12*, 829-846.

Halgren, T.A., Murphy, R.B., Friesner, R.A., Beard, H.S., Frye, L.L., Pollard, W.T., and Banks, J.L. (2004). Glide: a new approach for rapid, accurate docking and scoring. 2. Enrichment factors in database screening. Journal of medicinal chemistry *47*, 1750-1759.

Hanahan, D., and Weinberg, R.A. (2011). Hallmarks of cancer: the next generation. Cell *144*, 646-674.

Heigwer, F., Kerr, G., and Boutros, M. (2014). E-CRISP: fast CRISPR target site identification. Nature methods *11*, 122-123.

Kottakis, F., Nicolay, B.N., Roumane, A., Karnik, R., Gu, H., Nagle, J.M., Boukhali, M., Hayward, M.C., Li, Y.Y., and Chen, T. (2016). LKB1 loss links serine metabolism to DNA methylation and tumorigenesis. Nature *539*, 390.

Locasale, J.W. (2013). Serine, glycine and one-carbon units: cancer metabolism in full circle. Nature Reviews Cancer *13*, 572-583.

Locasale, J.W., Grassian, A.R., Melman, T., Lyssiotis, C.A., Mattaini, K.R., Bass, A.J., Heffron, G., Metallo, C.M., Muranen, T., Sharfi, H., *et al.* (2011). Phosphoglycerate dehydrogenase diverts glycolytic flux and contributes to oncogenesis. Nat Genet *43*, 869-874.
Ma, L., Tao Y Fau - Duran, A., Duran A Fau - Llado, V., Llado V Fau - Galvez, A., Galvez A Fau - Barger, J.F., Barger Jf Fau - Castilla, E.A., Castilla Ea Fau - Chen, J., Chen J Fau - Yajima, T., Yajima T Fau - Porollo, A., Porollo A Fau - Medvedovic, M., *et al.* (2013). Control of nutrient stress-induced metabolic reprogramming by PKCzeta in tumorigenesis. Cell *152*, 599-611.
Mali, P., Yang, L., Esvelt, K.M., Aach, J., Guell, M., DiCarlo, J.E., Norville, J.E., and Church, G.M. (2013). RNA-guided human genome engineering via Cas9. Science *339*, 823-826.
Meng, H., McClendon, C.L., Dai, Z., Li, K., Zhang, X., He, S., Shang, E., Liu, Y., and Lai, L. (2015). Discovery of novel 15-lipoxygenase activators to shift the human arachidonic acid metabolic network toward inflammation resolution. Journal of medicinal chemistry *59*, 4202-4209.
Mentch, S.J., Mehrmohamadi, M., Huang, L., Liu, X., Gupta, D., Mattocks, D., Gomez Padilla, P., Ables, G., Bamman, M.M., Thalacker-Mercer, A.E., *et al.* (2015). Histone Methylation Dynamics and Gene Regulation Occur through the Sensing of One-Carbon Metabolism. Cell metabolism *22*, 861-873.
Merdanovic, M., Monig, T., Ehrmann, M., and Kaiser, M. (2013). Diversity of allosteric regulation in proteases. ACS Chem Biol *8*, 19-26.
Mullarky, E., Lucki, N.C., Beheshti Zavareh, R., Anglin, J.L., Gomes, A.P., Nicolay, B.N., Wong, J.C., Christen, S., Takahashi, H., Singh, P.K., *et al.* (2016). Identification of a small molecule inhibitor of 3-phosphoglycerate dehydrogenase to target serine biosynthesis in cancers. Proceedings of the National Academy of Sciences of the United States of America *113*, 1778-1783.
Ou, Y., Wang, S.J., Jiang, L., Zheng, B., and Gu, W. (2015). p53 Protein-mediated Regulation of Phosphoglycerate Dehydrogenase (PHGDH) Is Crucial for the Apoptotic Response upon Serine Starvation. Journal of Biological Chemistry *290*, 457-466.
Pacold, M.E., Brimacombe, K.R., Chan, S.H., Rohde, J.M., Lewis, C.A., Swier, L.J., Possemato, R., Chen, W.W., Sullivan, L.B., and Fiske, B.P. (2016). A PHGDH inhibitor reveals coordination of serine synthesis and one-carbon unit fate. Nature chemical biology.
Pavlova, N.N., and Thompson, C.B. (2016). The Emerging Hallmarks of Cancer Metabolism. Cell Metab *23*, 27-47.
Pei, J., Yin, N., Ma, X., and Lai, L. (2014). Systems biology brings new dimensions for structure-based drug design. Journal of the American Chemical Society *136*, 11556-11565.
Possemato, R., Marks, K.M., Shaul, Y.D., Pacold, M.E., Kim, D., Birsoy, K., Sethumadhavan, S., Woo, H.K., Jang, H.G., Jha, A.K., *et al.* (2011). Functional genomics reveal that the serine synthesis pathway is essential in breast cancer. Nature *476*, 346-350.
Shalem, O., Sanjana, N.E., Hartenian, E., Shi, X., Scott, D.A., Mikkelsen, T.S., Heckl,

D., Ebert, B.L., Root, D.E., and Doench, J.G. (2014). Genome-scale CRISPR-Cas9 knockout screening in human cells. Science *343*, 84-87.
Sonveaux, P., Vegran, F., Schroeder, T., Wergin, M.C., Verrax, J., Rabbani, Z.N., De Saedeleer, C.J., Kennedy, K.M., Diepart, C., Jordan, B.F.*, et al.* (2008). Targeting lactate-fueled respiration selectively kills hypoxic tumor cells in mice. J Clin Invest *118*, 3930-3942.
Turnbull, A.P., Salah, E., Savitsky, P., Gileadi, O., von Delft, F., Edwards, A., Arrowsmith, C., Weigelt, J., Sundstrom, M., Oppermann, U. (2006). Crystal structure of human 3-phosphoglycerate dehydrogenase.
Unterlass, J.E., Baslé, A., Blackburn, T.J., Tucker, J., Cano, C., Noble, M.E., and Curtin, N.J. (2018). Validating and enabling phosphoglycerate dehydrogenase (PHGDH) as a target for fragment-based drug discovery in PHGDH-amplified breast cancer. Oncotarget *9*, 13139.
Wagner, J.R., Lee, C.T., Durrant, J.D., Malmstrom, R.D., Feher, V.A., and Amaro, R.E. (2016). Emerging computational methods for the rational discovery of allosteric drugs. Chemical reviews *116*, 6370-6390.
Wang, Q., Qi, Y., Yin, N., and Lai, L. (2014). Discovery of novel allosteric effectors based on the predicted allosteric sites for Escherichia coli D-3-phosphoglycerate dehydrogenase. PLoS One *9*, e94829.
Warburg, O. (1956). On the origin of cancer cells. Science *123*, 309-314.
Yamada, K., Hara, N., Shibata, T., Osago, H., and Tsuchiya, M. (2006). The simultaneous measurement of nicotinamide adenine dinucleotide and related compounds by liquid chromatography/electrospray ionization tandem mass spectrometry. Analytical biochemistry *352*, 282-285.
Yuan, Y., Pei, J., and Lai, L. (2011). LigBuilder 2: a practical de novo drug design approach. J Chem Inf Model *51*, 1083-1091.
Yuan, Y., Pei, J., and Lai, L. (2013). Binding site detection and druggability prediction of protein targets for structure-based drug design. Current pharmaceutical design *19*, 2326-2333.
Zhao, E., Ding, J., Xia, Y., Liu, M., Ye, B., Choi, J.H., Yan, C., Dong, Z., Huang, S., Zha, Y.*, et al.* (2016). KDM4C and ATF4 Cooperate in Transcriptional Control of Amino Acid Metabolism. Cell reports *14*, 506-519.

CHAPTER 5: CONCLUSIONS AND FUTURE DIRECTIONS

5.1 Background and context

This chapter will summarize the findings from each chapter, draw conclusions, and discuss future directions of these projects. I will also provide insight on overall areas of future investigation for targeting the Warburg Effect.

5.2 Therapeutic targeting of the Warburg Effect in cancer

The discovery of the Warburg Effect dates back to nearly a century ago with clear evidence of increased glucose consumption and lactate secretion in the presence or absence of oxygen in tumors (Warburg, 1956; Warburg et al., 1927). Although the Warburg Effect is of paramount importance in the clinic for diagnostics with fluorodeoxyglucose-positron emission tomography (FDG-PET) imaging for staging of cancers (Ben-Haim and Ell, 2009; Vander Heiden et al., 2009), there has been limited success in therapeutically targeting the Warburg Effect. While there have been numerous efforts to target canonically regarded rate-limiting steps in glycolysis (Galluzzi et al., 2013; Hay, 2016; Luengo et al., 2017; Vander Heiden, 2011, 2013), there are also many challenges associated with these efforts including toxicity to surrounding tissues, off-target effects, and limited efficacy (Galluzzi et al., 2013; Vander Heiden, 2013). Thus, there is an unmet clinical need to identify strategies to therapeutically target the Warburg Effect in such a way that limits tumor progression but leaves normal tissues unaffected. It is important to note that therapeutic targeting of the Warburg Effect is not only limited to targeting enzymes in glycolysis. Because the Warburg Effect exerts important functions across central carbon metabolism, and because I have shown through this work that the Warburg Effect is a distinct entity from glycolysis, it is conceivable that targeting one of its branching pathways can also influence the Warburg Effect as has been seen with knockdown experiments of 3-phosphoglycerate dehydrogenase (PHGDH) previously (Locasale et al., 2011). Thus, there remains a disconnect in the field of appreciating the important potential of targeting the Warburg Effect and executing the

most effective therapeutic strategies to do so.

5.3 Summary of results and conclusions

Chapter 2 of this dissertation systematically addressed challenges associated with targeting the Warburg Effect by therapeutically exploiting a glycolytic enzyme with differential control properties over the Warburg Effect, namely glyceraldehyde-3-phosphate dehydrogenase (GAPDH). Using comparative metabolomics, I found that koningic acid (KA), a natural product produced by the *Trichoderma* species, targets glycolysis and branching pathways. By expressing the fungal-derived KA-resistant *GAPDH* allele, I demonstrated that KA is highly specific and selective for GAPDH. In collaboration with the National Cancer Institute (NCI), we found a heterogeneous response to KA across 60 cancer cells both in proliferation and in cellular metabolism, independent of tissue type. Using pharmacogenomics and a multi-omics approach, my collaborators and I found that doubling time, cell size, mutational, gene expression, and protein expression do not predict the heterogeneous response to KA. However, I found that glucose and lactate fluxes correlate most strongly with KA treatment, indicating that the quantitative extent of the Warburg Effect predicts response to KA. Subsequently, I was able to show that KA is bioavailable, and I identified a therapeutic window of KA *in vivo* of 1mg/kg. Lastly, I determined that the extent of the Warburg Effect predicts KA response in tumors as well, where high Warburg Effect tumors are sensitive to KA, but low Warburg Effect tumors are only marginally sensitive.

The results from chapter 2 provide evidence for underappreciated concepts in the

cancer therapy and metabolism fields. Firstly, there have been numerous conflicting reports on the rate-limiting enzymes of the Warburg Effect. Our results systematically show that based on a previous study using metabolic control analysis (MCA) to identify rate-limiting steps during the Warburg Effect (Bakker et al., 2000; Shestov et al., 2014), GAPDH does appear to exert the most differential control over the Warburg Effect compared to oxidative phosphorylation. This finding highlights the applicability of MCA in a therapeutic setting. Secondly, the remarkable selectivity of KA for the Warburg Effect by GAPDH inhibition demonstrates that KA is a suitable candidate for further pre-clinical analysis. Thirdly, the current paradigm for cancer therapy is genetic factors. However, this study importantly defines a context by which metabolism can be predictive of the responsiveness to an inhibitor. In fact, these findings demonstrate that in some contexts, the only predictive measurement for the success or failure of an anti-cancer therapy is at the metabolic level. Thus, this study reiterates the importance of taking the metabolic network and environment into consideration when determining anti-cancer therapy regimens and demonstrates that this is clinically relevant and possible.

The main goal of chapter 3 was to address another outstanding question in the field of whether glucose metabolism can exist in multiple states in the cell and how this influences metabolic outputs. While the Warburg Effect has been well-established, its biological role remains controversial, as delineated in chapter 1. Since chapter 2 demonstrated the utility of KA to specifically target cells undergoing the Warburg Effect through the inhibition of GAPDH, I used KA as a tool to investigate the Warburg Effect. First, I found that GAPDH inhibition with KA results in different biological outcomes

compared to inhibiting glucose uptake. These data suggest that glycolysis could in fact exist in different states within the cell. Given these findings, I next developed an evolved resistance to KA model over a period of 20 weeks. Since acquired resistance to KA occurred independent of alterations in the enzyme target or drug metabolism, I sought to determine the cellular metabolic contribution of acquired resistance to KA. I found that acquired resistant cells evolve a selective pressure to lose the Warburg Effect, but surprisingly remain dependent on glycolysis for survival. Furthermore, I found that as cells evolved to resistance, changes in fatty acid metabolism occurred. These resulting changes allowed acquired resistant cells to become sensitive to the mitochondrial metabolic inhibitors metformin and cerulenin.

Thus, my findings from chapter 3 are important to the field at large because it provides evidence that glucose metabolism does in fact exist in multiple states where cells can either be glucose-dependent and Warburg Effect-independent, or both glucose- and Warburg Effect-dependent with different functional outputs. Therefore, I demonstrate that the Warburg Effect is a different entity from glucose metabolism. While previous studies have shown upregulation of fatty acid metabolism in response to glucose deprivation (Buzzai et al., 2005; DeBerardinis et al., 2008), my study adds an additional layer to show that even in instances where glucose metabolism is indispensable for cell survival, increases in fatty acid metabolism remain a functional metabolic output. Moreover, I demonstrate that cells that were once undergoing the Warburg Effect can lose their ability to sustain aerobic glycolysis, but do not simply switch to oxidative phosphorylation. Rather, they continue undergoing glucose metabolism in a separate

biological state. In addition, it is noteworthy to mention that I was able to measure the temporal dynamics of metabolism in cells as they transitioned into a state away from the Warburg Effect. This measurement likely reflects the metabolic dynamics occurring in the tumor microenvironment given the rapidly changing nutrient availabilities observed *in vivo* in a multitude of studies (Davidson et al., 2016; Hensley et al., 2016; Mayers et al., 2016). Thus, this study advances the field by demonstrating that the Warburg Effect is a real biological phenomenon with separate metabolic properties from glucose metabolism, indicating the clinical importance for continued efforts to identify therapies to target the Warburg Effect.

Chapter 4 used a different angle of targeting the Warburg Effect through therapeutic targeting of 3-phosphoglycerate dehydrogenase (PHGDH), which is the rate-limiting step in serine biosynthesis that diverts glucose flux into serine synthesis at the 3-phosphoglycerate (3PG) step. Inhibition of PHGDH has been shown to have implications for glycolysis (Locasale et al., 2011), but also for nucleotide synthesis (Mullarky et al., 2016; Pacold et al., 2016). In this chapter, my collaborator Qian Wang identified two novel allosteric PHGDH inhibitors through a structure-based approach. Using various experimental techniques including competition assays, docking experiments, mutagenesis assays, and enzymatic activity assays, Qian identified that both inhibitors work well to inhibit PHGDH. Together, we also found that both inhibitors only affected cell proliferation of *PHGDH*-amplified cells, but not *PHGDH*-non-amplified cells. Using CRISPR-*Cas9* technology to genetically knock out (KO) *PHGDH* from cells, I determined that both allosteric inhibitors are highly specific for PHGDH as evidenced by

the differential decrease in cell growth in control cells, but not in *PHGDH* KO cells. I further determined that allosteric inhibition of PHGDH inhibits *de novo* serine synthesis and downstream serine metabolism using steady-state metabolomics and ^{13}C-glucose tracing. Thus, pharmacological inhibition of PHGDH has functional consequences in cells. Qian showed that *PHGDH*-amplified but not *PHGDH*-non-amplified tumors also exhibited sensitivity to both inhibitors.

Our findings from chapter 4 importantly illustrate the potential of PHGDH as a therapeutic target and provide pharmacological tools to better characterize the role of PHGDH in tumor progression. While a functional role of PHGDH to regulate nucleotide pools has been delineated in cancers that contain a *PHGDH* focal amplification, its precise mechanism by which it does so has not been fully resolved. The use of these inhibitors should serve as toolsets for probing the function of PHGDH. In addition, the use of CRISPR-*Cas9* gene knockout technology has been utilized for numerous purposes, mainly to understand the function of a particular gene. This study shows the utility of a genetic knockout system to determine compound specificity for its target, as long as the knockout is not lethal. Given the specificity of the compounds for PHGDH in both cells and tumors, this study contributes knowledge to the field that allosteric inhibition of PHGDH is feasible clinically and that these inhibitors should be further optimized for potential use as anti-cancer therapies.

5.4 Future directions

The work described in this dissertation raises interesting possibilities for future

studies (Figure 5.1). In chapter 2, I show clear evidence for KA efficacy in cancer cells and tumors undergoing the Warburg Effect. I demonstrate that BT-474 tumor progression is suppressed, with some evidence of apoptosis as shown by TUNEL staining. However, these data suggest that apoptosis may not be the only mechanism by which cells are dying in response to KA. Therefore, it is worth elucidating the cell death mechanisms by which cancer and tumor cells respond to KA. There are numerous forms of regulated cell death that have been well-established. Since many cell death mechanisms are linked to metabolic processes, it would be helpful to consider the changes in global metabolite profiles that I gathered in multiple cell lines treated with KA in chapter 2. For example, across multiple cell lines, it appears that there is an increase in reactive oxygen species (ROS) as observed by increases in oxidized to reduced glutathione ratios (GSSG:GSH) and oxidized to reduced nicotinamide adenine dinucleotide phosphate ($NADP^+$:NADPH). Increases in ROS can result in cell death by ferroptosis, defined as regulated cell death by lipid peroxidation (Dixon et al., 2012). It is a phenomenon by which the accumulation of ROS in the form of lipid peroxidases in cells results in depleted reduced glutathione levels, which has been speculated to occur either by inhibition of cystine entry via the cystine/glutamate antiporter system x_c^- or inhibition of glutathione peroxidase 4 (GPX4). Thus, a straightforward way to test whether ferroptosis is occurring in cells treated with KA is to attempt to rescue cells with inhibitors of ferroptosis, such as ferrostatin (Yang and Stockwell, 2016). Although this is just one proposed mode of regulated cell death, a similar approach can be taken to explore other mechanisms as well. While we understand why cells respond to KA (i.e. dependent on the extent of the Warburg Effect), elucidating

the mechanism of cell death will help to answer the question of how cells respond to KA. This knowledge could inform combination therapies in cancer but could also provide insight as to how inhibition of glycolysis communicates with cell death machinery in cells, which remains an area of active research.

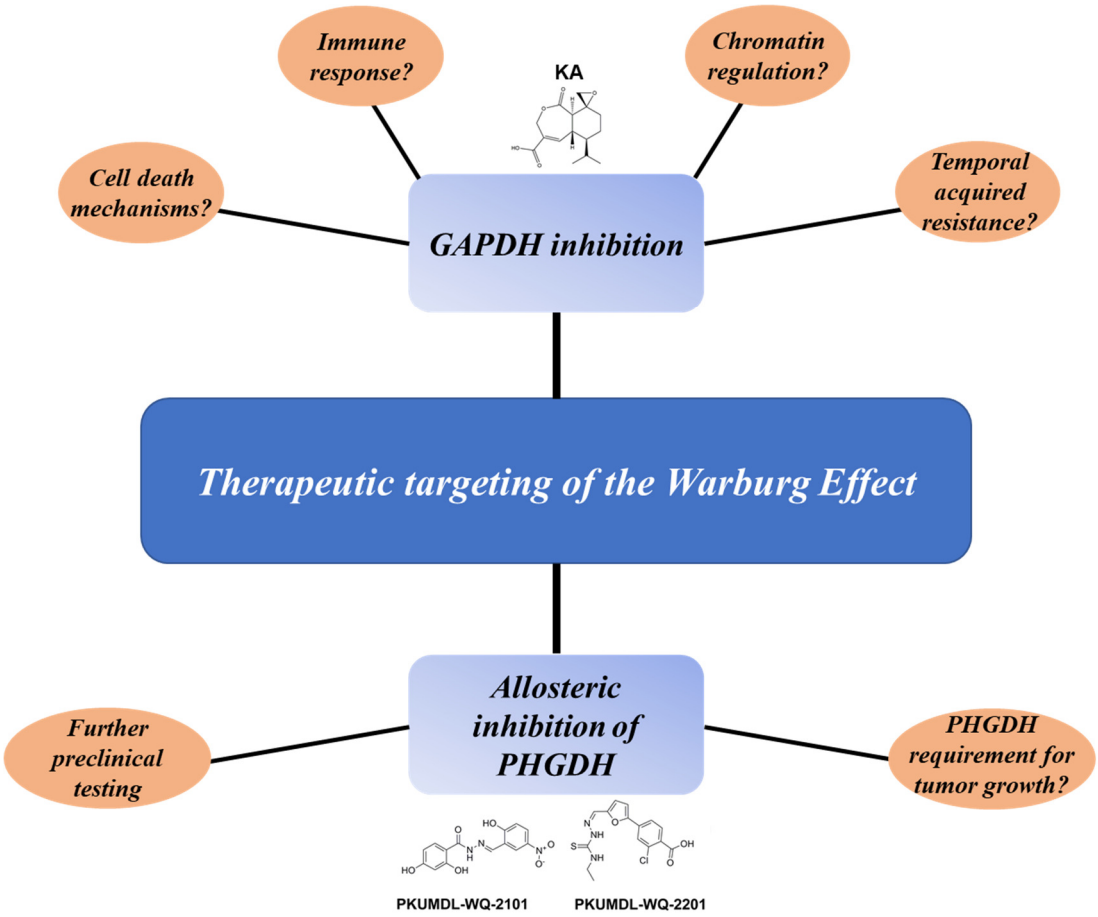

Figure 5.1. Schematic of open questions and future outlook for therapeutic targeting of the Warburg Effect through GAPDH and PHGDH inhibition.
The utility of KA as a specific GAPDH inhibitor allows for a multitude of possible future directions including elucidation of cell death mechanisms, its effects on immune response, its influence on the enhancer landscape, as well as opportunities for combination therapy during resistance. The use of PKUMDL-WQ-2101 and PKUMDL-WQ-2201 as allosteric inhibitors of PHGDH also opens areas for future research including further preclinical testing of the allosteric inhibitors as anti-cancer therapies as well as determining the mechanism by which PHGDH is required for tumor progression. Together, this dissertation provides tools to address active and emerging areas of cancer metabolism research.

Another intriguing possibility is determining how KA affects the immune

response (Figure 5.1), which is important both for KA to be an effective anti-cancer therapy as well as for its relevance in other disease contexts. An interesting study that was recently published showed that GAPDH inhibition with KA exerts anti-inflammatory effects *in vivo* and decreases disease incidence of experimental autoimmune encephalomyelitis (EAE), which is an animal model for multiple sclerosis (MS) (Kornberg et al., 2018). Moreover, in chapter 2 we found that activated CD8+ T cell function, responsible for anti-tumor effects, remained unaffected during treatment of physiological concentrations of KA, but proliferation decreased modestly. While the literature has shown that activated T cells utilize aerobic glycolysis whereas naive T cells depend on oxidative phosphorylation, the metabolic relationship with T cell function and activation is likely more complicated (Chang et al., 2013). Thus, KA can potentially be used as a tool to delineate the metabolic requirements in T cell function for tumor and immune cell crosstalk, as well as for immune modulation for disorders of the immune system such as autoimmune diseases.

Another interesting question that results from the work described in chapter 2 and 3 is how inhibition of the Warburg Effect with KA by GAPDH inhibition influences chromatin regulation (Figure 5.1). Many studies in the field have now shown that there is a clear connection between metabolism and chromatin modulation. Specifically relating to glycolysis, studies have shown that inhibition of ATP citrate lyase (ACLY) (Wellen et al., 2009) and the use of 2-deoxyglucose (2DG) (Cluntun et al., 2015) decrease histone acetylation in a glucose-dependent manner, thus decreasing chromatin accessibility. These studies point to an important role in glucose metabolism and the Warburg Effect

in chromatin biology. To expand from previous literature, it would be worthwhile to understand how inhibiting the Warburg Effect affects the enhancer landscape (i.e. regions of DNA that influence the rate of transcription) through dynamics of histone acetylation marks, particularly histone H3 at lysine 27 (H3K27ac) and mono-methylation of histone H3 at lysine 4 (H3K4me1), which have been shown to be markers of active enhancer regions. Given that I established KA as a tool to specifically target the Warburg Effect, it would be interesting to see the effect that GAPDH inhibition has on histone acetylation in KA-sensitive, intrinsic resistant, and acquired resistant cells and the modifications of enhancer and super enhancer histone acetylation marks, which could be tested using chromatin immunoprecipitation sequencing (ChIP-Seq). This study would address whether inhibition of glycolysis in cells undergoing the Warburg Effect has a larger or lesser effect on enhancer regions compared to cells with low glycolytic rates, which is important for understanding the signaling functions that the Warburg Effect confers.

Given the evolved resistance model that I developed in chapter 3 to understand the fundamental biology around glucose metabolism, it could be of interest to expand the acquired resistant cell lines to encompass a panel of cancer cells in order to understand acquired resistance to KA in a cancer therapeutic context. It is anticipated that different cancer cell lines would acquire resistance to KA at different rates from one another. Therefore, it would be important to monitor the growth rates, check for altered drug metabolism, and isolate clonal populations of resistant cells. To model acquired resistance in a cancer setting, xenografts in mice can be carried out, with subsequent intraperitoneal injections of KA at 1mg/kg, followed by tumor measurements and functional assays of

interest such as metabolomics and transcriptomics. It would also be intriguing to compare these findings with intrinsic resistant KA tumors and tumors expressing the fungal derived KA-resistant *GAPDH* allele, as described in chapter 2. A metabolite profile of these tumors cells could inform useful combination therapies, with cerulenin and metformin from chapter 3 as starting candidate compounds. Further studies with these cancer cells and tumors could test for modifications that occur at the transcriptional level that may influence metabolism, which can be evaluated using RNA-sequencing (RNA-seq). These studies will help further the potential utility of KA as an anti-cancer therapy.

In addition, since environmental factors influence metabolic regulation in cancers, tumor cells are under constant pressure to adapt metabolically to sustain energetic and proliferative demands. Thus, metabolic adaptations are likely occurring during each state of tumor evolution in the tumor's given microenvironment. Recent work has implicated the importance of studying temporal collateral sensitivity as an evolutionary process to resistance in cancers (Zhao et al., 2016). Thus, given the evolved resistance model from chapter 3, it would be worth understanding temporal acquired resistance from a metabolic level (Figure 5.1). This could be done by identifying metabolic vulnerabilities that emerge temporally as KA-sensitive cells acquire resistance to KA using 2D and 3D cell culture models to start. Based on these data, xenograft models could be utilized to model early, intermediate, and late-stage acquired resistance to KA, followed by metabolomics at each stage of resistance. Comparisons of metabolite profiles as tumors progress to resistance could provide insight for biomarkers to predict resistance to KA as well as therapeutic targets for collateral sensitivity to prevent late-stage acquired resistance. The application

of this study could be channeled more broadly to other areas of acquired resistance to metabolic therapy as it will likely demonstrate the importance of using metabolic factors as a determinant for not only predicting therapy efficacy, but also for predicting modes of resistance.

The work described in chapter 4 opens several areas for possible future research (Figure 5.1). Firstly, the allosteric inhibitors of PHGDH have been confirmed to be on target with efficacy against *PHGDH*-amplified, but not *PHGDH*-non-amplified cancer cells and tumors, making them suitable candidates for further preclinical testing. Future work with these allosteric inhibitors might involve derivatization to improve IC_{50} values for sensitive cells and *in vivo* efficacy. In addition, there have been numerous proposed mechanisms for the requirement of PHGDH in tumor progression. One mechanism is that PHGDH promotes nucleotide synthesis through regulating one-carbon units (Pacold et al., 2016). Another proposed mechanism of PHGDH is anaplerosis of the TCA cycle through the transamination reaction of glutamate to alpha-ketoglutarate (αKG) (Possemato et al., 2011). Thus, more work is necessary to delineate the precise mechanism of how PHGDH regulates tumor growth. I suspect that one possibility, based on my ^{13}C-glucose tracing data upon PHGDH inhibition, is that the pentose phosphate pathway (PPP) is involved in regulating nucleotide synthesis. I showed significant decreases in the m+5 peak of both pyrimidines and purines after PHGDH inhibition, indicating a possible role of PHGDH in regulating nucleotide synthesis through ribose. Thus, my metabolite data and the described allosteric PHGDH inhibitors will be useful tools for delineating this possible mechanism as well as other potential mechanisms for

regulating tumor growth.

Altogether, this dissertation provides rationale for future studies to continue exploring the functions and therapeutic possibilities of targeting the Warburg Effect.

5.5 References

Bakker, B.M., Westerhoff, H.V., Opperdoes, F.R., and Michels, P.A. (2000). Metabolic control analysis of glycolysis in trypanosomes as an approach to improve selectivity and effectiveness of drugs. Molecular and biochemical parasitology *106*, 1-10.

Ben-Haim, S., and Ell, P. (2009). 18F-FDG PET and PET/CT in the evaluation of cancer treatment response. Journal of Nuclear Medicine *50*, 88-99.

Buzzai, M., Bauer, D.E., Jones, R.G., DeBerardinis, R.J., Hatzivassiliou, G., Elstrom, R.L., and Thompson, C.B. (2005). The glucose dependence of Akt-transformed cells can be reversed by pharmacologic activation of fatty acid β-oxidation. Oncogene *24*, 4165.

Chang, C.H., Curtis, J.D., Maggi, L.B., Jr., Faubert, B., Villarino, A.V., O'Sullivan, D., Huang, S.C., van der Windt, G.J., Blagih, J., Qiu, J.*, et al.* (2013). Posttranscriptional control of T cell effector function by aerobic glycolysis. Cell *153*, 1239-1251.

Cluntun, A.A., Huang, H., Dai, L., Liu, X., Zhao, Y., and Locasale, J.W. (2015). The rate of glycolysis quantitatively mediates specific histone acetylation sites. Cancer Metab *3*, 10.

Davidson, S.M., Papagiannakopoulos, T., Olenchock, B.A., Heyman, J.E., Keibler, M.A., Luengo, A., Bauer, M.R., Jha, A.K., O'Brien, J.P., Pierce, K.A.*, et al.* (2016). Environment Impacts the Metabolic Dependencies of Ras-Driven Non-Small Cell Lung Cancer. Cell Metab *23*, 517-528.

DeBerardinis, R.J., Lum, J.J., Hatzivassiliou, G., and Thompson, C.B. (2008). The biology of cancer: metabolic reprogramming fuels cell growth and proliferation. Cell Metab *7*, 11-20.

Dixon, S.J., Lemberg, K.M., Lamprecht, M.R., Skouta, R., Zaitsev, E.M., Gleason, C.E., Patel, D.N., Bauer, A.J., Cantley, A.M., and Yang, W.S. (2012). Ferroptosis: an iron-dependent form of nonapoptotic cell death. Cell *149*, 1060-1072.

Galluzzi, L., Kepp, O., Vander Heiden, M.G., and Kroemer, G. (2013). Metabolic targets for cancer therapy. Nat Rev Drug Discov *12*, 829-846.

Hay, N. (2016). Reprogramming glucose metabolism in cancer: can it be exploited for cancer therapy? Nature Reviews Cancer.

Hensley, C.T., Faubert, B., Yuan, Q., Lev-Cohain, N., Jin, E., Kim, J., Jiang, L., Ko, B., Skelton, R., and Loudat, L. (2016). Metabolic heterogeneity in human lung tumors. Cell *164*, 681-694.

Kornberg, M.D., Bhargava, P., Kim, P.M., Putluri, V., Snowman, A.M., Putluri, N., Calabresi, P.A., and Snyder, S.H. (2018). Dimethyl fumarate targets GAPDH and aerobic glycolysis to modulate immunity. Science *360*, 449-453.

Locasale, J.W., Grassian, A.R., Melman, T., Lyssiotis, C.A., Mattaini, K.R., Bass, A.J., Heffron, G., Metallo, C.M., Muranen, T., Sharfi, H.*, et al.* (2011). Phosphoglycerate dehydrogenase diverts glycolytic flux and contributes to oncogenesis. Nat Genet *43*, 869-874.

Luengo, A., Gui, D.Y., and Vander Heiden, M.G. (2017). Targeting Metabolism for Cancer Therapy. Cell Chem Biol *24*, 1161-1180.

Mayers, J.R., Torrence, M.E., Danai, L.V., Papagiannakopoulos, T., Davidson, S.M., Bauer, M.R., Lau, A.N., Ji, B.W., Dixit, P.D., Hosios, A.M.*, et al.* (2016). Tissue of origin

dictates branched-chain amino acid metabolism in mutant Kras-driven cancers. Science *353*, 1161-1165.
Mullarky, E., Lucki, N.C., Beheshti Zavareh, R., Anglin, J.L., Gomes, A.P., Nicolay, B.N., Wong, J.C., Christen, S., Takahashi, H., Singh, P.K.*, et al.* (2016). Identification of a small molecule inhibitor of 3-phosphoglycerate dehydrogenase to target serine biosynthesis in cancers. Proceedings of the National Academy of Sciences of the United States of America *113*, 1778-1783.
Pacold, M.E., Brimacombe, K.R., Chan, S.H., Rohde, J.M., Lewis, C.A., Swier, L.J., Possemato, R., Chen, W.W., Sullivan, L.B., and Fiske, B.P. (2016). A PHGDH inhibitor reveals coordination of serine synthesis and one-carbon unit fate. Nature chemical biology.
Possemato, R., Marks, K.M., Shaul, Y.D., Pacold, M.E., Kim, D., Birsoy, K., Sethumadhavan, S., Woo, H.K., Jang, H.G., Jha, A.K.*, et al.* (2011). Functional genomics reveal that the serine synthesis pathway is essential in breast cancer. Nature *476*, 346-350.
Shestov, A.A., Liu, X., Ser, Z., Cluntun, A.A., Hung, Y.P., Huang, L., Kim, D., Le, A., Yellen, G., Albeck, J.G.*, et al.* (2014). Quantitative determinants of aerobic glycolysis identify flux through the enzyme GAPDH as a limiting step. Elife *3*, e03342.
Vander Heiden, M.G. (2011). Targeting cancer metabolism: a therapeutic window opens. Nat Rev Drug Discov *10*, 671-684.
Vander Heiden, M.G. (2013). Exploiting tumor metabolism: challenges for clinical translation. J Clin Invest *123*, 3648-3651.
Vander Heiden, M.G., Cantley, L.C., and Thompson, C.B. (2009). Understanding the Warburg effect: the metabolic requirements of cell proliferation. Science *324*, 1029-1033.
Warburg, O. (1956). On the origin of cancer cells. Science *123*, 309-314.
Warburg, O., Wind, F., and Negelein, E. (1927). The Metabolism of Tumors in the Body. J Gen Physiol *8*, 519-530.
Wellen, K.E., Hatzivassiliou, G., Sachdeva, U.M., Bui, T.V., Cross, J.R., and Thompson, C.B. (2009). ATP-citrate lyase links cellular metabolism to histone acetylation. Science *324*, 1076-1080.
Yang, W.S., and Stockwell, B.R. (2016). Ferroptosis: death by lipid peroxidation. Trends in cell biology *26*, 165-176.
Zhao, B., Sedlak, J.C., Srinivas, R., Creixell, P., Pritchard, J.R., Tidor, B., Lauffenburger, D.A., and Hemann, M.T. (2016). Exploiting Temporal Collateral Sensitivity in Tumor Clonal Evolution. Cell *165*, 234-246.

Figure A1.S1 (*Related to Figure 2.2)* - Glycolysis and branching pathways are altered after treatment with KA.

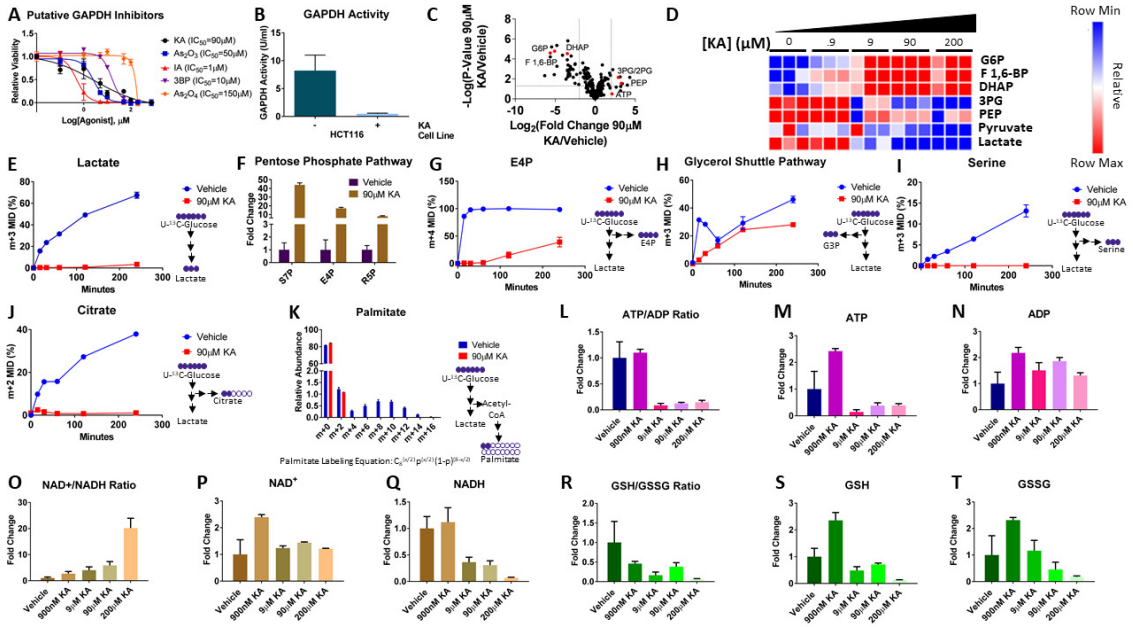

(A) Dose-response curve showing relative viability in HCT116 cells after treatment. 0-200μM koningic acid (KA); 0-200μM iodoacetate (IA); 0-200μM 3-bromopyruvate (3BP); 0-500μM arsenic trioxide (As_2O_3); 0-200μM arsenate (As_2O_4). **(B)** Relative GAPDH activity in HCT116 cells in response to vehicle (DMSO) or IC_{50} (90μM) KA (n=2). **(C)** Volcano plot showing metabolic profile of HCT116 cells treated with vehicle or 90μM KA. Log_2 fold change versus $-log_{10}$ (p-value). Glycolysis and related metabolites shown as red points. **(D)** Clustered heatmap with metabolite and dose annotations of dose-dependent glycolysis response to 90μM KA. **(E)** ^{13}C-Lactate. **(F)**

Pentose Phosphate Pathway levels. **(G)** ^{13}C-E4P. **(H)** ^{13}C-G3P. **(I)** ^{13}C-Serine. **(J)** ^{13}C-Citrate. **(K)** ^{13}C-Palmitate. **(L)** ATP to ADP ratio in response to 6-hour treatment with 0-200μM KA. **(M)** Relative ATP levels. **(N)** Relative ADP levels. **(O)** NAD^+ to NADH ratio. **(P)** Relative NAD^+ levels. **(Q)** Relative NADH levels. **(R)** Reduced to oxidized glutathione (GSH to GSSG) ratio. **(S)** Relative GSH levels. **(T)** Relative GSSG levels.

G6P, glucose-6-phosphate; F 1,6-BP, fructose 1,6-bisphosphate; DHAP, dihydroxyacetone phosphate; GA3P, glyceraldehyde-3-phosphate; 1,3-BPG, 1,3-bisphosphoglycerate; 3PG, 3-phosphoglycerate; PEP, phosphoenolpyruvate; S7P, sedoheptulose-7-phosphate; E4P, erythrose-4-phosphate; R5P, ribose-5-phosphate.
Data points are represented as mean ±SEM from n=3 biological replicates.

Figure A1.S2 ***(Related to Figure 2.3)*** **- Expression of *T. koningii* KA-resistant GAPDH allele in HCT116 cells rescues cell viability and metabolic alterations after KA treatment.**

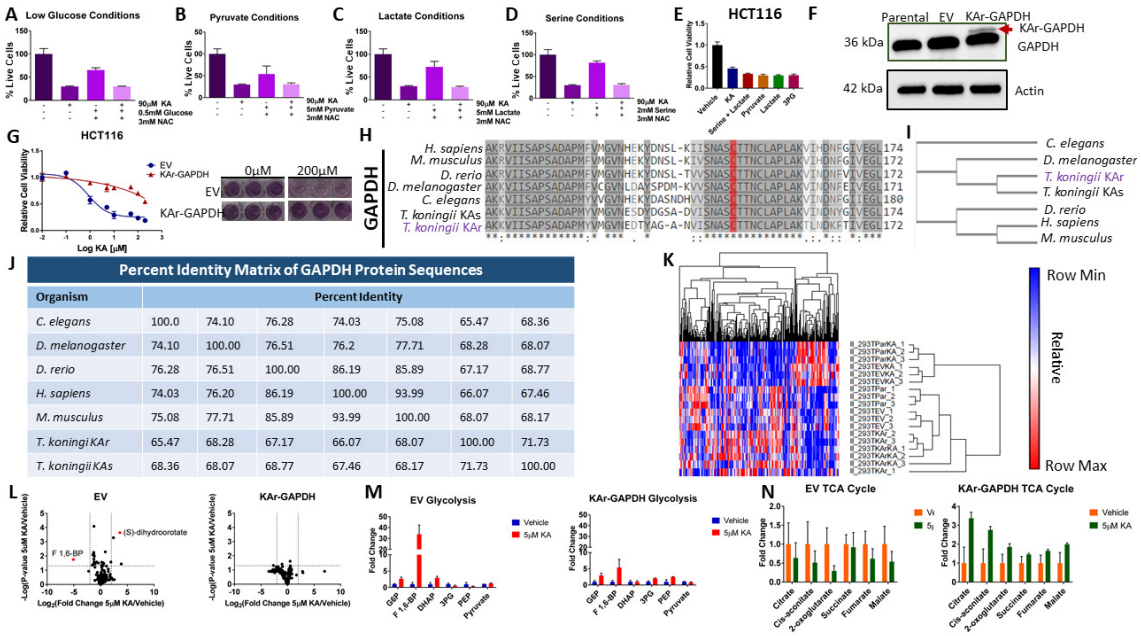

Organism	Percent Identity						
C. elegans	100.0	74.10	76.28	74.03	75.08	65.47	68.36
D. melanogaster	74.10	100.00	76.51	76.2	77.71	68.28	68.07
D. rerio	76.28	76.51	100.00	86.19	85.89	67.17	68.77
H. sapiens	74.03	76.20	86.19	100.00	93.99	66.07	67.46
M. musculus	75.08	77.71	85.89	93.99	100.00	68.07	68.17
T. koningii KAr	65.47	68.28	67.17	66.07	68.07	100.00	71.73
T. koningii KAs	68.36	68.07	68.77	67.46	68.17	71.73	100.00

(A) Media supplemented with 0.5mM glucose and/or 3mM N-acetylcysteine (NAC) with or without KA treatment in HCT116 cells. **(B)** Media supplemented with 5mM pyruvate and/or 3mM NAC as in (A). **(C)** Media supplemented with 5mM lactate and/or 3mM NAC as in (A). **(D)** Media supplemented with 2mM serine and/or 3mM NAC as in (A). **(E)** Media supplemented with 2mM serine + 5mM lactate, 5mM pyruvate, 5mM lactate, or 2mM 3-phosphoglycerate (3PG) with KA treatment. **(F)** Immunoblotting of parental, EV or KAr-GAPDH expressing HCT116 cells. **(G)** Cell viability of HCT116 cells expressing KAr-GAPDH or EV (left). Representative images of well (right) KAr-GAPDH or EV expressing cells treated with vehicle (0μM) or KA (200μM). **(H)** Multiple

sequence alignment of GAPDH protein sequence across different species. **(I)** Phylogenetic analysis of GAPDH among different species. **(J)** Table depicting the percent identity matrix of GAPDH protein sequence across different species. **(K)** Heat map showing global metabolic dynamics in response to vehicle or KA treatment in HCT116 parental, HCT116 EV, and HCT116 KAr-GAPDH overexpressed cells. **(L)** Volcano plots showing metabolite profiles of HCT116 cells expressing EV compared to those expressing KAr-GAPDH after treatment with DMSO or 5μM KA. Log_2 fold change versus $-log_{10}$ (p-value). Dotted lines along x-axis represent $\pm log_2(2)$ fold change and dotted line along y-axis represents $-log_{10}(0.05)$. Glycolysis metabolites shown as red points. All other metabolites are black points (n=3). **(M)** Glycolytic metabolite levels. **(N)** TCA cycle metabolite levels.

G6P, glucose-6-phosphate; F 1,6-BP, fructose 1,6-bisphosphate; DHAP, dihydroxyacetone phosphate; GA3P, glyceraldehyde-3-phosphate; 1,3-BPG, 1,3-bisphosphoglycerate; 3PG, 3-phosphoglycerate; PEP, phosphoenolpyruvate.

Data points are represented as mean ±SEM from n=3 biological replicates.

Figure A1.S3 ***(Related to Figure 2.4)*** **- KA treatment reveals metabolic heterogeneity among NCI-60 cell line panel.**

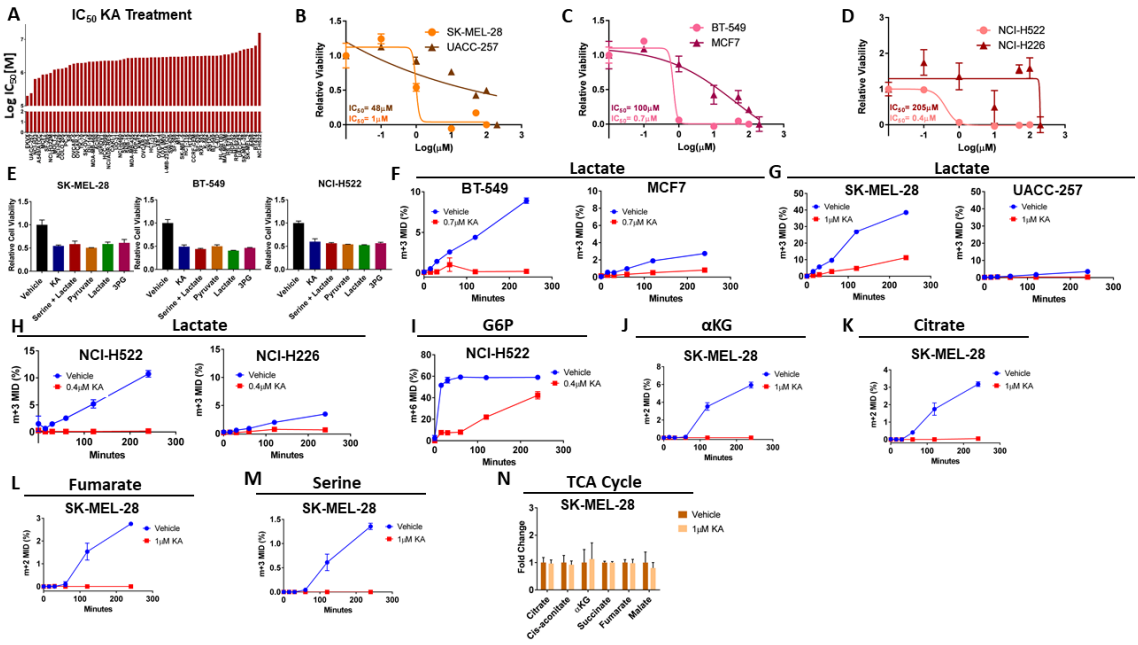

(A) Waterfall plot showing KA concentrations at which 50% of growth is inhibited (IC_{50}) among 60 independent cell lines. **(B)** SK-MEL-28 and UACC-257 melanoma cancer cells dose-response curve after treatment with 0-200μM KA. **(C)** BT-549 and MCF7 breast cancer cells as in (B). **(D)** NCI-H522 and NCI-H226 non-small cell lung cancer (NSCLC) cells as in (B). **(E)** Media supplemented with 2mM serine + 5mM lactate, 5mM pyruvate, 5mM lactate, or 2mM 3-phosphoglycerate (3PG) with KA treatment in KA-sensitive cells. **(F)** ^{13}C-Lactate in breast cancer cell lines treated with vehicle or 0.7μM KA. **(G)** ^{13}C-Lactate in melanoma cancer cells treated with vehicle or 1μM KA. **(H)** ^{13}C-Lactate in NSCLC cell lines treated with vehicle or 0.4μM KA. **(I)** ^{13}C-G6P in NCI-H522 cell lines treated with vehicle or 0.4μM KA. **(J)** ^{13}C-αKG in SK-MEL-28 cells. **(K)** ^{13}C-

Citrate in SK-MEL-28 cells. **(L)** ^{13}C-Fumarate in SK-MEL-28 cells. **(M)** ^{13}C-Serine in SK-MEL-28 cells. **(N)** TCA metabolite levels in SK-MEL-28 cells.

G6P, glucose-6-phosphate; αKG, alpha-ketoglutarate.

Data are represented as mean ±SEM with n=3 biological replicates.

Figure A1.S4 ***(Related to Figure 2.4)*** **- The cytotoxic response to KA treatment is heterogeneous.**

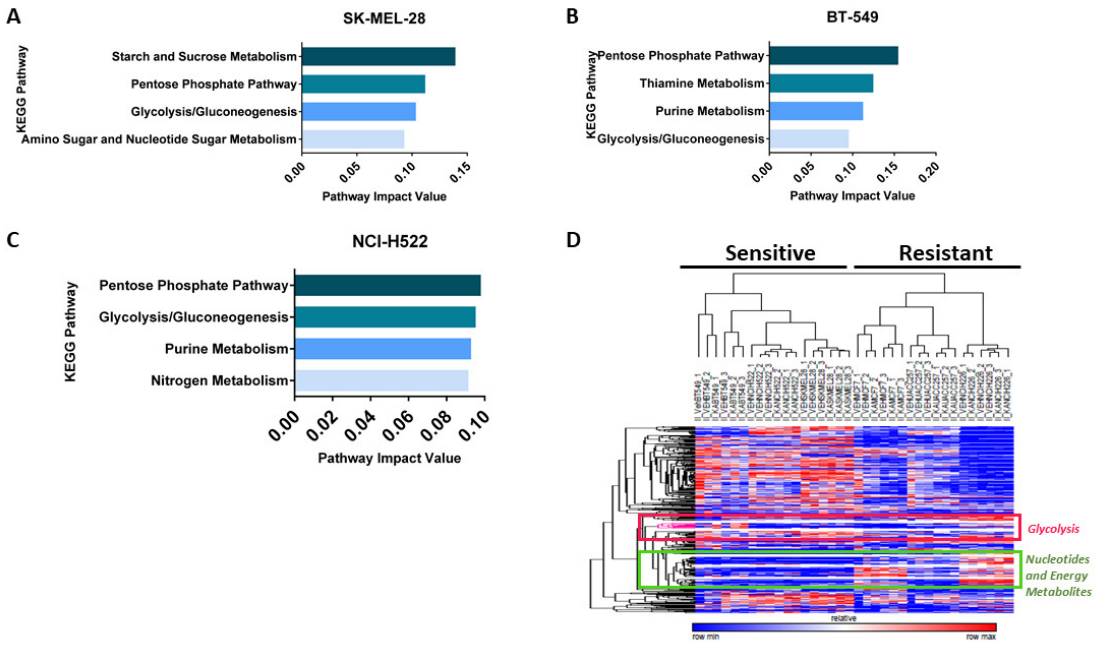

(A) Pathway analysis in BT-549 showing top 4 highest scoring pathways in response to KA. **(B)** Pathway analysis in SK-MEL-28 as shown in (A). **(C)** Pathway analysis in NCI-H522 as shown in (A). **(D)** Clustered heatmaps in KA-sensitive and resistant cells with pathway annotations of dose-dependent global metabolic responses to KA.

Figure A1.S5 ***(Related to Figure 2.5)*** **- Mutational, copy number alteration (CNA), and gene expression do not correlate with KA response and resistance.**

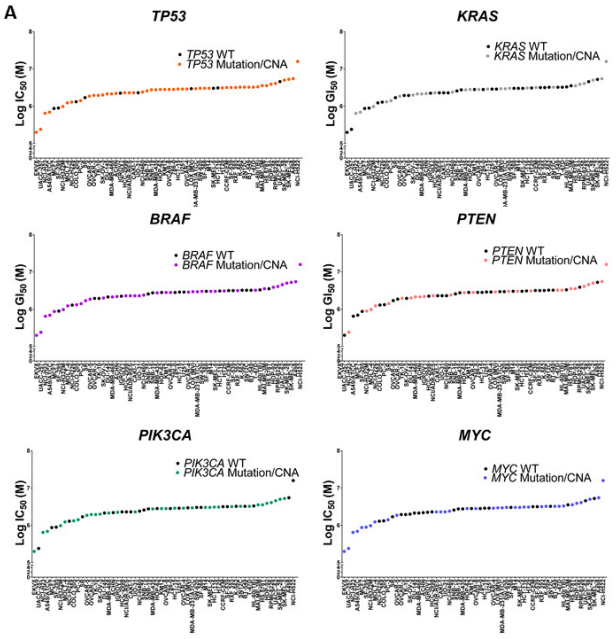

B

GSEA Ranked Order Core Enrichment Results

Probe	Rank in Gene List	Rank Metric Score	Running ES
HK2	1140	.196	.0928
PKLR	2199	.141	.1487
ALDOC	2349	.135	.2433
BPGM	4149	.079	.2171
PFKM	4465	.071	.2556

(A) Mutational and copy number alteration (CNA) of commonly altered oncogenes and tumor suppressor genes correlated with KA IC_{50} response across NCI-60 cell line panel. **(B)** Gene set enrichment analysis (GSEA) core enrichment results for statistically significant glycolysis genes across KA-sensitive and KA-resistant cell lines from NCI-60 cell line panel.

HK2, hexokinase 2; PKLR, red cell/liver pyruvate kinase; ALDOC, aldolase C; BPGM, bisphosphoglycerate mutase; PFKM, phosphofructokinase.

Figure A1.S6 *(Related to Figure 2.6)* - BT-474 cells are sensitive and MDA-MB-231 cells are resistant to KA treatment.

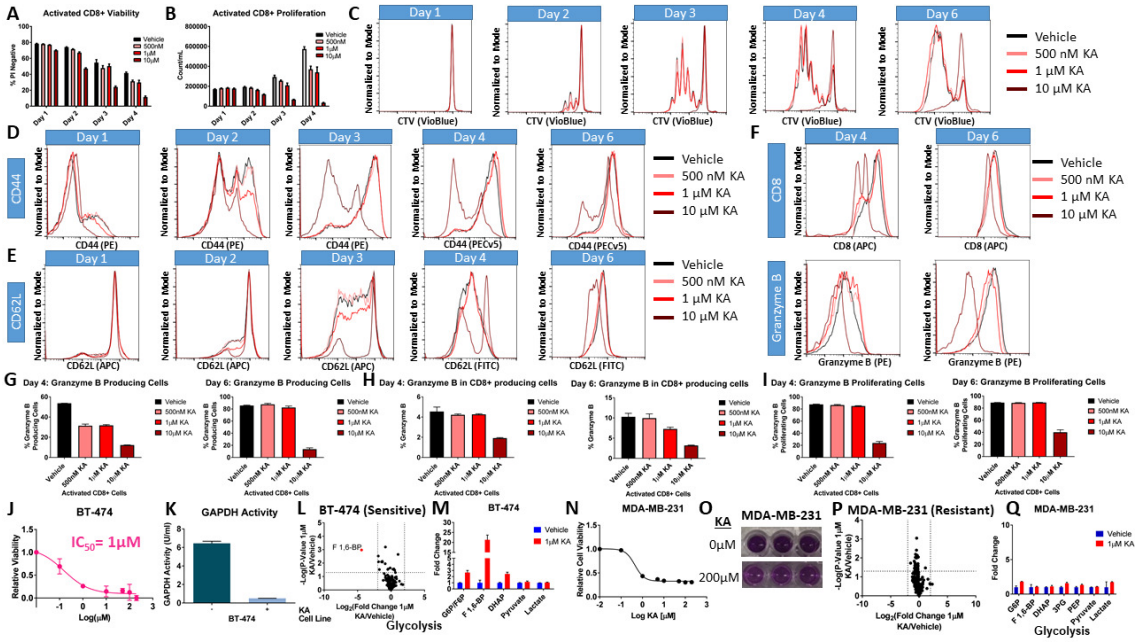

(A) Relative viability in activated CD8+ cells after treatment with 0-10µM KA. **(B)** Relative cell proliferation in activated CD8+ cells after treatment with 0-10µM KA. **(C)** Proliferation over 6 days in the presence of 0-10µM KA. **(D)** CD44 surface markers of activation over 6 days in the presence of 0-10µM KA. **(E)** CD62L surface markers of activation over 6 days in the presence of 0-10µM KA. **(F)** Granzyme B production in CD8+ cells at days 4 and 6. **(G)** Percent of granzyme B producing cells in response to 0-10µM KA at days 4 and 6. **(H)** Percent of granzyme B in CD8+ producing cells at days 4 and 6. **(I)** Percent of granzyme B proliferating cells in response to 0-10µM KA. **(J)** Dose-response curve showing relative viability in BT-474 breast cancer cells after treatment with 0-200µM KA. **(K)** GAPDH activity assay showing relative GAPDH

activity in BT-474 KA-sensitive cells treated with 1μM KA (n=2). **(L)** Volcano plot showing metabolic profile from BT-474 cells treated with vehicle or 1μM KA. Log_2 fold change versus $-log_{10}$ (p-value). Dotted lines along x-axis represent $\pm log_2(2)$ fold change and dotted line along y-axis represents $-log_{10}(0.05)$. Significantly different metabolites shown as red points. All other metabolites are black points. **(M)** Glycolysis profile from BT-474 cells. **(N)** Dose-response curve showing relative viability in MDA-MB-231 breast cancer cells after treatment with 0-200μM KA. **(O)** Representative images of wells (bottom left, top right) with MDA-MB-231 cells treated with vehicle (0μM) or KA (200μM). **(P)** Volcano plot showing metabolic profile from MDA-MB-231 cells treated with vehicle or 1μM KA. Log_2 fold change versus $-log_{10}$ (p-value). Dotted lines along x-axis represent $\pm log_2(2)$ fold change and dotted line along y-axis represents $-log_{10}(0.05)$. Significantly different metabolites shown as red points. All other metabolites are black points. **(Q)** Glycolysis profile from MDA-MB-231 cells.

G6P, glucose-6-phosphate; F 1,6-BP, fructose 1,6-bisphosphate; DHAP, dihydroxyacetone phosphate; GA3P, glyceraldehyde-3-phosphate; 1,3-BPG, 1,3-bisphosphoglycerate; 3PG, 3-phosphoglycerate; PEP, phosphoenolpyruvate.

Data are represented as mean ±SEM with n=3 biological replicates unless indicated otherwise.

Figure A1.S7 ***(Related to Figure 2.7)*** **- KA treatment suppresses BT-474 breast cancer tumor growth and disrupts energy status and redox potential.**

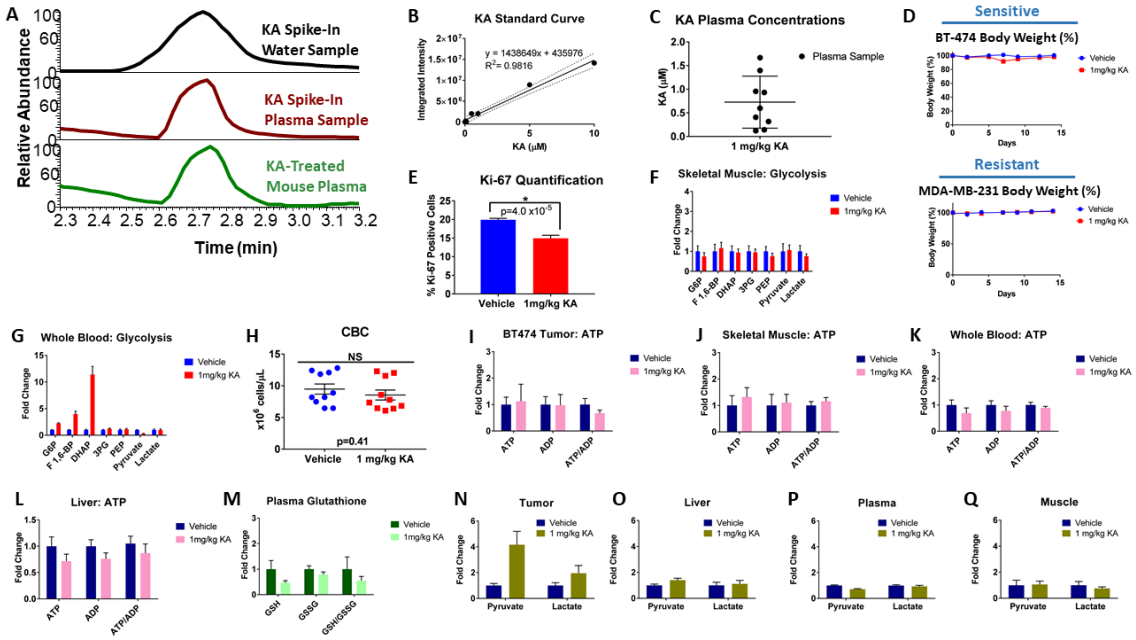

(A) Mass spectra of KA in water and plasma from BT-474 tumor study using liquid chromatography-mass spectrometry (LC-MS) with a representative KA plasma sample. **(B)** Standard curve of KA spiked into untreated plasma samples. **(C)** KA plasma concentrations from BT-474 mouse plasma samples (n=9). **(D)** Body weight percentage of KA-sensitive BT-474 and KA-resistant MDA-MB-231 tumor models (n=10 per group). **(E)** Quantification of Ki67 staining for cell proliferation from vehicle and 1mg/kg KA treated BT-474 tumors (n=3 per group). Data are represented as mean ±SEM from 3 representative sections of each tumor. **(F)** Glycolysis profile from skeletal muscle in BT-474 study (n=10 per group). **(G)** Glycolysis profile from whole blood in BT-474 study (n=10 for vehicle group; n=9 for treatment group). **(H)** Complete blood count (CBC)

from whole blood of MDA-MB-231 tumor study. **(I)** ATP, ADP, and ATP to ADP ratio in BT-474 tumor (n=10 per group). **(J)** ATP, ADP, and ATP to ADP ratio in skeletal muscle from BT-474 tumor study (n=10 per group). **(K)** ATP, ADP, and ATP to ADP ratio in whole blood from BT-474 tumor study (n=10 for vehicle group; n=9 for treatment group). **(L)** ATP, ADP, and ATP to ADP ratio in liver from BT-474 tumor study (n=10 per group). **(M)** GSH, GSSG, and GSH to GSSG ratio in plasma from BT-474 tumor study (n=10 per group). **(N)** Pyruvate and lactate levels in BT-474 tumors (n=7 for vehicle group; n=8 for treatment group). **(O)** Pyruvate and lactate levels in liver from BT-474 tumor study (n=10 per group). **(P)** Pyruvate and lactate levels in plasma from BT-474 tumor study (n=10 per group). **(Q)** Pyruvate and lactate levels in skeletal muscle from BT-474 tumor study (n=10 per group).

G6P, glucose-6-phosphate; F 1,6-BP, fructose 1,6-bisphosphate; DHAP, dihydroxyacetone phosphate; GA3P, glyceraldehyde-3-phosphate; 1,3-BPG, 1,3-bisphosphoglycerate; 3PG, 3-phosphoglycerate; PEP, phosphoenolpyruvate.

Data are represented as mean ±SEM from n = 3 independent measurements unless otherwise noted. *p<0.05, **p<0.01, ***p<0.001, ****p<0.0001 as determined by two-way ANOVA.

Figure A2.S1 ***(Related to Figure 3.1)*** **- GAPDH inhibition leads to different outcomes from targeting glucose uptake.**

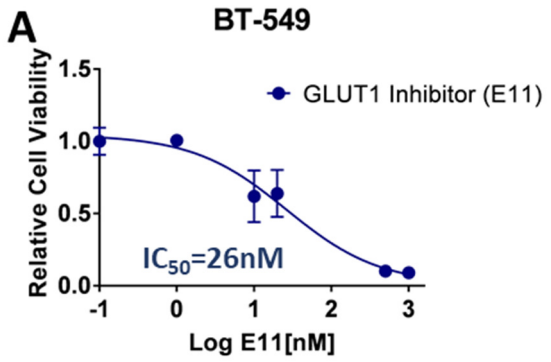

(A) BT-549 breast cancer cells dose-response curve after treatment with 0-1μM E11 for 24 hours.

All data are represented as mean ± SEM from n=3 biological replicates.

*p<0.05, **p<0.01, ***p<0.001, ****p<0.0001 as determined Two-Way ANOVA.

Figure A2.S2 ***(Related to Figure 3.2)*** **- Cells evolve resistance to GAPDH inhibition independent of drug metabolism.**

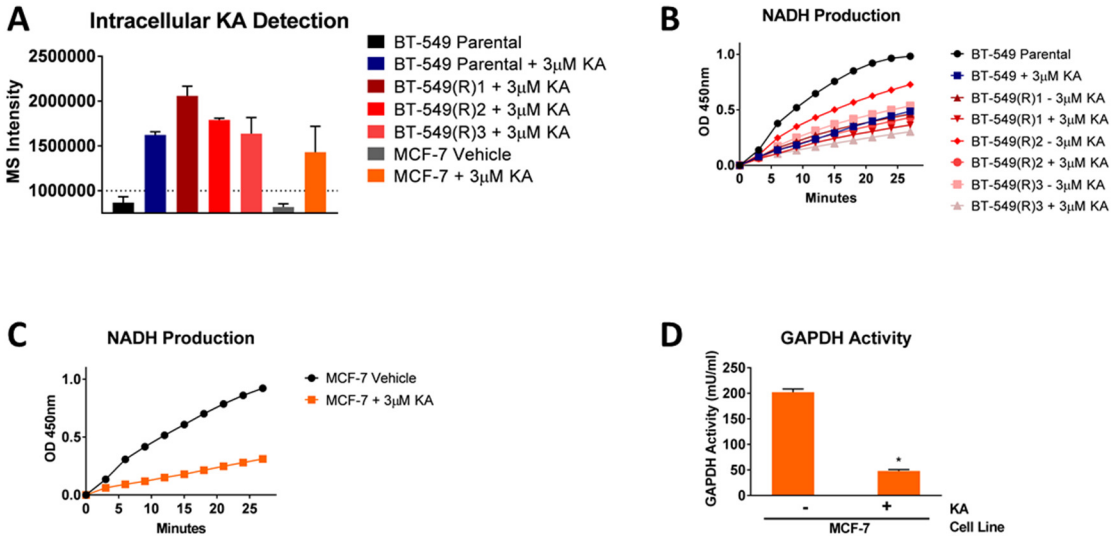

(A) Mass spectrometry intensities of intracellular KA in vehicle or KA (3μM) treated cells using liquid chromatography-mass spectrometry (LC-MS). Dotted line denotes noise level. **(B)** Relative NADH production from 0-27 minutes in kinetic mode of BT-549 parental and acquired resistant cells with and without KA (3μM) treatment (n=2). **(C)** Relative NADH production of MCF-7 cells as in (B) (n=2). **(D)** Relative GAPDH activity in MCF-7 cells in response to vehicle or 3μM KA (n=2).

All data are represented as mean ± SEM from n=3 biological replicates unless otherwise indicated.

*p<0.05, **p<0.01, ***p<0.001, ****p<0.0001 as determined by student's t-test.

Figure A2.S3 ***(Related to Figure 3.3)*** **- Acquired resistant cells remain dependent on glycolysis, but lose the Warburg Effect.**

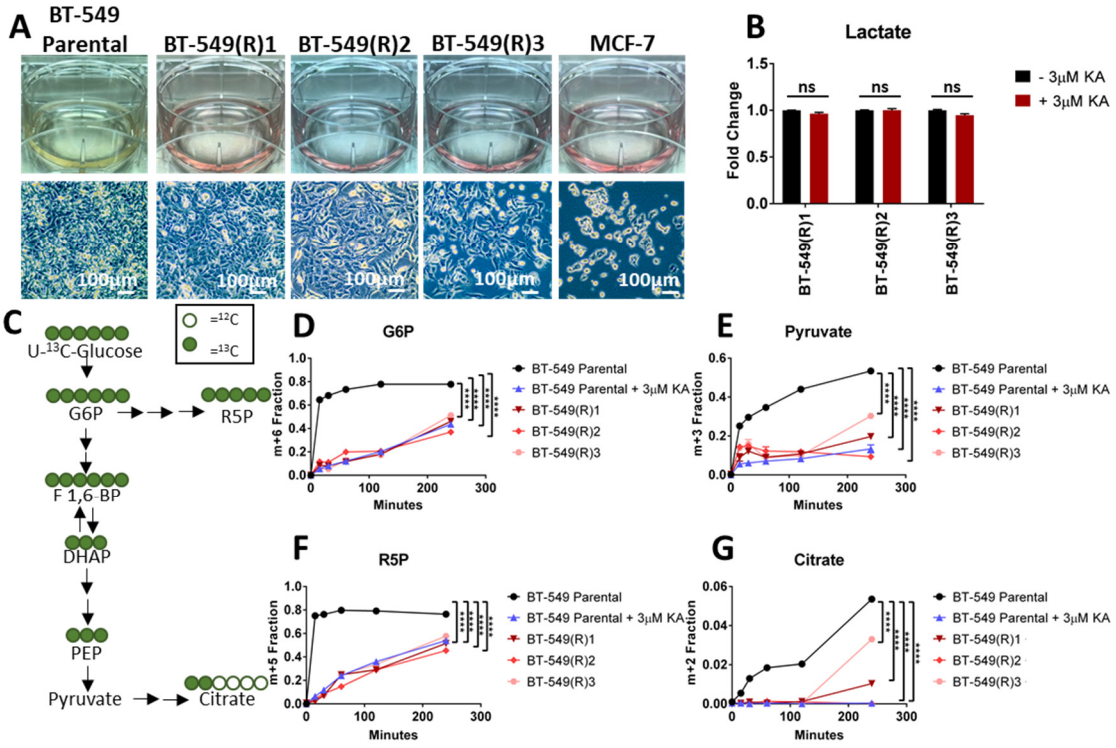

(A) Representative images of spent media (top row) and cells (bottom row) at confluency in BT-549 parental, BT-549 acquired resistant, and MCF-7 intrinsic resistant cells after 48 hours. **(B)** Lactate levels in BT-549 acquired resistant cells upon removal or maintained in KA (3µM) KA after 24 hours. Not significant denoted as "ns" determined by multiple t-tests. **(C)** Schematic of (U-^{13}C)-glucose labeling in glycolysis, pentose phosphate pathway, and the citric acid (TCA) cycle. **(D)** ^{13}C-G6P in BT-549 parental and acquired resistant cells treated with vehicle or KA for 0-4 hours. **(E)** ^{13}C-pyruvate as in (D). **(F)** ^{13}C-R5P as in (D). **(G)** ^{13}C-citrate as in (D).

G6P, glucose-6-phosphate; F 1,6-BP, fructose 1,6-bisphosphate; R5P, ribose-5-phosphate.

All data are represented as mean ± SEM from n=3 biological replicates.

*p<0.05, **p<0.01, ***p<0.001, ****p<0.0001 as determined by Two-Way ANOVA unless otherwise indicated.

Figure A2.S4 ***(Related to Figure 3.5)*** **- Changes in fatty acid metabolism emerge as a functional output of evolved resistance to KA.**

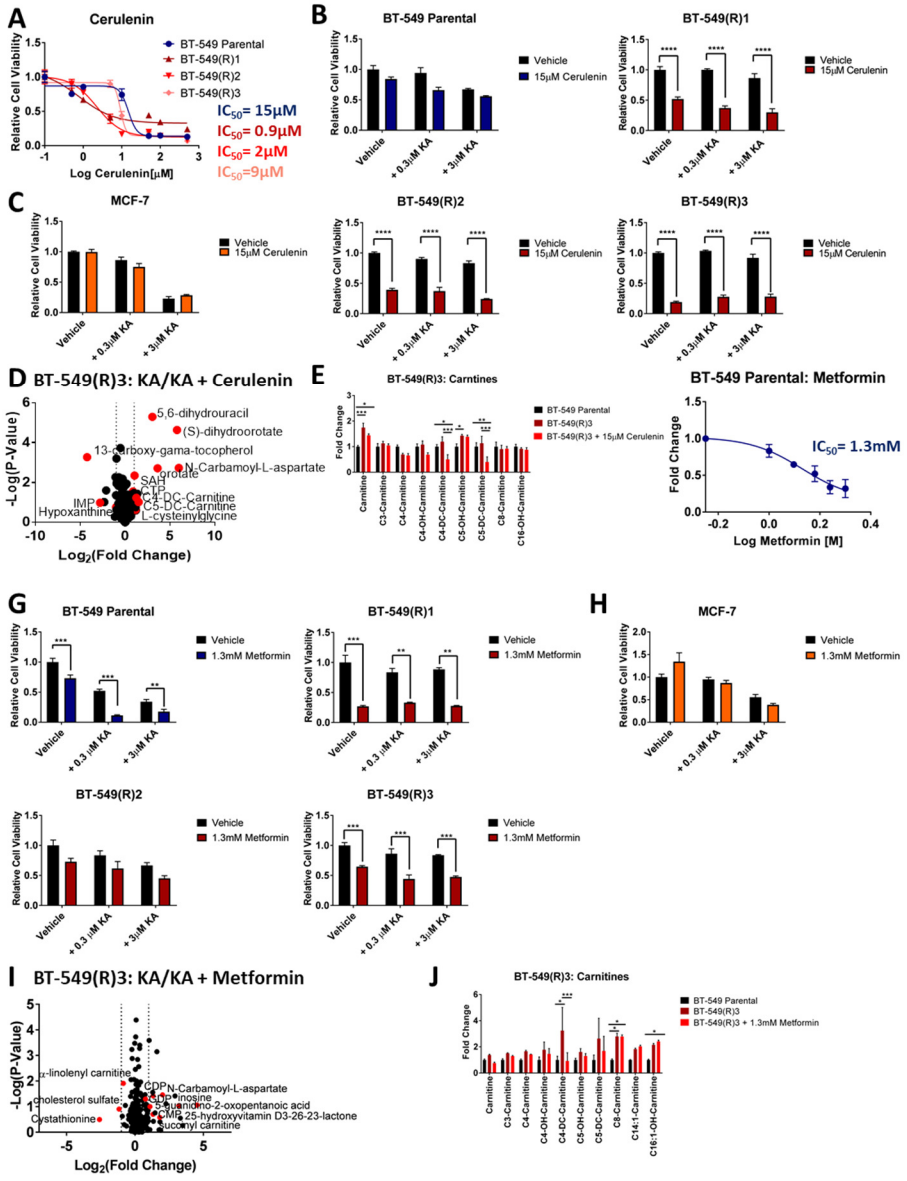

(A) BT-549 parental and acquired resistant cells dose-response curve treated with 0-500μM cerulenin for 24 hours. **(B)** Cell viability of BT-549 parental cells and acquired

resistant cells treated with cerulenin (15μM) with or without KA (0.3μM or 3μM) for 24 hours. **(C)** Cell viability of MCF-7 cells as in (B). **(D)** Volcano plot showing metabolite profiles of BT-549 acquired resistant (R)3 cells maintained in KA (3μM) with or without cerulenin (15μM). Log_2 fold change versus $-log_{10}$ p-value. Dotted lines along x-axis represent ± $log_2(1)$ fold change and dotted line along y-axis represents $-log_{10}(0.05)$. Metabolites ± $log_2(1)$ fold change shown as red points with metabolite names denoted. All other metabolites are black points. **(E)** Acyl-carnitine levels in BT-549 acquired resistant (R)3 cells maintained in KA (3μM) and treated with or without cerulenin (15μM) for 6 hours. **(F)** BT-549 parental cell dose-response curve treated with 0-2mM metformin for 24 hours. **(G)** Cell viability of BT-549 parental and acquired resistant cells treated with metformin (1.3mM) with or without KA (0.3μM or 3μM) for 24 hours. **(H)** Cell viability of MCF-7 cells as in (G). **(I)** Volcano plot showing metabolite profiles of BT-549 acquired resistant (R)3 cells maintained in KA (3μM) with or without metformin (1.3mM) as in (D). **(J)** Acyl-carnitine levels in BT-549 acquired resistant (R)3 cells maintained in KA (3μM) and treated with or without metformin (1.3mM) for 6 hours.

All data are represented as mean ± SEM from n=3 biological replicates.

*p<0.05, **p<0.01, ***p<0.001, ****p<0.0001 as determined by Two-Way ANOVA unless otherwise indicated.

Figure A3.S1 (*Related to Figure 4.3)* - PKUMDL-WQ-2101 and PKUMDL-WQ-2201 selectively bind to PHGDH in cells.

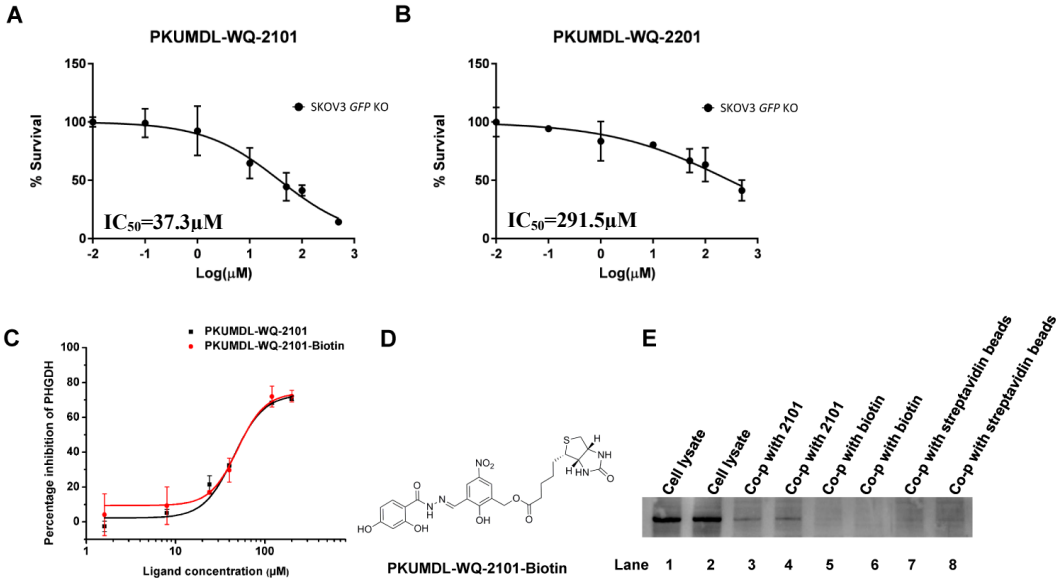

(A) Dose response curve of SKOV3 *GFP* KO control cells treated with PKUMDL-WQ-2101 or **(B)** PKUMDL-WQ-2201 with 0-200µM concentrations for 24 hours. **(C)** Enzyme inhibition assay for biotinylated PKUMDL-WQ-2101. The IC_{50} values for PKUMDL-WQ-2101 and biotinylated PKUMDL-WQ-2101 were 44.9 ± 3.1 and 49.5 ± 6.1 µM, respectively. **(D-E)** Pull down assay of biotinylated PKUMDL-WQ-2101 targeting endogenous PHGDH in MDA-MB-468. **(D)** Structure of biotinylated PKUMDL-WQ-2101. **(E)** PHGDH was pulled down in MDA-MB-468 cell lysates by biotinylated PKUMDL-WQ-2101 and analyzed by western blot with anti-PHGDH (Lanes 3, 4). PHGDH endogenous expression quantity in 15 µl 2 mg/ml cell lysate

supernatant (lanes 1-2), and PHGDH pulled down by biotin (Lanes 5, 6) and free streptavidin beads (Lanes 7, 8) were also analyzed by western blot with anti-PHGDH and used as controls. Co-p, co-precipitate.

Data represent the mean ± SEM.

Figure A3.S2 ***(Related to Figure 4.5)*** **- PKUMDL-WQ-2101 and PKUMDL-WQ-2201 does not affect tumor growth of MDA-MB-231 xenografts.**

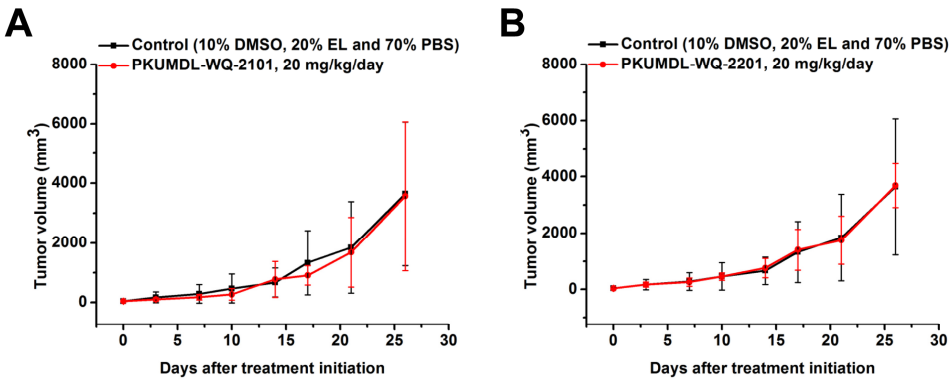

(A-B) Compared with the control group, the growth of tumors was not influenced by the 26-days treatment of **(A)** PKUMDL-WQ-2101 and **(B)** PKUMDL-WQ-2201.

Data represent the mean ± SEM independent experiments.